Brain-Derived Extracellular Vesicles as Therapeutic Vehicles and Molecular Probes in the Neonatal Brain

Nam Phuong Nguyen

A dissertation

submitted in partial fulfillment

of the requirements for the degree of

Doctor of Philosophy

University of Washington

2024

Reading Committee:

Elizabeth Nance, Chair

Lucia Vojtech

Daniel Chiu

Program Authorized to Offer Degree:

Molecular Engineering & Sciences

University of Washington

ABSTRACT

Brain-Derived Extracellular Vesicles as
Therapeutic Vehicles and Molecular Probes
in the Neonatal Brain

Nam Phuong Nguyen

Chair of the Supervisory Committee:
Elizabeth Nance
Department of Chemical Engineering

In the central nervous system (CNS), intercellular communication through extracellular vesicles (EVs) is crucial for sustained trauma response and tissue repair following injury. EVs are biologically derived nanoparticles released by every cell that carry a diverse cargo of biomolecules important for cell communication including proteins, lipids, carbohydrates, and genetic material. The contents of EV cargo is an active research question in the field, and has been shown to be dependent on cell type, as well as environmental and physiological changes. As EVs are both produced and trafficked by cells, they are strong therapeutic candidates with several inherent design advantages over existing nanoparticle therapeutics: biostability, biocompatibility, lipid bilayer protection of cargo, and inherent cell uptake mechanisms. These advantages are especially important for drug delivery to the brain, which presents several therapeutic barriers such as the cerebral spinal fluid barrier and tortuous brain

parenchyma. In addition, the blood brain barrier (BBB) poses a great challenge for therapeutics researchers as it excludes 98% of all small molecule and macromolecular drugs from passing but EVs have demonstrated an ability to cross.

Despite growing interests in advancing EV therapeutics for brain injury and disease, there are two significant challenges hindering their development and clinical translation: 1) lack of physiologically relevant EV models and 2) a need for greater clarity about EV localization and transport in brain tissue. To address the first challenge, I evaluated the therapeutic efficacy of EVs derived from brain tissue (BEVs), rather than the standard approach of using EVs from cell culture. Compared to EVs derived from 2D cell monoculture models, those derived from 3D tissue are more physiologically relevant as they represent a heterogenous population that mirrors the existence of diverse cell types found in native brain tissue. When evaluating the therapeutic potential of BEVs in an *ex vivo* model of oxygen glucose deprivation (OGD), BEVs exhibited dose- and time-dependent therapeutic effects on injured tissue. BEVs induced a shift in the microglial morphology of OGD tissues from an inflammatory towards a restorative phenotype, while simultaneously increasing anti-inflammatory cytokine expression and decreasing cell cytotoxicity. These promising results led to further studies to address the second challenge—a lack in understanding about BEV localization and transport.

To track BEVs in the brain we conjugated BEVs to either quantum dots (QDs) or novel oligonucleotide biobarcodes (oligobarcodes) using an efficient click chemistry reaction. Through a combination of confocal imaging and multiple particle tracking, the QD conjugation allowed us to visualize the spatial distribution of BEVs in brain tissue, which was regionally dependent. QD conjugations also allowed us to track BEV

transport properties in real-time to confirm that BEV behavior was regionally dependent. We then used oligobarcoded BEVs to quantitatively measure the BEV uptake in both glial and non-glial cells in healthy and OGD brain tissue. Microglia, the resident immune cell of the brain, exhibited increased and preferential uptake of oligobarcoded BEVs compared to blank oligobarcode controls. We then expanded our oligobarcode-EV conjugation strategy to study the uptake of semen-derived EVs in the vaginal tract, demonstrating the broad translational opportunities that our platform provided to tracking EVs from any source.

Collectively this work demonstrates the therapeutic potential of tissue-derived BEVs and offers a dual-conjugation technique to visualize and track EVs from any source in physiological environments. Our novel QD and oligobarcode conjugation strategy is an accessible technique that can be translated across different biological models to provide both quantitative and qualitative evaluation of EV visualization and tracking that will advance the EV therapeutics landscape.

ACKNOWLEDGEMENTS

I admit that this is the last section I completed for this dissertation, not because I do not have anyone to acknowledge, but because I have too many. This dissertation was born from a first-generation student's courage, a curiosity for the unknown, a never-ending journey of learning, and most importantly, the unwavering support of many communities. That is what gives this work meaning.

First and foremost, I am forever grateful to my advisor, Professor Elizabeth Nance, for her mentorship and scientific insights. Her encouragement and belief in my abilities were crucial to my success, and she helped introduce new opportunities that I could not have imagined for myself. Her dedication to excellence and empathetic engineering has been an inspiration. She took me in when COVID started, when the world was turned upside down and imposter syndrome kept me in the dark. Thank you, Elizabeth, for bringing me to the light and for taking a chance on me.

I am also grateful for my other dissertation committee members: Professor Lucia Vojtech, Professor Daniel Chiu, and Professor Alshakim Nelson. I value their expertise and encouragement throughout this journey. What started as a collaboration with Lucia became a mentorship, and I am so grateful to have been able to work alongside her. Research is challenging, but she always lent me encouraging words and spent time working together to interpret perplexing results. Lucia's lab became a second lab home. I thank Daniel for his time and technology-focused insights near the end of my Ph.D. I enjoyed our discussions about commercialization, areas for improvement in EV research, and the asbestos at the old Stanford Chemistry building. I thank Al for all he has done for the Molecular Engineering program, and especially for his exemplary support of students. I enjoyed discussing with him about outreach in the community, inclusivity in academia, and how to make academia a more welcoming and accessible environment for underrepresented minorities.

I didn't know anyone when I first moved to Seattle, and now I can't imagine what life would be like without the communities I have been a part of. I give many thanks to the Nance lab--there were countless times when they were the only thing that brought me out of bed and into lab. I am thankful for our moments of shared chatter and laughter, amidst the chaos of experiments. Grad school can be a challenging, emotional, and lonely experience, and I have always felt like I was a part of something bigger because of my team. Special thanks to labmates Hawley Helmbrecht and Ruby Jin for coffees, bobas, and lunches together and keeping me sane with their friendship. I can't imagine my doctoral journey without their friendship and camaraderie. I thank all my undergrad mentees, the "Spooky Action team"—I am so honored to have been their gateway into the exciting world of research and to witness their growth. I am so thankful that our shared interests in nanotherapeutics brought us together.

To my Molecular Engineering cohort mates—I have enjoyed studying, making pizzas, performing outreach, catching up over $6 rosé, and going through these past couple

years with them. Special thanks to Ayumi Pottenger, my program bestie, and my work wife. She is incredibly strong and kind, a beautiful kindred spirit who entered my life.

To my dear friends whom I've met at various stages in my journey but have stayed with me nonetheless—you all bring light into my life. Special thanks to Kristen Warden and Danica Coffin, two of my longest friends (Kristen gets a special shout out as our friendship has spanned almost 20 years!), who have brought so much joy, gummy bears, bad holiday shows, and birthday cards to me in all those years.

Last, I want to thank my family—I would not be here without them. To my parents Phat Nguyen and Hanh Huynh, to whom I dedicate everything I do, and who have blessed me with a drive for education. It is possible for me to be the first college graduate and now Ph.D. in our family because of sacrifices they made in this new country. I thank them for supporting me through college and grad school, even though those were opportunities that they never had. To my brother, Danh Nguyen, who has saved me more than once. To my loving husband Dr. Alexander Yuan, for being a source of scientific discourse and adventure. Alex has been a constant through transformative moments in my career, and I am so thankful to be supported by and to experience life with such an inspirational scientist. Alex also expanded my family, and I thank Mindy Loebner and Ed Yuan for welcoming me into their family with open arms.

It is only with the help of these individuals that this research and dissertation have taken form, and that my contributions to the scientific community have been made.

TABLE OF CONTENTS

LIST OF FIGURES

LIST OF TABLES

LIST OF APPENDICES

LIST OF ABBREVIATIONS

AEVs: Astrocyte-derived EVs
APC: Antigen-presenting cell
BCA: Bicinchoninic acid
BEV: Brain-derived extracellular vesicle
CNS: Central nervous system
DAPI: 4′,6-diamidino-2-phenylindole fluorescent stain
DG: Density gradient
DLS: Dynamic light scattering
EV: Extracellular vesicle
FACS: Fluorescence activated cell sorting
FQDs: Functionalized quantum dots
HI: Hypoxia-ischemia
HIE: Hypoxia-ischemia encephalopathy
ISEV: International Society for Extracellular Vesicles
LC-MS: Liquid chromatography-mass spectrometry
MSC: Mesenchymal stem cell
NTA: Nanoparticle tracking analysis
OGD: Oxygen-glucose deprivation
Oligo: Oligonucleotides
Oligo-BEVs: Oligobarcode-conjugated BEVs
Oligo-SEVs: Oligobarcode-conjugated SEVs
OWH: Organotypic whole hemisphere
QD: Quantum dot
QD-BEVs: Quantum dot-conjugated BEVs
ROS: Reactive oxygen species
SEC: Size exclusion chromatography
SEV: Semen-derived extracellular vesicle
SM: Shape mode
TEM: Transmission electron microscopy
TH: Therapeutic hypothermia
Treg: Regulatory T cell
UC: Ultracentrifugation
UF: Ultrafiltration

CHAPTER 1. INTRODUCTION

1.1. The Global Impact of Neonatal Hypoxia-Ischemia Encephalopathy (HIE)

Brain injury that occurs early in life is highly associated with increased risk of neurodevelopmental disorders in adulthood, indicating the importance of studying this early developmental period for later health outcomes.[1] Hypoxic-Ischemic Encephalopathy (HIE) is a brain condition that is the leading cause of morbidity and mortality in neonates, to which there is no cure.[2] Neonatal HIE is clinically characterized by neurologic dysfunction due to a reduction of adequate cerebral blood flow in neonates up to 28 days old. This reduction of blood flow leads to deficient supplies in glucose and oxygen to sensitive tissues of the brain. If left untreated, HIE results in serious consequences for many infants including death, permanent brain damage, cerebral palsy, epilepsy and other significant cognitive and developmental impairments.[3] Globally, neonatal HIE poses a heavy health burden on infants and their families. The incidence rate of HIE in low and middle income countries is as high as 26 afflicted neonates per every 1000 live births.[4] Even in high resource countries, the incidence rate remains high at up to 8 afflicted neonates per 1000 live births, a number which has not decreased in the past two decades.[4, 5] Complex risk factors such as in utero infection, antepartum bleeding, uterine rupture, and maternal socioeconomic standing make HIE difficult to predict and diagnose at the time of injury.[3] Anywhere from 10 to 60% of neonates affected by HIE do not survive injury onset.[6] The high morbidity rate of HIE is often compounded by the difficulty in diagnosing the onset of HIE due to subtle symptoms in neonates. Among those who survive injury onset, elevated

morbidity rates of disability such as cerebral palsy and cognitive decline in patients persist throughout adult life.[5]

Despite the seriousness of neonatal cerebral ischemia, there are currently no effective treatment options for the ischemic newborn brain. The current state of the art treatment for mild to moderate HIE is therapeutic hypothermia (TH). TH requires rapid cooling of vulnerable deep brain structures in infants to a temperature range of 33.5 °C to 34.5 °C for up to 72 hours.[6, 7] Unfortunately, TH treatments for neonatal HIE provides only modest benefits in mortality and morbidity, with 30-50% of treated infants continuing to experience poor health outcomes (including death or severe disability).[8] Recent studies have concluded that TH is not an effective treatment option for neonates with severe HIE, regardless of the cooling temperature or length of cooling.[9] The complex nature of immune response during an HI event makes it difficult to develop effective treatments that target injury response mechanisms.

1.2. Injury Response in the Neonatal Ischemic Brain

1.2.1. Excitotoxicity in HIE Onset

Acute onset of HIE triggers a complex set of physiological responses that accumulate and can lead to long-term impairment for up to years following the injury. During initial HIE onset, insufficient supply of glucose and oxygen due to reduced blood flow leads to a deficit in adenosine triphosphate (ATP) production. As a result, cells undergo sodium/potassium ion pump failure and switch to anaerobic metabolism producing lactic acid that lowers the pH of the surrounding tissue.[10] The combined decrease in ATP and increase in acidosis causes an overcompensation of glutamate release into surrounding tissues. As glutamate is a major excitatory neurotransmitter in

the central nervous system (CNS), its overproduction prompts dysregulation of neuronal stimulation and leads to neuronal death, a condition known as excitotoxicity.[11] Overstimulation of neurons during excitotoxicity triggers neuronal death and a build-up of reactive oxygen species (ROS) and superoxide radical anion (SOX) that further damage cellular integrity and initiates oxidative stress.[12] This chain of excitotoxicity and oxidative stress sends signals to peripheral and resident immune cells, prompting for a dynamic response to the injury.

1.2.2 Immune Cell Cascades in Response to Excitotoxicity

A hallmark of HIE is the immediate and sustained inflammation that occurs as a physiological response to injured tissues.[13] The infiltration of peripheral immune cells and activation of pro-inflammatory microglia and astrocytes immediately following an ischemic event can drive inflammation, cell death, and phagocytosis of damaged tissue that can persist for days to years after the insult.[14] Activated immune cells can also remain in the area of injury months following the initial onset and trigger subsequent inflammation in tissue.[15] Microglia and astrocyte response to HIE are of particular interest due to their unique involvement in immune regulation in the brain.[15]

Microglia – one type of glial cell in the CNS - are often regarded as the resident immune cells of the CNS and play an important role in the surveillance and response to invading pathogens and tissue injuries.[16] Acute onset HIE leads to rapid neuronal cell death and activation of resident microglia to migrate to injured tissue sites.[17] Upon reaching the area of injury, microglia release inflammatory cytokines that contribute to a signaling cascade that recruits other cells to the area, such as activated neutrophils and astrocytes.[18] These released cytokines include both pro-inflammatory (e.g. tumor

necrosis factor (TNF), interleukin (IL)-1β, IL-6) and anti-inflammatory species (e.g. IL-4, IL-10, and transforming growth factor (TGF-β)) that serve opposing roles in order to coordinate the removal of injured and dead cells and debris as well as the recovery of tissue homeostasis and promotion of neurogenesis.[15, 19, 20] Recent studies correlate microglial morphology to disease state and injury progression within the brain, though the exact classifications of microglial phenotypes remain highly disputed.[21] Microglial crosstalk with other cells is crucial to produce a coordinated immune response to HIE.

Similar to microglia, astrocytes are glial cells that play an important role in injury response in the brain. Astrocytes are responsible for water homeostasis, tissue repair, scar formation, synapse modulation, regulating oxidative stress, and energy storage among other roles.[22] Astrocytes are sensitive to glutamate levels within the brain due to the presence of neurotransmitter receptors on their surface that are similar to those of neurons. Increased glutamate production during HIE can cause activated microglia to produce ROS and increase their phagocytotic behavior targeted towards synapse elimination.[18] Hence, increased levels of ionic dysregulation coupled with inflammatory microglial signaling can lead to reactive astrocytes that exacerbate neuronal death and dismantle healthy cellular crosstalk.[23] Activated microglia and astrocytes can remain in the brain for months to years following an acute injury such as HIE.[14]

Since microglia and astrocytes are both critical to normal brain function, HIE injury disrupts healthy crosstalk between cells. Given that highly coordinated immune response between cell types is essential for brain development and neuronal recovery, it is advantageous to evaluate important players of intercellular communication during an ischemic event. Extracellular vesicles (EVs) in the brain are one such critical player

in intercellular communication that has recently gained widespread attention in the nanotherapeutics space.

1.3. Introduction to Extracellular Vesicles (EVs)

1.3.1. Extracellular Vesicles are Important Players in Intercellular Communication

Extracellular vesicles (EVs) are unique biologically derived nanoparticles that are produced in every cell type in the body and serve as a critical mode of intercellular communication.[24-26] Surrounded by a lipid bilayer, EVs are capable of carrying a wide repertoire of biomolecules involved in critical physiological pathways including proteins, carbohydrates, and genetic material. Though there is no final consensus on a standardized classification of EVs, the current recommendation is to use the umbrella term 'extracellular vesicle' or denote EVs by size.[27] EVs can range anywhere from 20nm to over 1μm in diameter. Terms that suggest a biogenesis pathway such as 'exosome,' 'microvesicle,' and 'ectosome' which were acceptable 5 years prior are now discouraged under current guidelines set by the International Society for Extracellular Vesicles (ISEV). This change in standards exemplifies the dynamic nature of the rapidly expanding field of EV research. It is important to note that at this time, there are no standardized definitions for EV classifications due to the difficulty in assigning an EV to a particular biogenesis pathway unless real-time video of biogenesis is recorded.[27-29]

Despite differences in their biogenesis, size, or cargo, all EVs are released from the plasma membrane and taken up by every cell type in the human body. In recent decades EVs were considered for many years to either be inert cellular debris or otherwise act as receptacles for cellular debris.[26] However, it is now accepted that EVs play a crucial role in shuttling important biomolecular signals between cells and

potentially across long distances via body fluids. Though the mechanisms of EV biodistribution and cell-specific uptake remain unclear, EVs contain cargo that are horizontally transferred to neighboring cells, acting as an important mode of cellular communication.[26, 30] Cellular communication is necessary for proper coordination and tissue homeostasis following injury or disease. Due to their role as critical mediators of cellular communication, EVs are well suited to act as both messengers for therapeutic delivery as well as informants on disease progression and injury pathogenesis in physiological tissues, such as the brain.

1.3.2. Extracellular Vesicles in the Brain

A functional CNS relies on effective and robust exchanges of information between complex and diverse networks of cells. EVs are active in multiple critical processes including the regulation of synaptic plasticity, and neuronal development, proliferation, and transmission.[25, 31-33] Studies have suggested that various proteins on the surface of EVs bind to surface receptors presented on the BBB allowing transport from both directions (i.e. from the bloodstream towards the brain and vice versa), though specific players involved in these observations are likely model- dependent.[34, 35]

As tissues are comprised of a diverse cellular population, the EVs that are collected from whole brain tissue are also heterogeneous in nature in regard to their surface moieties and cargo. Huang et.al. have shown through their efforts of compiling a comprehensive ‘human brain EV atlas’ that EV characteristics from the brain are highly varied between regions.[36] For example, cell-enriched surface markers such as neuronal markers NCAM and CD271 varied between brain regions and subsequent principal component analysis of the RNA content in the brain EVs showed clearly separated

groups of RNA expression between the cerebellum and thalamus. In addition, particle size, morphology, and concentrations were also varied between regions. Various *in vitro* and *ex vivo* studies have successfully isolated cell-specific EVs from all CNS cells, which show that EVs carry unique cell-specific cargo and surface markers that mirror their cell of origin.[32, 37] For instance, EVs derived from microglia, which are the resident immune cells of the brain, contain major histocompatibility complex (MHC) class II receptors that are involved in initiating the body's immune response to pathogens.[32] These cell-specific cargo can also be influenced by the injury state of the cell.[38, 39]

Under standard conditions, EVs support critical crosstalk between neurons and glial cells to promote cellular signaling, support of the blood brain barrier, neuronal firing rates, and neurogenesis.[32, 40] However, in injury or disease conditions, EVs can contribute to the spreading of inflammatory, antigenic, and cell death signals throughout the body.[33] Following tissue inflammation, astrocytes and microglia release EVs that stimulate the production of inflammatory cytokine IL-1β that propagates injury response.[41, 42] In Alzheimer's Disease models, it has been shown that neuronally derived EVs are enriched in amyloid-β proteins that can contribute to accumulation of amyloid-β plaques.[43] EVs released from glioblastoma (GBM) tumors have been shown by several groups to secrete EVs with high immunogenic potential in mice and humans.[43, 44] In an injured brain model, EVs shed from glial cells such as microglia and astrocytes have been shown to cross the blood brain barrier (BBB), though the mechanism of action is unclear.[45, 46]

Not only is EV cargo in the brain affected following injury and disease, but also EV release and trafficking. The rate and specifications of EV uptake has been

demonstrated to depend on both the EV characteristics and the recipient cell, which affect cellular crosstalk.[40, 47] For example, Chivet et. al. demonstrated that EVs derived from neuroblastoma are selectively endocytosed by glial cells, whereas EVs released from neurons are preferentially taken up by other neurons in culture.[48] Brenna et.al showed that under healthy conditions, microglia are the main source of EVs released in the brain, whereas after HI injury the main EV population originated from astrocytes.[49] Similarly, the cargo proteins of astrocyte derived EVs in healthy and inflammatory conditions were compared by You et.al.[41] Their findings revealed that astrocyte EV cargo changed considerably following the application of an inflammatory IL-1β stimulus, and that astrocyte EVs from injured cells were more likely to be taken up by neurons, leading to reduced neurite outgrowth and firing. Bianco et. al. and Yang et.al. demonstrated that both microglial and astrocyte cells experience heightened release of EVs in response to tissue inflammation in the brain compared to a healthy control.[37, 50] Together, these results suggest that EVs are actively involved in tissue regulation both in healthy and injury conditions in the brain and their characteristics and cargo are both cell-dependent but also pathology-dependent.

1.3.3. The Role of Extracellular Vesicles in HIE Injury Response

During HIE, cells are simultaneously releasing pro-inflammatory cytokines via EVs that lead to oxidative stress and cell death as well as anti-inflammatory cytokines that help clear debris and rebuild tissue.[51] Though inflammation plays both beneficial and detrimental roles in the injury outcome of HIE, it serves as a vital period for brain repair and is a major target for the development of therapies. Both *in vivo* and *in vitro* studies confirmed that treatment with cell culture-derived EVs leads to increased

neuronal recovery in adult stroke and traumatic brain injury models.[52-54] Recently, Xin et. al. published a paper demonstrating that intravenous application of mesenchymal stem cell (MSC)-derived EVs in a perinatal rat model improved neurological outcomes, angiogenesis, and neurogenesis following HI.[55] Several groups have also found that EVs derived from neuronal, microglial, and astrocytic stem cells attenuated neuronal death, reduced pro-inflammatory and apoptotic signaling, and improved synaptic transmission rates in both *in vitro* and *in vivo* HI models.[54, 56-58]

Though EV research has significantly expanded over the past years, a large challenge facing the field is a lack of physiologically relevant EV models.[59-61] Furthermore, it is agreed upon in the scientific community that the therapeutic effects of MSC therapeutics on tissues is not due to the physical implantation of the MSCs themselves, but rather, through EV-mediated paracrine effects.[62] This revelation suggests that it may be possible to directly administer EVs as therapeutic agents rather than MSCs. The unique property of EVs to maintain the cargo of their origin cell allows them to be important carriers of information about the endogenous processes occurring within the brain microenvironment. For advancements in the field of EV therapeutics to have the greatest impact and potential for clinical translation to neonatal models, it is imperative to gain a greater understanding of endogenous EV activity in the brain.

1.3.4. EV Therapeutics

Synthetic nanoparticles have widely been used in the drug delivery space for almost 3 decades, though complex interactions within biological environment are a significant barrier for the successes of most nanoparticle formulations. The ability of EVs to transport unique cargo intercellularly indicates a strong potential for EVs to be

used as a therapeutic vehicle and/or diagnostic tool. This unique ability to transfer information between cells elevates EVs as a promising therapeutic candidate for areas that have been traditionally difficult to target with other nanomedicine platforms, such as the central nervous system (CNS). EVs have many strong advantages for the design of therapeutic platforms, including: 1) biocompatibility, 2) small size, 3) non-immunogenicity, 4) stability, and 5) inherent targeting capacity to cells.[63] Additionally, while the BBB serves as a significant obstacle to many nanotherapeutic platforms, EVs are capable of crossing this barrier. EVs also have a strong record of attenuating inflammation in the body. There are currently several EV-based therapies in clinical trials for brain tumors and injury.[64] Specifically, a Phase I study using EVs derived from induced human pluripotent stem cells to treat adults with acute HI has recently started recruiting participants in 2024 (NCT06138210).

Though there is growing interest in establishing EV therapeutics for brain injury, most studies and all clinical trials evaluating EV therapeutic potential are performed on adult models using cell-culture derived EVs. In contrast, we have successfully sequestered brain tissue-derived EVs (BEVs) to better recapitulate endogenous HIE injury response in a neonatal 3D model. It has been shown that EVs derived from 3D models rather than 2D cell culture are more physiologically representative and elicit improved therapeutic responses.[65, 66] Thippabhotla et.al. observed that 2D culture derived EVs showed significantly different secretion and biomolecular cargo profiles (RNA and DNA) when compared to EVs derived from 3D culture. Zhang et. al. demonstrated that MSC EVs cultured in 3D collagen scaffolds led to improved spatial memory in rats following traumatic brain injury compared to EVs cultured in 2D

conditions.[59] Our isolated BEVs formed the crux of our studies, as they are the subject of our therapeutic efficacy studies and subsequent characterization and localization studies. In this way we can better study the therapeutic roles and behaviors of endogenously derived EVs under physiological conditions.

Despite the immense therapeutic potential of EVs to improve HI outcomes in *in vitro*, *ex vivo*, *and in vivo* models and the existence of several EV-based clinical trials, the translation of EV therapeutics remains a challenge. One of the main challenges is the heterogenous nature of EVs in the body. Most EV research in literature is performed using EVs derived from monoculture, while EVs in the body exist as a diverse population derived from several different cell types. Due to this discrepancy in research, it is difficult to determine how EVs in the body behave differently compared to a uniform population of EVs derived from cell monoculture. In addition to uncertainty surrounding the heterogenous nature of endogenous EVs, another challenge is a lack of available and accessible tools to quantify EV behavior and localization in brain tissue. In my work I addressed both challenges, as outlined in Chapter 1.5.

1.4. *Ex Vivo* HI Neonatal Models to Screen EV Therapies

Our lab has developed an organotypic whole hemisphere (OWH) brain slice model of oxygen glucose deprivation (OGD) that captures HI injury in the neonate.[11, 67] OWH brain slices capture the 3D architecture and regional complexity of the brain, allowing for the simultaneous assessment of different brain regions (cortex, hippocampus, thalamus, etc.) not present in standard cortical, hippocampal, or organoid models.[68-70] This includes deeper regions in the brain such as the striatum. As one brain can produce multiple slices, this procedure also reduces the number of animals needed

for an experiment. OWH brain slices can be imaged with various forms of microscopy such as confocal or 2-photon imaging, including live-tracking of nanoparticles or cells throughout the brain parenchyma. Our lab has used OWH models to probe nanoparticle diffusion across multiple brain regions and ages as well as to screen and test for the efficacy of various nanotherapeutics on cells of the central nervous system. Mechanistic studies can also be performed using OWH brain slices by measuring whole slice metabolic activity, gene expression through quantitative PCR, and staining for cell stress (HIF-1α, iNOS), death (Casp-3), and proliferation (EdU). This work will detail the use of OWH slices to model HI injury and the brain's subsequent immune response to BEV treatment through imaging and live-tracking of glial cells on a population and single-cellular level and studying changes in tissue RNA/protein expression.

To model HI *ex vivo,* OGD conditioning applied to our OWH slices. OGD models are a standard procedure in our lab to recapitulate disease processes for nanotherapeutic applications.[67, 69] Studies indicating increased (Hypoxia-Inducible Facto-1α) HIF-1α levels as well as PI/DAPI cytotoxicity staining confirmed that OGD conditioning induces hypoxia in *ex vivo* slices.[69] It has also been demonstrated that postnatal (P) day-10 brains have increased cellular proliferation measured by E-ethynyl-2'-deoxyuridine (EdU) staining, compared to P17 brains for up to 14 days following acute slicing, and that overall cell death is dependent on donor age, brain region, and OGD exposure time. [69] To study EV therapeutic activity and its impact on cellular behavior, we performed OGD conditioning in *ex vivo* slices from male P10 rat brain to model HI in term-equivalent neonates. We used males for our experiments because it is generally accepted that males have worse outcomes in neurological injury

than females.[71] The OGD slice model is a powerful, clinically relevant tool for evaluation of EV therapeutic efficacy in the ischemic brain microenvironment.

1.5. Overall Research Objectives

The objectives of this research thesis are: 1) to establish the therapeutic potential of BEVs in a neonatal HI model, 2) to deploy quantum dot conjugations to probe and visualize BEV spatial distribution within the injured brain, and 3) to establish a novel and translatable oligonucleotide barcode methodology to track EV uptake.

Chapters 2-4 contains published or submitted work demonstrating my approaches for addressing these research objectives. Chapter 2 delineates my optimized methods for BEV extraction and characterization, which were used for therapeutic efficacy studies on OGD models of HI. Results from my work showed that BEVs confer therapeutic effects in a dose- and time- dependent manner. These promising therapeutic results from chapter 2 motivated my work in chapters 3-4 wherein we implemented click chemistry conjugation to tag EVs with either quantum dots (QDs) or oligonucleotide barcodes (oligobarcodes) to further investigate BEV localization and transport in brain tissue. This novel technique addresses current challenges with EV tracking and facilitated collaborative work with Dr. Lucia Vojtech (Chapter 4) in the deployment of this oligobarcode conjugation technique to track semen-derived EVs in the female genital tract. Chapter 5 is a summary of various completed and ongoing projects that I have participated in. Chapter 6 is my curriculum vitae to date.

EVs are an emerging therapeutic platform, to which there are several advantages over current nanoparticle formulations for treating neurological injury and disease. Since my work focuses on EVs derived from brain tissue, it is important to note that I am

proposing preclinical tools for advancing EV research. Further translation and implementation of EV therapeutics to the clinic and for commercial use will require considerations for scalability. To this end, using cell-derived EVs would be the most efficient and scalable method to produce EVs for patients, specifically, EVs derived from mesenchymal stem cells as they are the current standard in the field. However, before EV therapeutics can be translated and scaled, we must first understand the behaviors of endogenous tissue-derived EVs. Understanding tissue EV characteristics, localization, and cellular fate across different brain regions and injury states will improve the disease-directed engineering process of future EV designs. My work seeks to address knowledge gaps in this field by using tissue-derived EVs rather than cell culture-derived EVs to maintain physiologic relevance.

As a quickly evolving field of study, EV research requires greater standardization in EV-specific definitions, controls and research methodology. The International Society of Extracellular Vesicles publishes a document outlining standardization recommendations every 4 years, demonstrating the dynamic future of this field. It is my hope that this thesis will provide greater insight into not only the therapeutic potential of BEVs for neonatal health outcomes, but will also introduce a new translatable EV tracking platform, and inform the community on both the limitations and strengths of studying BEVs for clinical translation.

CHAPTER 2. INVESTIGATING THE THERAPEUTIC POTENTIAL OF BEVS IN THE NEONATAL HYPOXIA ISCHEMIA

Nam Phuong Nguyen, Hawley Helmbrecht, Ziming Ye, Tolu Adebayo, Najma Hashi, My-Anh Doan

This chapter was published in the *International Journal of Molecular Sciences* in 2022 under the title “Brain Tissue-Derived Extracellular Vesicle Mediated Therapy in the Neonatal Ischemic Brain."

2.1. Introduction

HIE is the leading cause of mortality and morbidity in neonates, to which there is no cure. Though there is significant interest in establishing EV therapeutics as a platform to treat brain injury and disease, the field lacks comparable biological models. Most published studies and all clinical trials evaluating EV therapeutic potential are performed on adult models using EVs derived from stem cell culture. Given that the status quo in EV therapeutics research is to use 2D cell culture-derived EVs in adult models, there are two limitations in translating this work into the neonatal space: 1) neonatal physiology and disease progression may be different from what is observed in adult models and 2) EVs derived from stem cell culture do not fully recapitulate their endogenous activity. Understanding the endogenous activity of BEVs within the neonatal brain can inform researchers about the design criteria required to engineer EV therapeutics with improved targeting and functional capabilities neonates.

To address the lack of knowledge surrounding tissue-derived EVs in the field, we have successfully sequestered EVs derived from the neonatal brain (BEVs) to better

recapitulate endogenous HIE injury response in a neonatal 3D model. In doing so, we can evaluate BEVs as therapeutic agents and molecular probes in HI.

2.2. Materials & Methods

2.2.1. Animal Care and Ethics

This study was performed in accordance with the guide for the care and use of laboratory animals of the National Institutes of Health (NIH). All animals were handled according to an approved Institutional Animal Care and Use Committee (IACUC) protocol (#4383-02) of the University of Washington (UW), Seattle, WA. The UW has an approved Animal Welfare Assurance (#A3464-01) on file with the NIH Office of Laboratory Animal Welfare, is registered with the United States Department of Agriculture (certificate #91-R-0001), and is accredited by AAALAC International. Time-mated pregnant female Sprague–Dawley rats (virus antibody-free CD® (SD) IGS, Charles River Laboratories, Raleigh, NC, USA) were delivered on postnatal day 5 with a litter of 10, sex-balanced pups. Dams were housed individually with their litter and allowed to ac-climate to their environment. Before and after the experiment, each dam and her pups were housed under standard conditions with an automatic 12 h light/dark cycle, a temperature range of 20–26 °C, and access to standard chow and autoclaved tap water ad libitum. The pups were checked for health daily.

2.2.2. OWH Slicing Methodology

Following intraperitoneal euthanasia with pentobarbital, fresh brain tissue was rapidly extracted from P10 male rats, placed in ice cold dissection media, and sectioned into 300 μm slices using a McIlwain tissue chopper (Ted Pella, Redding, CA, USA). These slices were plated onto 30 mm cell culture inserts (Millipore Sigma, Burlington,

MA, USA) in nontreated 6-well plates (USA Scientific, Orlando, FL, USA). Slices were then incubated at 37 °C in 1 mL of 5% slice culture medium (SCM) at 37 °C and 5% CO2 to recover from acute slicing. SCM medium with 5% horse serum consists of 180 mL HBSS (Gibco), 20 mL horse serum, 200 mL MEM (Gibco, Dublin, Ireland), 4 mL PenStrep, and 4 mL GlutaMax (Gibco). Days in vitro (DIV) 0 was defined as the day of brain extraction and slicing. At DIV1, the media was exchanged with fresh 5% SCM.

2.2.3. OGD Methodology

Acute brain slices are incubated in oxygen-glucose deprived media within an oxygen-free chamber.[67, 69] Since multiple slices can be obtained with one brain, OWH slices reduce the number of animals required and allow for higher throughput screening. At DIV3 slices were placed in glucose depleted media and a hypoxic chamber for 30 min before further tissue processing. OGD medium consists of 120 mM NaCl, 5 mM KCl, 1.25 M NaH2PO4, 2 mM MgSO4, 2 mM CaCl2, 25 mM NaHCO3 and 20 mM HEPES. The solution was passed through a vacuum filter unit 0.2 µm (Nalgene, Rochester, NY, USA). Previous work in the rat determined that 30 min incubation time under these conditions was sufficient to induce significantly higher cell death compared to healthy slices.[67] Varying OGD exposure can result in a high degree of cell death and depletion of glutathione (GSH), a mediator of intracellular oxidative stress.

2.2.4. BEV Isolation Using a Combination of Methods

A modified BEV isolation procedure published by Vella et. al. was used to extract and enrich BEVs from whole rat brain.[72] Each rat brain was perfused with 10 mL PBS to reduce contamination from blood and serum-derived EVs. For every extraction, four PBS perfused P10 brains were used from the same litter and sex to limit biological

variability and flash frozen prior to processing. Whole brains extracted from P10 rats were finely chopped in a solution and incubated for 20 min in a water bath with protease inhibitors to allow for complete dissociation of extracellular matrix proteins. Subsequently, tissue samples were ultracentrifuged under increasing speeds at 4 °C to remove large proteins and cellular debris from the supernatant. The homogenate was initially spun at 300× g for 5 min, transferred to a new tube to spin at 2000× g for 10 min, and finally transferred to new tubes and ultracentrifuged for 10,000× g for 35 min. After ultracentrifugation, the collected supernatant was run through an Amicon ultrafiltration column (100 kDa molecular weight cutoff) and spun at 3214× g for 90–120 min, or until the final volume reached 500 µL. A size exclusion chromatography column (iZon Science, Portland, OR, USA) was then used to further purify BEVs, and fractions containing high concentrations of BEVs were ultracentrifuged in an Amicon ultrafiltration column (50 kDa) at 3214× g for 60–90 min at 4 °C to concentrate isolated BEVs. The concentrate was collected, and flash frozen at −80 °C in 1X PBS until use.

2.2.5. BEV Characterization

The total protein concentration of the isolated BEV solution was quantified using a bicinchoninic acid assay (BCA, Pierce BCA Protein Kit). Nanoparticle tracking analysis (NTA) using a NanoSight was used to quantify particle size (nm) at a dilution of 1:1000 in 1X PBS. The purity of BEVs was calculated as the number of particles measured by NTA/protein concentration measured by BCA [51]. The zeta potential of BEVs suspended in 1X PBS was measured using a Zetasizer (Malvern Panalytical, Malvern, UK).

The identity of isolated EVs was verified using dot blot immunodetection. The dot blots were labeled for positive and negative surface markers. Positive EV markers included: tetraspanins CD9 (1:500, BD Biosciences, Franklin Lakes, NJ, USA) and CD63 (1:500, BioRad, Hercules, CA, USA). The negative EV protein marker used is a membrane protein of the Golgi Apparatus GM130 (1:500, BD Biosciences, Franklin Lakes, NJ, USA). A housekeeping marker GAPDH (1:500, Thermofisher, Waltham, MA, USA) was also used as a positive control for the tissue lysates, while 1X PBS was used as the negative control. BEVs and P10 brain tissue were lysed using 1X RIPA buffer with a 1X protease inhibitor cocktail on ice (100x, Thermofisher, Waltham, MA, USA). Lysates were incu-bated on ice for 20–30 min following the addition of 1X RIPA. The brain tissue lysates were ultracentrifuged at 15,000× g for 30 min at 4 °C to pellet cell debris, which was then removed for dot blotting. BEV lysates were concentrated using a 3 kDa molecular weight cutoff ultrafilter (Thermofisher, Waltham, MA, USA) and ultracentrifuged at 15,000× g. A BCA quantification was used immediately prior to dot blotting to determine the protein mass loaded onto each membrane. Strips of wetted polyvinylidene fluoride (PVDF) transfer membranes were prepared (Thermofisher, Waltham, MA, USA), and a hydrophobic pen was used to draw rings for each sample protein. Proteins from BEV and brain tissue lysate were aliquoted at a volume of 15 µL into each ring. Following an initial blocking with 5% skim milk in TBST buffer at room temperature, the membranes were blocked with primary antibodies diluted with 5% skim milk TBST buffer on a shaker overnight at 4 °C. The following morning, the membranes were blocked with secondary antibody (IR800 goat anti-mouse, 1:4000) for 1.5 h in the dark at room temperature. After staining with secondary antibody, the membranes were

washed with 5% skim milk and TBST buffers several times before imaging (Azure Biosystems, Dublin, CA, USA).

Dot immunoblots were analyzed using ImageJ and the integral signal density (total fluorescent signal) of each sample was quantified within a region of interest of the same area for each sample. All sample fluorescent intensities were normalized with the blank solution (PBS) prior to quantification.

2.2.6. Transmission Electron Microscopy (TEM) Imaging

TEM Imaging was performed using a FEI (Thermoscientific) TF20 TEM at the UW Molecular Analysis Facility at 200 kV with an Eagle CCD Camera. To prepare BEV samples on a carbon grid, aliquots of BEVs were thawed and mixed with an equal volume of 1.5% glutaraldehyde buffered with 0.1 sodium cacodylate buffer for fixing. Then, 200 mesh TEM grids were glow-discharged, and 10 µL of BEV suspension was placed onto the grid and left to dry for 5 min in ambient temperature. The grids were then exposed to 5% uranyl acetate for 5 min and washed three times with a droplet of distilled water. Grids were air-dried before storage.

2.2.7. BEV Administration on Ex Vivo Slices

Frozen BEV fractions were thawed and gently resuspended with a pipette. BEV solution was then diluted with sterile 1X PBS to achieve experimental dosages (5 µg, 12.5 µg, 25 µg, 50 µg) suspended in a total volume of 100 µL per slice. The BEV solution was topically applied onto the tissue slices at various application timepoints (−24, 0, 4, and 24 h post-OGD conditioning), aligned with previous therapeutic efficacy studies performed in OWH slices.[67, 69] After various BEV exposure timepoints of interest

(4, 24, and 48 h), slices were stained with propidium iodide (PI) to quantify cell viability and fixed with 4% formalin. Formalin fixed slices were subsequently co-stained with DAPI and Iba-1 (Wako), a standard marker of microglia.

2.2.8. Confocal Imaging

A Nikon A1R confocal microscope was used for blinded quantification of cell viability (PI-stained cell count/ total cell count). Three to five images were captured of the cortical region of every slice at 40× magnification and each image was blinded to participants involved in cell counting with ImageJ. Confocal images of cells were taken at 40× magnification and further processed computationally.

2.2.9. Cell Morphology Analysis

All images of interest from each treatment and control group of Iba-1-stained slices were converted from .nd2 file format to .tiff file format using the Nikon's Confocal NIS-Elements software. The saved .tiff files of all images were segmented by multiple thresholding methods using scikit-image's try_all_threshold functionality which includes the isodata, li, mean, minimum, otsu, triangle, and yen thresholds.[73] An image showing the original cell image compared with the other seven thresholding methods was saved as a .tiff for qualitative comparison. The Li threshold method for segmentation was determined to be most accurate when comparing to manual segmentation with the Fiji implementation of ImageJ.[74] For further quantification, the images were individually segmented using scikit-images threshold_li function followed by removing small objects smaller than 71 pixels^2 and filling all holes. To determine the size of the small object to remove, we accounted for the average size of microglia (1600 μm^2).[75] The microglia size was converted to a pixel cut off by (1) converting from pixels to μm with the

confocal metadata 1 pixel = 3.4527 um conversion (2) ensuring no potential microglia were cut off by selecting a lower boundary at half the average microglia size.

After segmentation, cells were quantified with two methods: regionprops analysis through Sci-kit image and with Visually Aided Morpho-Phenotyping Image Recognition (VAMIRE).[76] With the regionprops functionality, cells were individually measured for geometric parameters including area, perimeter, major axis length, and minor axis length. The aspect ratio of cells was calculated as the ratio of the major axis length to the minor axis length and cellular circularity was calculated with the following equation:

$$\text{Circularity} = \frac{4\pi * \text{Area}}{(\text{Perimeter}^2)}$$

Heat maps of the fold change of individual geometric features from regionprops analysis were created using Excel conditional formatting with a custom 2-scale color map with white as the highest value and a unique color as the lowest value—perimeter: green, area: yellow, circularity: blue, and aspect ratio: purple.

For VAMPIRE analysis, the NumPy files of the cell images after threshold-based segmentation were split into four equal quadrants. For each quadrant, any cell touching the edge of the image was removed to avoid noise created by artificial straight edges. All the quadrants were split into groups for building and applying a VAMPIRE model via an 80:20 train: test split. Models were built and applied according to previously published VAMPIRE methodology.[76] Five shape modes (SM) where chosen to capture biological variation while remaining computationally efficient. The VAMPIRE method also produced results of the aspect ratio, circularity, perimeter, and area of every cell and correlated shape mode. Qualitative visualizations of the segmented cells were

created with Python by assigning each shape mode a color with the Matplotlib twilight color map. Heat maps of shape mode frequencies were created in Microsoft Excel with conditional formatting and a red-yellow-green color scale. All code can be found on the Nance Lab GitHub repository.[77]

2.2.10. Reverse Transcriptase Quantitative Polymerase Chain Reaction (RT-qPCR)

Changes in pro-inflammatory, anti-inflammatory, cell death, glial activation, and oxidative stress gene expression profiles following BEV treatment was quantified using RT-qPCR. For each condition, three brain slices were cultured together on the same membrane. Slices were preserved in RNALater (Thermofisher, Waltham, MA, USA) and kept at 4 °C prior to processing to prevent RNA degradation. The RNA from homogenized brain slices were extracted with TRIzol reagent, pelleted at 15,000× g, washed several times with ultrapure DEPC water (Thermofisher, Waltham, MA, USA) and 70% ethanol, and the RNA final concentration was measured using a NanoDrop. cDNA was diluted to 20 ng/μL with ultrapure RNA-free water. RNA was transcribed into cDNA using Thermofisher (Waltham, MA, USA) Reverse Transcription RNA to cDNA kit. qPCR was run using the transcribed cDNA and BioRad (Hercules, CA, USA) SYBR Green Master Mix that binds to double-stranded DNA to quantitatively track the progress of DNA amplification in real-time. Primers used were: Inflammatory (IL-4, IL-6, IL-9, IL-10, IL-11, Nκβ), oxidative stress (iNOS), cell death (Casp-3), and cellular activation markers (Ki67, CD68, GFAP, Synapsin, CD11b, Vim), and a housekeeping gene (GAPDH) (Table 2.1). The qPCR runs at 95 °C for 30 s, 95 °C for 5 s, and then 60 °C for 30 s for 40 cycles. The gene expression changes in OGD-conditioned and BEV

treatment groups were normalized to the healthy controls to quantify fold-expression change. Results were statistically analyzed with one-way ANOVA (Kruskal–Wallis multiple comparison tests) and normalized by the median Ct value for all samples.

Gene	NCBI Reference Sequence	Forward Primer	Reverse Primer
GAPDH	NM_017008.4	ACTCCCATTCTTCCACCTTTG	ACTCCCATTCTTCCACCTTTG
IL-4	NM_201270.1	GTCACTGACTGTAGAGAGCTATTG	CTGTCGTTACATCCGTGGATAC
IL-6	NM_012589.2	GAAGTTAGAGTCACAGAAGGAGTG	GTTTGCCGAGTAGACCTCATAG
IL-9	NM_001105747.1	GAAGGACGACCCATCATCAAA	ACGGTGTGGTACAATCATCAG
IL-10	NM_012854.2	AGTGGAGCAGGTGAAGAATG	GAGTGTCACGTAGGCTTCTATG
IL-11	NM_133519.5	CTAGCACTTCAAAGGTCCTCAA	ACACCTTGAACCTTGCTATCTC
Ki67	NM_001271366.1	CACACACAAAGAGCCCATAGA	GATTCCTCCTGCCGGTTAAA
Nκβ	NM_001276711.1	GGTTACGGGAGATGTGAAGATG	GTGGATGATGGCTAAGTGTAGG
CD68	NM_001031638.1	CTTGGCTCTCTCATTCCCTTAC	TGTATTCCACTGCCATGTAGTT
Vimentin	NM_031140.1	CTTCCCTGAACCTGAGAGAAAC	GTCTCTGGTTTCAACCGTCTTA
GFAP	NM_017009.2	AAAGACACTGAAACAGGAGAGAG	GGACTGAGCAACCAGGAATAG
Synapsin	NM_001110782.2	GGACGGAAGGGATCACATTATT	ACCACAAGTTCCACGATGAG
CD11b	NM_012711.1	GAGCACCATCTGGGACATAAA	GGCATCAGAGTCCACATCAA
iNOS	NM_012611.3	TGGAGCGAGTTGTGGATTG	CCTCTTGTCTTTGACCCAGTAG
Casp-3	NM_012922.2	GAGCTTGGAACGCTAAGA	CTGACTTGCTCCCATGTAT

Table 2.1. Sprague-Dawley Rat mRNA Primer Design for qPCR.

2.2.11. Statistical Analysis

Statistical analysis was performed in GraphPad Prism version 9.2.0 (GraphPad Software, San Diego, CA, USA). Graphs for the cell features compared to the control and treatment groups and compared to shape modes are displayed as the median with interquartile range and all data points are shown. Morphology features were compared across all groups using a nonparametric One-Way ANOVA utilizing the Kruskal–Wallis

test and Dunn's post hoc correction for multiple comparisons. All p-values < 0.05 were considered statistically significant.

2.3. Results

2.3.1. Isolating BEVs from Whole Neonatal Brain Tissue

Recent papers suggest that while several different techniques exist for EV sequestration, such as ultracentrifugation (UC), size exclusion chromatography (SEC), and density gradient (DG), a combination of two or more of these methods improve EV throughput.[78, 79] For this project BEVs from saline-perfused P10 male rat brains were isolated using a combination of UC, SEC, and ultrafiltration (UF). The size and number of BEVs were characterized using nanoparticle tracking analysis (NTA). NTA results for BEVs showed a mean size distribution of 100–300 nm (Figure 2.1 A-B)—representative of the size regime of exosomes and small microvesicles—and a concentration that averaged 3.2×10^{11} particles/mL among formulations. To put this value into perspective, blood has an estimated concentration of about $5–15 \times 10^{8}$ particles/mL. NTA results reported a purity similar to published tissue-derived EV values, confirming that our methods were appropriate for BEV purification[78]. The zeta potential of BEVs was on average measured to be −14.1 mV.

2.3.2. Characterization and Validation of BEVs

Characterization and validation of BEVs was performed following successful isolation methodology. We visualized the geometry of isolated BEVs using transmission electron microscopy (TEM) through negative and positive staining (Figure 2.1C). The negative stain coats the background with heavy metal, allowing electrons to travel more easily through the vesicle. This created high contrast between the background and

clearly delineated the lipid bilayer of the BEVs. Meanwhile the positive stain coats organic material lining the surface of BEVs, which revealed surface texture likely due to membrane biomolecules such as lipids and proteins, in addition to the lipid bilayer. Together, these images provided information about the vesicular geometry and topology of BEVs.

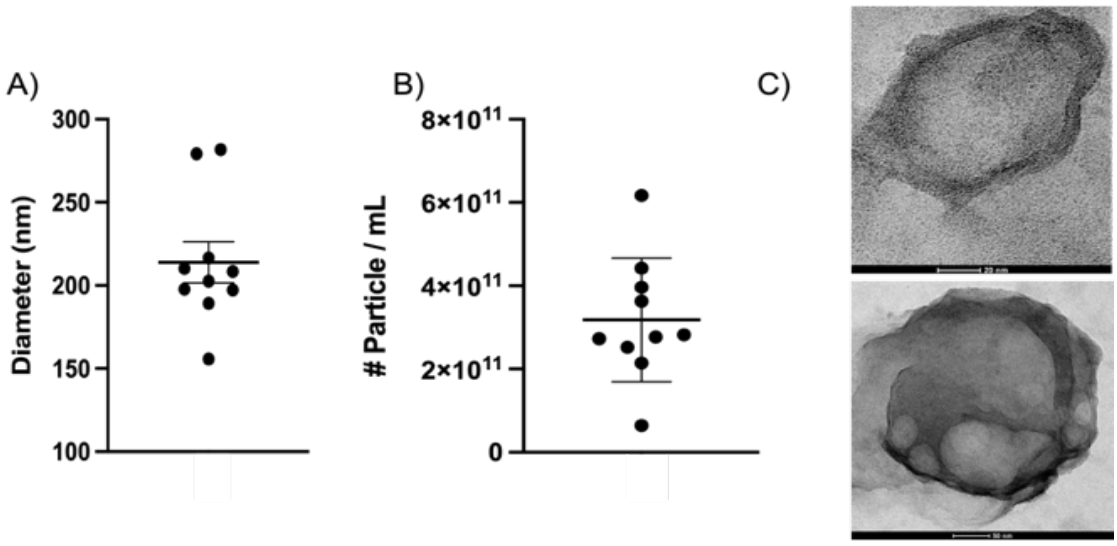

Figure 2.1. Characterization of BEVs.
Average A) diameter and B) concentrations (#particle/mL) across all BEV extracts as measured by NTA and BCA. Each point represents one unique sample (N=10). The mean diameter and concentration across all isolates are 213.9 nm and 3.2 x 10^{11} particles/mL, respectively. C) Transmission electron microscopy (TEM) closeup of isolated BEVs using negative staining (top) and positive staining (bottom) with visible lipid membrane structure. BEVs ranged from 30-200nm, supporting NTA data. Scale bars = 20nm (top), 50nm (bottom).

Following visual confirmation of EVs using TEM, the identity of isolated BEVs was quantitatively validated using dot blot immunodetection on BEV and brain tissue lysates after lysis with 1X radioimmunoprecipitation buffer (RIPA). The presence of target proteins CD9, CD63, and GM130, and housekeeping protein GAPDH were tested among the samples. It is expected that BEV fractions would contain positive EV

markers CD9 and CD63, while lacking EV negative marker GM130. Brain tissue lysate was used as a positive control and is expected to express all proteins tested. Conversely, 1X PBS served as a negative control and was not expected to express any signal.

As expected, the 1X PBS control produced no fluorescence, while the brain tissue lysates (for all dilution factors) showed strong fluorescent signals for all targeted proteins (Figure 2.2). Using the image processing platform ImageJ, we quantified the total detected fluorescent signal and computed the integral signal density values within a selected region of interest to serve as a proxy for the total amount of protein assessed in the sample. Detection of EV positive markers, tetraspanins CD9 and CD63, were confirmed in all blots containing BEV and brain lysate. As expected, the BEV lysate showed negligible signal for negative EV biomarker GM130 (0.004 signal density), confirming that BEV samples were free of cellular contaminants otherwise found in brain tissue.[80]

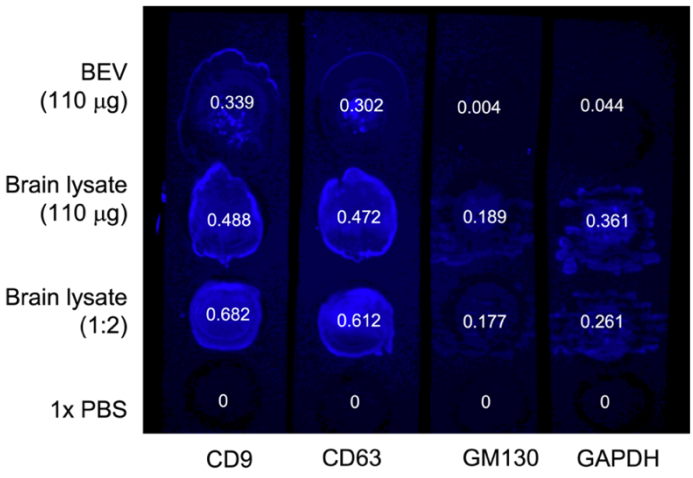

Figure 2.2. Dot blot immunodetection of EV proteins.
Immunoblot panel of BEV lysates compared to brain tissue (BT) lysate and a negative control. Samples (top to bottom) are BEV lysate, BT lysate, BT lysate (1:2 dilution in PBS), and PBS (negative control). Each PVDF membrane strip was probed with a different primary antibody for a specific target protein (left to right): CD9, CD63, GM130, and GAPDH. Each spot contained 110μg (or 55μg) of sample protein in a volume of 15μL as measured by BCA. The total

fluorescent signal density of each dot was normalized by the negative control (PBS), quantified in ImageJ, and labeled in the corresponding dot.

From integral signal density quantification of the BEV lysates, we determined that CD9 had the greatest abundance of all measured proteins (0.339), followed by CD63 (0.302) and GAPDH (0.044). A signal density ratio quantifies the abundance of target proteins extracted in the BEV lysate compared to brain tissue lysate (signal density ratio = signal density of BEV/signal density of brain tissue lysate). The signal density ratios for CD9, CD63, GM130, and GAPDH are 69.5%, 64%, 2.12%, and 12.19%, respectively. Based on these immunoblotting results, we validated the identity of EV isolates used for these studies, with CD9 being the most abundant target tetraspanin.

2.3.3. BEV-Mediated Therapeutic Effects on an Ex Vivo Ischemic Slice Model

Having successfully isolated and characterized BEVs, we sought to address the overarching question of whether BEVs confer therapeutic effects within an HI model. To study EV therapeutic activity and its impact on cellular behavior, we performed OGD on organotypic whole hemisphere OWH slices from the P10 rat brain to model HI in term-equivalent neonates.[11, 67] Following OGD conditioning, we topically applied 5 µg, 12.5 µg, 25 µg, and 50 µg BEV dosages on slices at various timepoints (Figure 2.3 A). Healthy and OGD control slices did not receive any BEV treatment. Comparing cellular cytotoxicity values among *ex vivo* slices revealed several important trends. First, the percent cytotoxicity expectedly decreased over time in both the healthy and OGD control conditions as tissues recovered from acute slicing (Figure 2.3 B). [67] Second, 25 µg is the observed minimum therapeutic dosage beginning at 24h exposure. At this exposure time, the percent cytotoxicity was not statistically significant from the healthy control but was statistically significant from the OGD (0 µg BEV) control ($p < 0.0001$).

This reveals that 24h is the observed minimum exposure time necessary to elicit a therapeutic response at the minimum therapeutic dosage. Third, the percent cytotoxicity across 5–50 μg dosages were statistically insignificant from the healthy control at 48h exposure time ($p > 0.999$), which is regarded as the therapeutic exposure time.

Though it was determined that 25 μg and 48h were the therapeutic dose and exposure time for our model, another important clinical parameter to investigate is the therapeutic window for BEV treatment. Defining a treatment window during which BEVs retain their therapeutic efficacy is especially critical in neonates given that subtle symptom presentation during HIE onset usually results in delayed medical treatment. To test for the therapeutic window, BEV treatment was administered to OGD conditioned slices at various application timepoints before and after OGD onset (−24, 4, 24h). Noticeably, there were extended time periods when all 5–50 μg dosage groups elicited therapeutic effects resulting in cell viability at similar levels to the healthy control (Figure 2.3C). This result occurred in BEV application as early as 4h post-OGD and as late as 24h post-OGD and indicates that the therapeutic window of administration can extend up to a day post-injury. The results from this experiment suggest that BEV application is therapeutically effective even when administered several hours after injury onset.

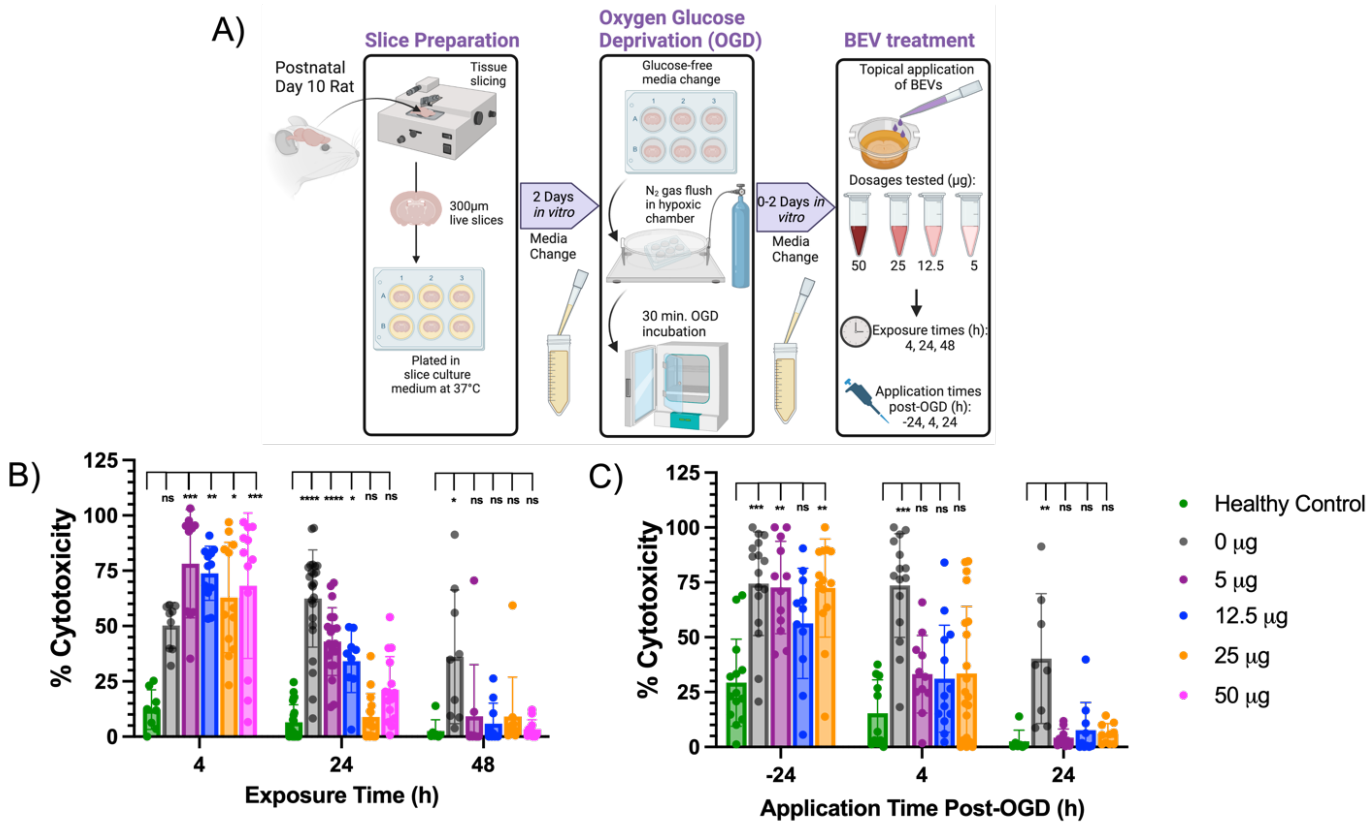

*Figure 2.3. Cytotoxicity in Hypoxic-Ischemic Brain Slices Following BEV Treatment. A) Timeline of ex vivo OWH slicing, OGD conditioning, and BEV treatment prior to outcome assessment to determine the therapeutic efficacy of BEVs. On DIV1 ex vivo slices are placed into a permeable PTFE membrane submerged in 5% SCM and incubated at 37℃ and 5% CO_2 for recovery post-acute slicing for 2 days. OGD conditioning for 30 minutes is performed on DIV4, followed by application of BEVs at various dosages (5μg, 12.5μg, 25μg, and 50μg) and application timepoints (-24h, 4h, 24h). B) Slices were immediately treated with BEVs following OGD conditioning for varying exposure times of 4, 24, and 48h. 25μg and 50μg dosages led in significant decreases in cell death compared to 0μg control across all timepoints with at least 24h of exposure. C) Slices were treated with BEVs at varying application timepoints: 24h pre-OGD (-24h), and 4 and 24h post- OGD for 24h. BEVs retained therapeutic viability when applied up to 24h post-injury. Percent cytotoxicity was determined using PI cell viability assay and cytotoxicity was normalized by cell number (N=3 slices per group, 4-6 cortical images per slice). Significance was determined by multiple group Kruskal-Wallis testing (ns=not significant, *p< 0.05, **p<0.01, ***p<0.001, ***p<0.0001). Modified from Nguyen et. al.*

2.3.4. mRNA Expression Changes in Response to BEV Treatment

Though brain slices exposed to BEVs demonstrated therapeutic effects within our *ex vivo* model, it remains unclear what cytokines and regulatory factors are involved. In addition to assessing cell viability via confocal imaging, RT-qPCR was used

to further quantify BEV therapeutic activity on *ex vivo* OGD slices by measuring changes in gene expression levels following treatment. RT-qPCR was run on a subgroup of slices to evaluate temporal changes in the gene expression profiles of inflammatory (IL-4, IL-6, IL-9, IL-10, IL-11, N κβ), oxidative stress (iNOS), cell death (Casp-3), and cellular activation markers (Ki67, CD68, GFAP, Synapsin, CD11b, Vim) (Table 2.1) following BEV treatment at 25 µg for 24h (Figure 2.4). At 24h, slices with BEV treatment showed a significant increase ($p = 0.037$) in the expression of anti-inflammatory cytokine IL-10 compared to the OGD control (Figure 2.4**).** After 24h, there were no significant changes in expression of cell activation and cell death markers profiled in this study.

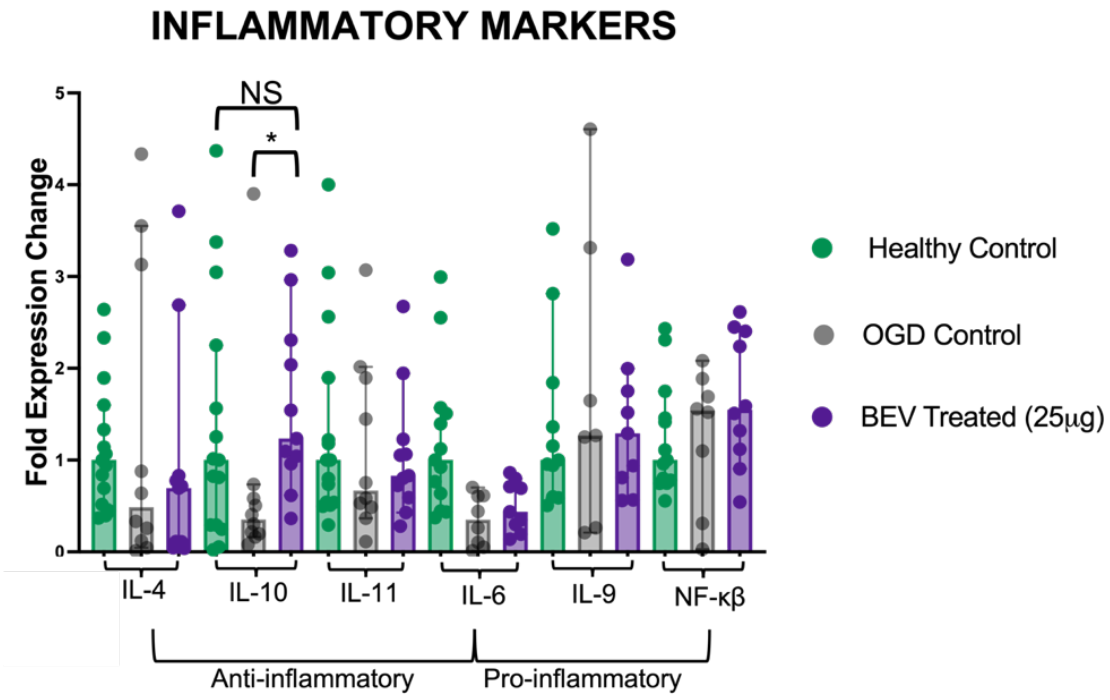

Figure 2.4. RNA quantification in ex vivo slices.
*Fold-changes of inflammation mRNA markers in healthy, OGD-conditioned, and BEV treated ex vivo slices following 24hexposure (N = 7–15 RNA samples (3 replicates per sample)); median ± 95% confidence interval; ns: not significant, * = p < 0.05).**mRNA markers tested, but showed no significance after statistical analysis: 1) cell death and stress: iNOS & Casp-3, 2) cell*

proliferation: Ki67, Synapsin, CD68, 3) cell activation: GFAP (astrocytic), CD11b (microglial), Vim (neuronal). Modified from Nguyen et.al.

2.3.5. Morphological Response of Glial Cells to BEV Treatment

Microglia are glial cells whose phenotypes provide ample information about the biological state of the brain.[81] Due to their extensive involvement in injury response within the brain, microglia morphology is used as a proxy through which inflammation and injury progression can be measured within the OGD model. Several shape features of microglia were compared across healthy control, OGD control, and BEV treated slices at varying exposure times—4 h, 24h, and 48 h.

Qualitative differences in cellular density and morphology were observed in representative images of microglia stained with Iba-1 across the healthy, OGD, and BEV-treated slices at 24h (Figure 2.5). The healthy control slices showed the highest microglia density, followed by BEV-treated slices, and finally OGD control slices with the lowest density. Microglia from healthy and BEV-treated slices also displayed greater extent of ramification than microglia from OGD control slices.

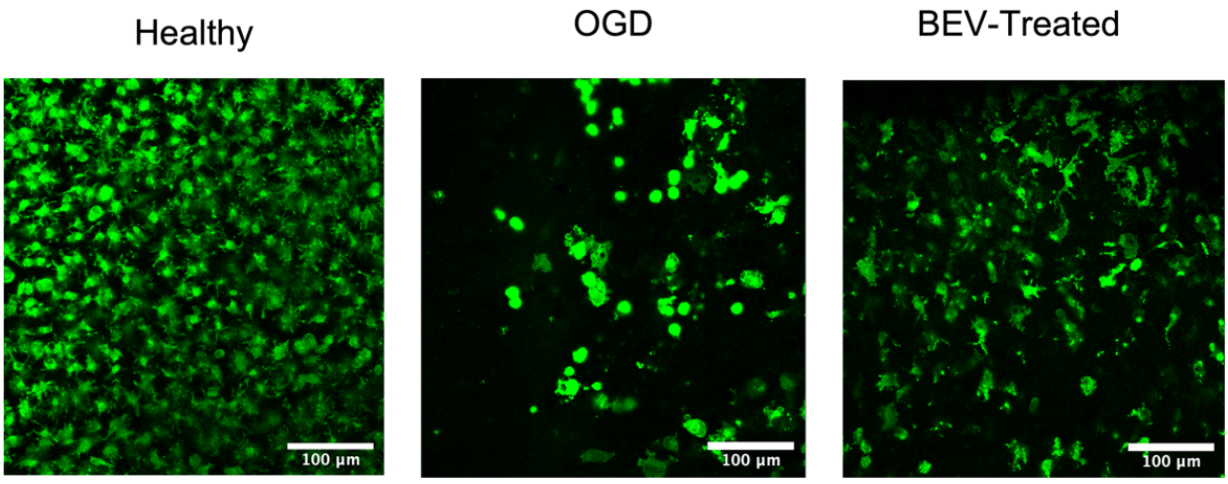

Figure 2.5. Representative confocal imaging examples of microglia (stained with anti-Iba-1) at 40x magnification.

These images were taken from the cortical region of ex vivo healthy control, OGD control, and 25μg BEV-treated slices at an exposure time of 24h. Scale bars: 100 µm.

Quantitative analysis of microglia shape features was completed with Python-based image processing (Figure 2.6). While fluctuations in morphology during the first 24hmay be due to natural microglial heterogeneity, changes in perimeter, area, circularity, and aspect ratio were observed in BEV-treated slices between the 24h and 48h exposure times. After 24h the microglia from BEV-treated slices showed no significant difference from the OGD control slices in perimeter, area, circularity, and aspect ratio. However, this trend changes at the 48h time point as the microglia from BEV-treated groups become statistically differentiable to the healthy and OGD controls in every feature except perimeter (area: $p < 0.0001$ for both healthy and OGD controls; circularity: $p < 0.0001$ for both healthy and OGD controls; aspect ratio: $p = 0.0002$ for healthy control, $p = 0.0097$ for OGD control). Specifically, the median area and circularity of the BEV-treated microglial cells decreased while the median aspect ratio and perimeter increased. Meanwhile, the OGD control slices observed increases in the median value of circularity, area, perimeter and observed relatively no change in median aspect ratio. The healthy control slices observed an increase in median value for circularity and a decrease in the median value for area, perimeter, and aspect ratio.

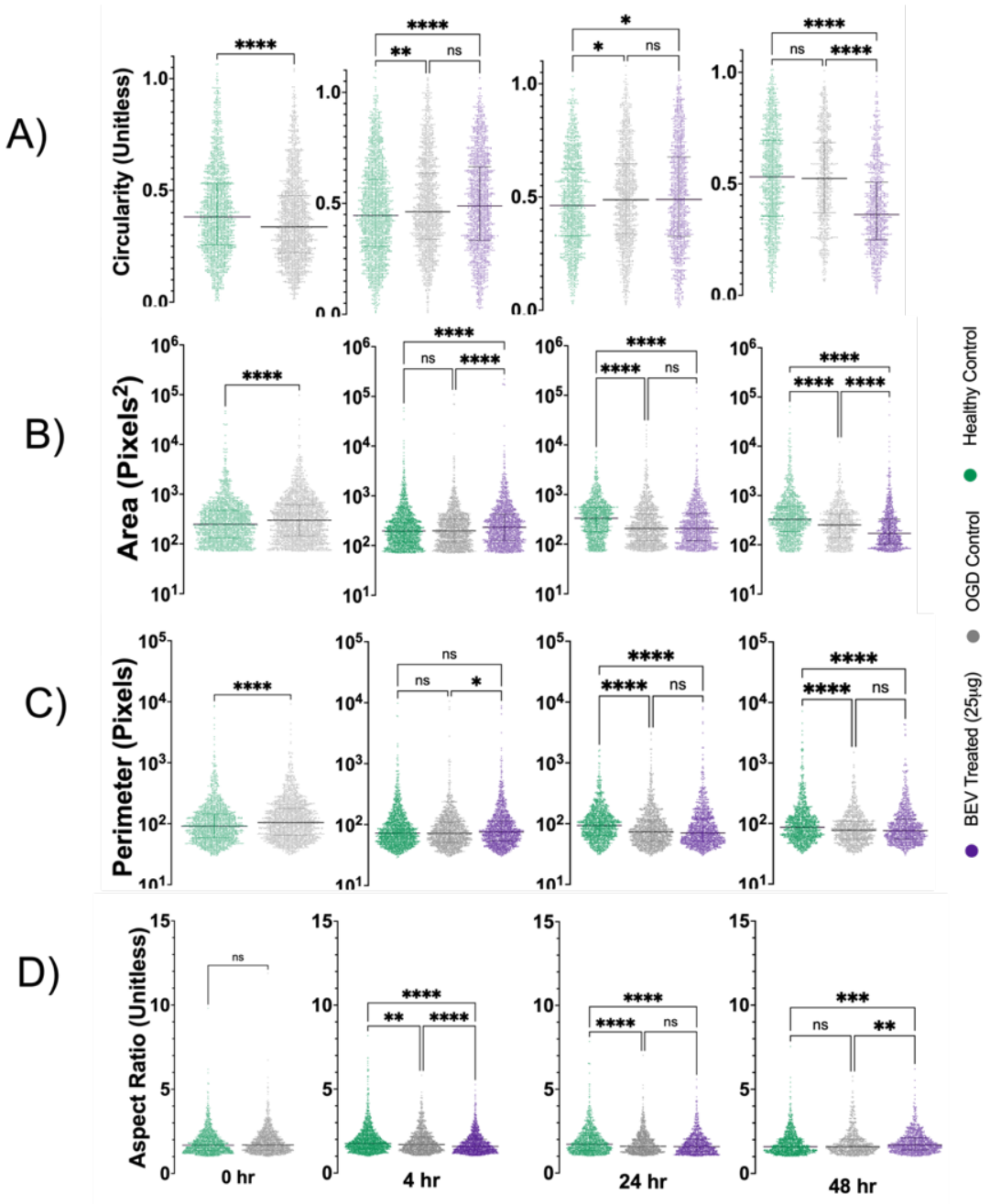

*Figure 2.6. Cell morphology analysis across treatment groups and exposure time. Quantification of microglial geometric parameters: A) Circularity, B) Area Coverage, C) Perimeter, D) Aspect Ratio. Graphs display median with interquartile range. * (p<0.05), ** (p<0.01), *** (p<0.001), and **** (p< 0.0001) indicate significant difference with Kruskal-Wallace test adjusted for multiple comparisons. Modified from Nguyen et.al.*

Using the VAMPIRE image analysis package to categorize cell shapes, microglia were split into five distinct shape modes (SM) and graphed for perimeter, area,

circularity, and aspect ratio (Figure 2.7A). Representative images of the original Iba-1 stain, segmented microglia, and color-coded SMs are displayed alongside a representative dendrogram of the PCA and SMs determined by k-means clustering (Figure 2.7B). SM3 represents a circular microglial shape with the highest circularity yet smallest perimeter, area, and aspect ratio. SM1 and SM5 were statistically indifferentiable amongst the four geometric features analyzed and correlated with branched microglia with little to no swelling, as these SMs have the highest perimeter and area and the lowest circularity. SM2 and SM4 were also nearly indifferentiable from each other, but SM4 has a significantly higher aspect ratio. The aspect ratio differences between SM2 and SM4 may indicate that SM4 has increased process extension or unidirectional branching in comparison to SM2.

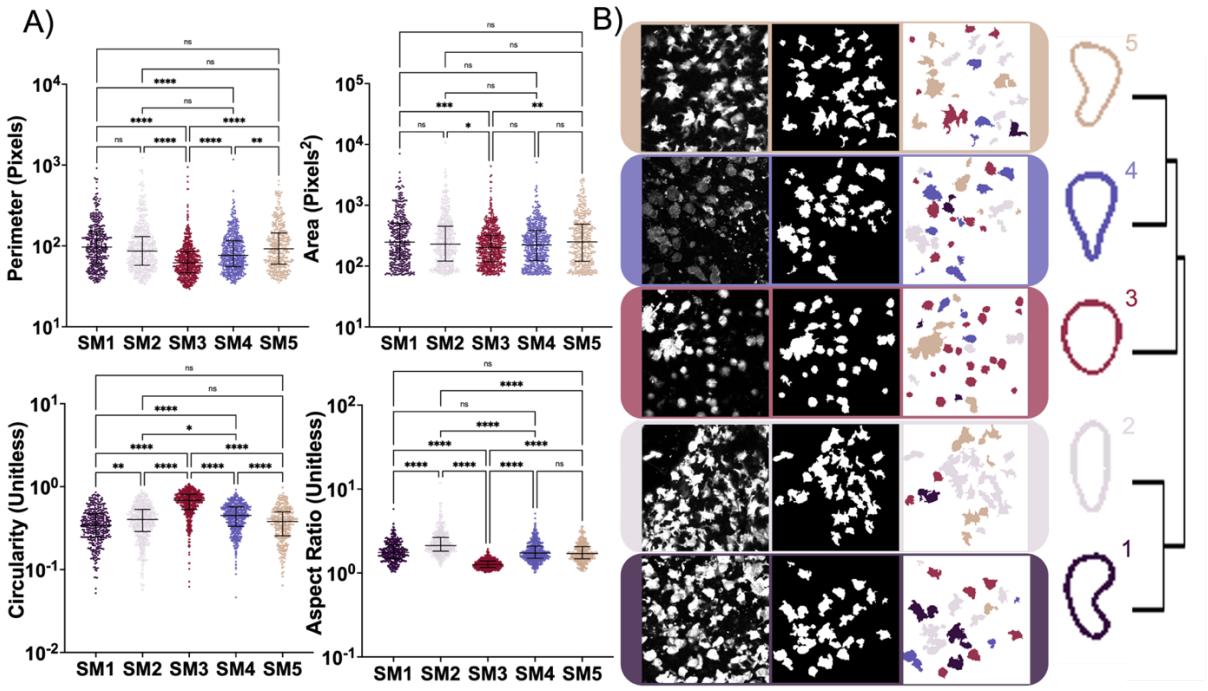

Figure 2.7. Comparison of VAMPIRE generated cell shape modes by geometric parameters.

*A) Morphology parameters for the five VAMPIRE SMs. Graphs depict median with interquartile range. * (p<0.05), ** (p<0.01), ***(p<0.001), and **** (p<0.0001) indicate significant difference with Kruskal-Wallace test adjusted for multiple comparisons. B) Segmentation procedure shown with the original cell image, Li Threshold image, and labeled by color to represent each of the shape modes (colored according to dendrogram on right) after VAMPIRE method.*

To demonstrate morphological heterogeneity frequencies of all SMs were visualized as a heat map across every exposure time—0, 4, 24, and 48 h—and for all three experimental groups—healthy control, OGD control, and BEV treatment (Figure 2.7). SM3 and SM4 exhibited the highest overall frequency with the peak of SM3 occurring at 24hand the peak of SM4 occurring at 0 and 4 h. SM 1 and 5 exhibited the lowest frequencies with the lowest overall frequencies occurring in SM 5 at 24h. The BEV-treated slices showed the lowest microglial heterogeneity at 24hwhen SM3 dominated at 37% and both SM1 and SM5 were at 12%. However, at 48hthe BEV-treated slices showed the highest microglial heterogeneity with the most evenly dispersed frequencies across all groups and exposure times.

Exposure	Treatment	Shape Mode 1	Shape Mode 2	Shape Mode 3	Shape Mode 4	Shape Mode 5
0 hr	healthy control	16.3	15	21.5	29.6	17.6
	ogd control	17.7	23.8	20.4	21.4	16.7
4 hr	healthy control	18.5	23.3	15.1	25.3	17.8
	ogd control	17.9	13.5	20.8	31.4	16.4
	bev treatment	12.3	20.3	29.5	21.2	16.7
24 hr	healthy control	14.9	24.3	26	22.1	12.7
	ogd control	17.6	19.9	34.1	15.3	13.1
	bev treatment	12.2	21.8	36.5	17.3	12.2
48 hr	healthy control	15.6	15.6	37.4	19	12.3
	ogd control	15.2	23.2	28	17.6	16
	bev treatment	22.5	17	21.7	21.7	17

Key: Percent Shape Mode	12	17	21	27	38

Figure 2.8. Global heatmaps of percent shape mode by exposure time and treatment condition. Adapted from Nguyen et. al.

2.4. Discussion

EVs initiate and promote a therapeutic injury response in adult stroke models by releasing neuroprotective, neurogenic, and anti-inflammatory factors and have high

potential to be translated into the neonatal therapeutic space. However, most studies and all ongoing clinical trials evaluating EV therapeutic potential are performed on adult models using stem cell-culture derived EVs, which do not recapitulate EV activity in their endogenous environment. Here, we investigated the therapeutic potential of BEV administration on an OWH slice culture model of neonatal HI. We showed that BEVs can be successfully isolated from whole brain tissues by using a combination of UC, SEC, and UF techniques. Independently, these are standard techniques in EV research but using them in combination allowed for increased EV yield and purity as quantified by NTA and BCA. We validated the identity of BEV using dot blots targeting positive (tetraspanins CD9, CD63) and negative (GM130-a membrane protein of the Golgi Apparatus) EV markers compared to brain tissue lysate. Positive markers were detected in both the BEV and brain tissue lysates, while negative EV markers were only present in brain tissue lysate confirming the identity of isolated BEVs. Both the negative control (1X PBS) and negative EV marker GM130 had negligible signal density values in BEV lysate, which is indicative of BEV purity. It is difficult to address the purity of the BEV samples, as quantitative standards have not been set due to inconsistent methods utilized between research groups for EV isolations.[28] This problem is compounded by the diverse sources from which EVs are extracted. The wide range of EV sequestration methods result in highly heterogenous distributions of EV size across the literature. Here I report data from the BEV isolates used for this project, including size distribution, and concentration to provide comprehensive characterization of our BEV isolates (Table

2.2).

EV extract #	Mean Diameter (nm)	Mode Diameter (nm)	Particle #	Purity (Particle/mL)
1	279.3	227.5	2.73E+11	5.76E+08
2	155.8	132.3	2.82E+11	4.35E+08
3	197.3	144.2	3.63E+11	9.65E+08
4	208.4	138	2.52E+11	4.00E+08
5	197.8	139.2	2.14E+11	5.46E+08
6	216.6	129.5	6.17E+11	1.43E+09
7	210.2	140	2.77E+11	4.09E+08
8	189.3	145	4.42E+11	4.11E+08
9	281.7	180	6.42E+10	7.14E+07
10	146.1	202.5	3.96E+11	6.91E+08

Table 2.2. Characterization data from BEV extracts used in dose- and time- dependency studies.

We performed dose- and time-dependency experiments to evaluate the therapeutic potential of BEVs in an HI brain slice model. We observed a decrease in the percent cellular cytotoxicity over time in the healthy and OGD control conditions as the slices naturally recover from acute slicing, aligning with previous outcomes in our OGD slice model in rats.[67] Results from these therapeutic efficacy studies suggest that 25 µg of BEVs is the minimum therapeutic dosage after 24h exposure time. At this dosage and exposure time, BEV-treated slices and the healthy control display comparable cytotoxicity values. Notably, at 4h of exposure time all BEV dosages elicited an increased cytotoxicity compared to the OGD control. However, this increase was not observed at 24h. We hypothesize this may be due to a delayed activation of immune response following injury onset that occurs between 4 and 24h.[82] Additionally, 48h is considered as the therapeutic exposure time for which cellular cytotoxicity significantly decreased following BEV treatment across all tested dosages.

We sought to determine the therapeutic application window of BEV treatment following OGD conditioning. Cellular cytotoxicity values for tissues treated with BEVs were similar to the healthy control at all dosages when applied between 4 and 24h post-OGD conditioning. This indicates that the application window of BEVs spans at least 24h following injury onset. In our interpretation, this heightened therapeutic activity suggests that BEV treatment may directly interact with important cells regulating injury response during peak immune activation period within 24h post-injury.[82] Unexpectedly, 24h BEV priming of the *ex vivo* slices before OGD (−24h) in our time-dependent experiments (Figure 2.3 C) did not demonstrate increased therapeutic response. It may be that priming will be more efficient closer to the period of injury onset, or that priming requires cell-specific BEVs to trigger neuroprotective factors that will lead to a decrease in cell cytotoxicity. To reduce the number of animals used, we did not run 50 µg dosage experiments for all timepoints because 25 µg was previously determined as the therapeutic dosage. Dosages greater than 25 µg could continue to elicit observed therapeutic trends, but this may not be necessary as 25 µg drove cytotoxicity values down to levels comparable to the healthy control after 24h (*Figure 2.3*).

Furthermore, all slice studies were sex-controlled using only male pups because males often have worse outcomes in neurological injury than females.[71] While 25 µg BEV is presented as the minimum therapeutic dosage for ischemic male rat pups, this dose may be lower for a pup with a lesser injury severity regardless of sex. Future studies investigating the role of sex-dependent BEV injury attenuation will provide insight into the biological conditions affecting BEV therapeutic efficacy.

While our cytotoxicity evaluations did indeed demonstrate reduced cytotoxicity in the BEV-treated slices, we evaluated qPCR on two cell death markers: iNOS and Casp-3. qPCR results indicated no difference in these specific cell death markers. Therefore, it is likely to be the case that BEVs impact another pathway not explored in this paper. Other studies have found that EVs influence other apoptotic markers such as BCL2 Associated X (Bax),[54] superoxide dismutase 1 (SOD-1),[32] Bcl-2 and nineteen kilodalton-interacting protein 2 (BNIPS),[56] and osteopontin (OPN).[49] It is also possible that rather than influencing cell death pathways directly, BEVs impact the expression of cell survival pathways such as extracellular signal-regulated kinase 1 (Erk1) and Erk2[32] or prion protein (PrP)[49]. These mechanisms of effect can be explored in future studies.

Results from whole slice qPCR analysis also demonstrated a significant increase in anti-inflammatory gene expression for IL-10 in BEV-treated slices compared to the OGD control group after 24hexposure. In particular, IL-10 expression after BEV treatment is comparable to the healthy control, pointing to the role that BEVs play in regulating injury attenuation back to healthy levels. IL-10 is a critical anti-inflammatory cytokine, and the upregulation of IL-10 mRNA expression suggests that BEVs play a role in alleviating inflammation in injured tissues through elevating IL-10 anti-inflammatory expression.

Gene expression analysis was paired with the phenotypic profiling of microglia that provided information about inflammation, disease onset and progression, and stimuli from the local environment. Classically, a swollen and amoeboid-like phenotype is connected to a pro-inflammatory active microglia, while a ramified and branched phenotype is connected to a less-inflammatory, resting state.[81] Microglial differentiation

between BEV treatment, OGD controls, and healthy controls was quantified over several key morphologic features on both an individual and population-based level. On the individual level, microglia in BEV-treated groups demonstrated unique morphological changes between 4–48hof BEV exposure. At 4 h, microglia in both the BEV treated slices and OGD slices show significant increases in circularity from the healthy control slices, suggesting swelling of microglia. Swollen, thicker microglia are correlated with a pro-inflammatory state, which is confirmed by increased cytotoxicity and pro-inflammatory marker expression at 4hof BEV exposure. Microglia from BEV-treated slices start to exhibit significant morphological changes from OGD controls at 48 h. The microglia from BEV exposure at 48hdisplayed decreased median area and circularity with an increased aspect ratio, which suggests that the microglia are entering more elongated shapes. Elongation with decreased area also indicates a decrease in swelling associated with a less inflammatory microglial state. This microglial shift between 24–48htowards an anti-inflammatory state confirms the therapeutic effects demonstrated via cytotoxicity and qPCR results at this critical timepoint.

This morphological shift between 24–48h is also observed at the population-level in microglia exposed to BEV treatment. Using the SMs obtained via VAMPIRE, overall morphological changes in the microglial population were compared across treatment groups and exposure times. Microglia across all conditions displayed increased homogeneity of microglial phenotypes at 4h and 24h, which is to be expected during initial injury response period. However, at 48h, while the OGD and healthy control homogeneity increases, microglia from BEV-treated slices become more heterogeneous and transition into a branched and less swollen SM. Strikingly, the increase in

heterogeneity and increased IL-10 marker from qPCR analysis in BEV-treated slices suggests that the microglia not only transition out of a pro-inflammatory state between 24 and 48 h, but also enter into a different morphology that might be a more restorative phenotype compared to the resting state characteristic of the healthy control. Changes in microglial morphology reveal that BEV administration has dose- and time-dependent impacts upon immune cell activation in a neonatal HI model. Though no significant changes in cell activation or cell death marker expression were observed at 24hof exposure, it is hypothesized that these changes will occur at 48hto reflect the time-dependent shift observed in microglia morphology. Future studies evaluating chronologic changes in gene expression will be valuable in bridging changes in microglial morphology with cellular response in an HI model following BEV administration.

Multiple P10 rat brains are required for each BEV extraction sample, so tissues from pups of the same litter and sex were pooled together to reduce biological variability amongst samples. Despite our efforts to reduce biological variability, there may still be discrepancies between pups from different litters that affect our results. For example, pups that are malnourished are likely to have under-developed brains that may impact the severity of immune response to injury. The small mass of neonatal brains in animal models poses a limitation in the scalability of BEV research. It should be noted that when considering the translation of this work into a clinical setting, it is not the intention that BEVs will be derived from the neonatal brain and administered into patients. Rather, the goal of this research is to first establish the therapeutic efficacy of BEVs in ischemic attenuation, so that future directions of our work can focus on teasing apart

specific aspects of protection against injury. Clinical translation of this work will involve comparing the protective mechanisms and payloads imparted by BEVs to conventional forms of cell culture-derived EVs, such as mesenchymal stem cells. Understanding endogenous BEV activity in a neonatal ischemic model will inform the design of EV therapeutics from the bench into clinical use. While we demonstrated that BEVs elicit dose- and time-dependent therapeutic effects when applied to OGD conditioned slices, endogenous EVs exist in a heterogeneous population within the brain. Therefore, all results reported in this paper are indicative of treatment from the BEV population represented by EVs derived from different cell types.

2.5. Conclusion

EVs have gained much interest due to their emergence as important players in injury response, neuronal development, and proliferation within the adult brain. We investigated the dose- and time-dependency of BEV treatment on an *ex vivo* slice model of HI. In contrast to existing studies, we performed experiments using whole brain tissue derived EVs to recapitulate the therapeutic potential of endogenous EVs on neonatal is- chemic models. In summary, we showed that BEVs can be successfully derived from whole neonatal rat brain tissue through a combination of EV isolation and purification techniques. BEV treatment of ex vivo HI slice models decreased cellular cytotoxicity at a minimum therapeutic dose of 25μg and a therapeutic exposure time of 48h, and has an application time window up to 24h post-injury. We observed a shift in microglial morphology from pro-inflammatory amoebic to anti-inflammatory and restorative shape modes following BEV administration. Analysis of changes in gene expression profiles indicated that BEVs significantly increased anti-inflammatory IL-10

cytokine expression. Collectively, our results reflect the promising therapeutic role that BEVs play in attenuating inflammation and cell death in HIE neonatal models. Future research in BEVs can inform the design and administration of therapies for improving outcomes for neonatal HIE patients.

CHAPTER 3. DESIGNING NOVEL OLIGONUCLEOTIDE BIOBARCODE TAGS TO TRACK EXTRACELLULAR VESICLE FATE

Nam Phuong Nguyen, Michelle Asencio, Shahrokh Paktinat, Elizabeth Nance, Lucia Vojtech

This chapter is in preparation to be submitted in 2024 under the title “Novel Oligonucleotide Biobarcodes for Labeling Extracellular Vesicles."

3.1. Abstract

Current methods for visualizing the trafficking of extracellular vesicles (EVs) rely on fluorescent labeling and microscopy to reveal their location. However, these methods are not fully quantitative and suffer from false-positive signals and unfavorable signal-to-noise background when analyzing tissue samples. Furthermore, they require specialized microscopes and instrumentation which are expensive, not accessible in many locations, and necessitate extensive user training. Here, we sought to develop a method to label EVs with short oligonucleotide “biobarcodes”, enabling detection in tissues using standard quantitative PCR techniques. We engineered a short (22 base) DNA oligonucleotide based on the *C. elegans* microRNA cel-miR-39 that was modified with a 5-prime amine group for click chemistry conjugation to the EV surface. Additional phosphorothioate bonds increased stability against exonucleases when applied *in vitro, ex vivo,* and *in vivo*. We successfully conjugated the oligonucleotide barcodes (oligobarcodes) to EVs isolated from human semen (SEVs) and from whole neonatal rat brains (BEVs) and administered to *in vitro* cell or *ex vivo* tissue cultures to examine the fate of SEVs and BEVs with different cell populations. To detect the oligobarcoded SEVs (oligo-SEVs) we utilized a three-step PCR protocol using stem-loop primer and

pre-amplification, followed by quantitative PCR with an assay utilizing a locked-nucleic acid fluorescent probe. Compared to unconjugated oligonucleotide (blank oligo), we detected significantly more signal in cells treated with oligo-SEV, suggesting that SEVs drive cell interaction and uptake. Similar to results from literature using fluorescent imaging studies, oligo-SEVs were preferentially located with antigen-presenting cells (APCs) in digested vaginal tissue samples as well as in *in vivo* murine genital tracts. Our oligonucleotide barcoding methodology offers a novel method for labeling EVs from any source and provides quantitative, translatable, and microscope-free analysis of cellular EV uptake that can be used in *in vitro*, *ex vivo*, and *in vivo*.

3.2. Introduction

Extracellular vesicles (EVs) are lipid-bound nanoparticles that are released by every cell type in the body and contain a wide repertoire of biomolecules involved in critical physiological pathways.[83-85] Though the mechanisms of EV biodistribution and cell-specific uptake remain unclear, EV cargo can be transferred to neighboring or distant cells, acting as an important mode of intercellular communication.[26, 86] EVs are an attractive alternative to traditional synthetic nanoparticles for drug delivery due to their critical roles in cell communication, therapeutic potential, and ability to carry cargo and be trafficked to recipient cells with low immunogenicity.[24, 63, 87-89] For effective translation of EVs into the therapeutic space there is a need to monitor the uptake and localization of EVs within cells and tissue to quantify EV biodistribution and behavior in physiological environments. However, monitoring EV localization within cells, tissues, and biofluids is challenging due to their small size, heterogeneity and lack of current labeling techniques that offer quantitative results.[90, 91] Additionally, for purposes of

tracking the distribution of administered EVs within a biological model, it is difficult to distinguish endogenous EVs from those that are externally applied.

In recent years, various methods have emerged for imaging EVs to study their cellular targeting.[91-94] The most common labeling strategies are the use of lipophilic dyes, radiolabeling, and genetic engineering. However, these labeling techniques have significant disadvantages. The gold standard labeling technique for EVs is the use of lipophilic dyes, such as DiI and PKH67, that anchor to the lipid membrane of EVs.[94, 95] Though these dyes are commercially available and are applied using a relatively straightforward protocol, they can aggregate or leak out of membranes to produce background signal and have a low penetration depth within tissues.[95, 96]

In radioisotope labeling of EVs, a transmembrane protein is labeled with a radioisotope and either loaded into the EV lumen or tagged to their surface and imaged with special cameras.[92, 94] Though this technique allows for imaging within deep tissue and is highly sensitive and specific, handling the radioactive material required for this technique is highly regulated. In addition, special equipment is required to image radiolabeled EVs, which is expensive and necessitates specialized training of personnel to operate. EVs can also be genetically engineered to express recombinant proteins with fluorescent tags.[97, 98] However, genetic engineering can be time consuming, the fluorescent tags can be degraded by proteases within the cells, and there is limited physiological relevance of this technique. It is important to note that all labeling techniques described above are semi-quantitative and mainly provide qualitative visual output of EV localization rather than numerical output. To address these concerns, we

report on the use of oligonucleotide barcodes (oligobarcodes) as a novel technique for labeling EVs.

Oligobarcoding is an advantageous EV labeling technique due to its use of fast and efficient click chemistry to conjugate DNA-based biobarcodes to the surface of EVs. Importantly, oligobarcodes can be readily quantified using standard analytical methods such as polymerase chain reaction (PCR) to amplify the barcode sequence(s) with high sensitivity. We previously used 4-formylbenzoate (4FB) linked to 6-hydrazinonicotinate acetone hydrazone (HyNic) click chemistry to label EVs and virions with fluorescent quantum dots and demonstrated stable, highly tailorable constructs with preservation of EV function.[99] Here, we utilize the same chemistry to conjugate a synthetic 5' amine-containing small oligonucleotide to EVs derived from human semen and from whole rat brain tissue. Our small oligonucleotide barcode is based on the sequence of *C. elegans* microRNA 39 to enable use of commercial stem-loop PCR assays and is modified with phosphothioate bonds to increase stability during culture with cells and tissues.

We demonstrated a proof of concept that this oligobarcoding method can be used to track EV fate from two different EV sources—semen (SEVs) and brain tissue (BEVs)—within two different models: *in vitro* digested vaginal tissue and *ex vivo* brain slices. Semen carries a high concentration of EVs (an average of 1×10^{13} per ejaculate) containing immunosuppressive biomolecules that can act to regulate the female immune system upon delivery favoring a healthy pregnancy. [100-102] It has been shown that SEVs efficiently bind to and enter antigen-presenting cells (APCs), markedly reducing antigen-specific cytokine production.[103] EVs also maintain therapeutic functionality in the brain, as BEVs have been found to improve cell viability, increase

anti-inflammatory cytokine expression, and shift microglia towards a restorative phenotype following *ex vivo* hypoxic ischemic injury.[104, 105] Though this oligobarcode method was tested with EVs from semen and brain tissue, this conjugation technique can be applied to EVs derived from any source and can be used *in vitro*, *ex vivo*, *and in vivo*. The oligobarcoding method establishes a robust, accessible tool for quantifying EV association with specific cell types in cell culture and *in-vivo* conditions, enabling a greater understanding of EV fate and function.

3.3. Materials & Methods

3.3.1. Animal care and ethics

This study was performed in accordance with the guide for the care and use of laboratory animals of the National Institutes of Health (NIH). All animals were handled according to an approved Institutional Animal Care and Use Committee (IACUC) protocol (#4383-02) of the University of Washington (UW), Seattle, WA. The UW has an approved Animal Welfare Assurance (#A3464-01) on file with the NIH Office of Laboratory Animal Welfare, is registered with the United States Department of Agriculture (certificate #91-R-0001), and is accredited by AAALAC International. Time-mated pregnant female Sprague–Dawley rats (virus antibody-free CD® (SD) IGS, Charles River Laboratories, Raleigh, NC, USA) were purchased and arrived on postnatal day 5 with a litter of 10, sex-balanced pups. Dams were housed individually with their litter and allowed to acclimate to their environment. Before and after the experiment, each dam and her pups were housed under standard conditions with an automatic 12h light/dark cycle, a temperature range of 20–26°C, and access to standard chow and autoclaved tap water ad libitum. The pups were checked for health daily.

3.3.2. Isolation of semen-derived extracellular vesicles (SEVs)

SEV were purified from diluted semen by ultracentrifugation at 100,000xg over 25% sucrose cushions for 12h, then washed with PBS and concentrated in 100 kDa spin filters. SEV were characterized by nanoparticle tracking, electron microscopy, and western blotting.

3.3.3. Isolation of brain-derived extracellular vesicles (BEVs)

BEVs were isolated from whole, perfused neonatal rat brains extracted from male postnatal day 10 (P10) rats. Brain tissue was finely chopped in a solution and incubated for 20 minutes in a water bath with protease inhibitors to allow for complete dissociation of extracellular matrix proteins. Subsequently, the homogenate was initially spun at 300xg for 5 minutes, transferred to a new tube to spin at 2000xg for 10 minutes, and finally transferred to new tubes and ultracentrifuged for 10,000xg for 35 minutes. After ultracentrifugation the collected supernatant was run through an Amicon ultrafiltration column (100kDa molecular weight cutoff) and spun at 3214xg for 90-120 minutes, or until the final volume reached 500μL. A size exclusion chromatography column (iZon) was used to further purify BEVs, and fractions containing high concentrations of BEVs were ultracentrifuged in an Amicon ultrafiltration column (50kDa) at 3214xg for 60-100 minutes at 4°C to concentrate isolated BEVs.[104]

3.3.4. Conjugation of oligobarcodes to extracellular vesicles (Oligo-EV)

Working dilutions of HyNic, 4FB, and oligos were prepared in 1X PBS. Concentrated SEV and BEV stocks were added to the HyNic working solution (SEV-HyNic), while oligobarcodes were added to 4FB working solution (oligo-4FB). EV-HyNic and oligo-4FB solutions were incubated in the dark at room temperature on a rotating

stand for 2 hours. After incubation, oligo-4FB was purified with a NAP-5 column (GE Healthcare) to remove excess unconjugated Sulfo-S-4FB. After 2 hours, EV-HyNic was purified using an ultrafiltration unit with a 100kDa molecular weight cut-off (Amicon). The unit was ultracentrifuged at 3214xg to remove excess unconjugated Sulfo-S-HyNic for 30 minutes.

Purified oligo-4FB and EV-HyNic were combined at an 80:1 oligo:EV ratio and diluted to a total volume of 1mL in 1xPBS. This sample was left in the dark on a rotating stand for 2 hours to ensure reaction between oligo-4FB and EV-HyNic. A size exclusion chromatography (SEC) column was used to separate fully conjugated oligo-SEVs from unconjugated oligo-4FB and fractions 7-9 (2.5mL total) were collected. A control sample containing unconjugated oligo-4FB (oligo alone) with 1XPBS was also purified at the same time to ensure that the conjugation procedure did not introduce any artifacts. A final oligo-SEV concentration was performed using an Amicon 50kDa molecular weight cut-off ultrafiltration unit, with centrifugation at 3215xg for 45 minutes.

3.3.5. In vitro oligo-SEV exposure experiments to vaginal cells and tissues

Human vaginal tissues were trimmed to remove excess stroma, then cut into small (~30-50 mm squares) using sterile razor blades. Pieces were dissociated in freshly made collagenase (700 collagen units/mL) digestion media containing DNase (50Units/μL) in a 37°C orbital incubator at 200rpm for 45 minutes. Tissue homogenate was passed through a 70μm cell strainer to remove undigested chunks and large terminally differentiated epithelial cells, and flow through cells enriched for leukocytes were collected in a 50mL conical tube. The isolated cells were the centrifuged at 300xg for 12 minutes at 4°C. After centrifugation, the supernatant was removed and replaced

with fresh R10 media to resuspend the cell pellet. This process was repeated multiple times until all biopsy fractions were dissociated and strained. Following the last centrifugation step, isolated cells were put in R10 media and plated at a desired cell concentration in a flask or 6 well cell culture plate.

Oligo-SEVs were then administered directly to isolated cells and incubated at 37°C for 6 and 24h Following exposure, APCs were separated with magnetic bead isolation (EasySep Cell Separation) against CD11c, and both CD11c+ cells and non-APC remaining cell fractions (flow through) were collected to be analyzed.

3.3.6. Preparation of ex vivo organotypic whole hemisphere brain slices

Following intraperitoneal euthanasia with pentobarbitol, fresh brain tissue was rapidly extracted from P10 male rats, placed in ice cold dissection media, and sectioned into 300 μm thick slices using a McIlwain tissue chopper (Ted Pella). These slices were plated onto 30 mm cell culture inserts (CellTreat) and incubated at 37°C in 1mL of 25% slice culture medium (SCM) and 5% CO_2 to recover from acute slicing. After 24h, oligo-BEVs were topically applied to the brain slices (10^9 molecules of oligo-BEVs per slice), which were then returned to 25% SCM for another 24h before processing.

Brain slices were collected and digested in a Hibernate-E buffer containing collagenase and protease and phosphotase inhibitors. Following digestion, samples were spun down at 450g for 10 minutes to pellet cells prior to Direct PCR and stemloop conversion.

3.3.7. Stemloop conversion reaction

Cell pellets were lysed in DNAse free H_2O and immediately heated at 95°C for 5 minutes. Stemloop conversion samples contained 0.2μL DNA polymerase (Amplitaq), 3μL 4X stemloop primer, 1.5μL 10X PCR Buffer I mix, 0.5μL 10mM dNTPs, 1μL DNAse

free H_2O, and 9µL of each sample. Samples were run with the following thermocycler settings: 1) 95°C for 5 minutes, 2) 16°C for 30 minutes, 3) 65°C for 5 minutes, 4) 72°C for 5 minutes, 5) 95°C for 2 minutes, 6) 16°C for 5 minutes, 7) 65°C for 5 minutes, and 8) 72°C for 5 minutes.

3.3.8. Direct PCR for oligo amplification

Following stemloop extension, samples oligos and gDNA targets were pre-amplified using a preamplification reagent (Thermofisher Taqman PreAmp Master Mix). 20X oligobarcode primer-probe mix (FAM) and late RPP30 genomic control (HEX/Cy5) were diluted in TE buffer to a final concentration of 0.2X. 1.25µL of first-step PCR product was combined with 6.25µL preamp master mix, 1.875µL of each diluted primer-probe mix, and 1.25µL of DNAse free H_2O. Thermocycler conditions used were: 1) 95°C for 10 minutes, 2) 55°C for 2 minutes, 3) 72°C for 2 minutes, 4) 12 cycles of 95°C for 15 seconds and 60°C for 4 minutes, and 5) 99.9°C for 10 minutes.

3.3.9. qPCR for oligo-EV target quantification

The pre-amplification products were diluted 1:10 in TE buffer to be run with qPCR. For a 20µL total reaction volume per well, 10µL of Taqman Proamp Master Mix was combined with 1µL of each 20X primer-probe mix, 8µL DNAse free H_2O and 1µL of diluted pre-amplification sample. Thermocycler conditions used were: 1) denaturing at 95°C for 20 seconds, followed by 2) annealing/extension for 45 cycles of 95°C for 1 second and 65°C for 25 seconds. Samples were run with a multi-channel setting to collect fluorescent signals concurrently from the oligobarcode (FAM) and genomic DNA (HEX) probes. Captured oligobarcode fluorescence signals were normalized by genomic DNA signals prior to calculating fold changes between conditions.

3.3.10. Cell viability experiments with alamarBlue Assay

The viability and proliferation of THP cells following oligo-SEV exposure was quantified using an alamarBlue cell viability assay (Thermofisher). This assay uses a reagent that produces a highly fluorescent compound following its reduction by living cells. This fluorescence can be quantified to measure cell viability and proliferation, with positive absorbance unit values corresponding to positive cell viability and proliferation. 15,000 THP cells were exposed to various dilutions of oligo-SEV in a 96-well tissue treated plate. Cells were suspended with R10 media to a final volume of 100µL and 10µL of alamarBlue reagent was added to the cell suspension. Cells were incubated with the alamarBlue reagent at 37°C for 6 and 24h. At the 6h timepoint, a plate reader was used to measure absorbance at 570nm wavelength prior to media change. Fresh R10 media was added at 100µL per well and 10µL of alamarBlue reagent was added and incubated with cells until the 24h timepoint. A maximum cell death sample and a media only sample were used as controls.

3.3.11. In vivo murine application of oligobarcode-SEVs

Female C57BL/6J mice were used for intravaginal application of oligo-SEVs. All mice were 12-16 weeks old, and injected with Depo-Provera 7 days prior to oligo-SEV application. For every litter of 12 mice, 6 mice were administered oligo-SEVs, 3 mice were administered with blank unconjugated oligobarcodes, and 3 were used as saline controls. Prior to administration of oligo-SEVs, mice vaginal canals are swabbed to open up the cavity and remove mucus. One dose of oligo-SEVs (1.3 - 3.3 x 10^{10} molecules of oligo-SEV) in a 20 µL volume were administered per mouse. Vaginal administration of oligo-SEVs, blank oligobarcode, and saline was performed 24h

following Depo-Provera injection, and the mice were left for an additional 24h following the procedure for oligo-SEV uptake. Following the 24h oligo-SEV incubation period, the mice were sacrificed and the upper and lower genital tracts as well as the iliac, mesenteric, and inguinal lymph nodes were extracted. For every condition (oligo-SEV, blank oligo, saline control) organs from 3 mice were pooled together to improve oligobarcode detection. These harvested tissues were immediately digested, immunoseparated into APC and flow through cell populations, and Direct PCR was performed for each sample.

3.3.12. Institutional review board statement

This study was performed in accordance with the guide for the care and use of laboratory animals of the National Institutes of Health (NIH). All animals were handled according to an approved Institutional Animal Care and Use Committee (IACUC) protocols (#4383-02) of the University of Washington (UW), Seattle, WA. The UW has an approved Animal Welfare Assurance (#A3464-01) on file with the NIH Office of Laboratory Animal Welfare, is registered with the United States Department of Agriculture (certificate #91-R-0001), and is accredited by AAALAC International.

3.4. Results

3.4.1. Design of Oligonucleotide barcode and PCR amplification methodology

Oligobarcodes used for conjugation studies must be short enough for cellular uptake but also stable enough for Direct PCR amplification. Oligobarcoding of EVs occurred in a stepwise procedure: 1) EVs and oligobarcodes are separately functionalized to linker molecules, followed by 2) immediate incubation of newly functionalized EVs and oligobarcodes. We designed oligobarcodes with 5’ amine

groups to enable conjugation to sulfo-S-4FB linker molecules. Simultaneously, EVs were conjugated to sulfo-S-HyNic linker molecules as previously described, before covalent conjugation of both EVs and oligonucleotides using click chemistry. [106]

We initially tested a barcode design that was 100-nucleotides long for use in quantitative PCR (qPCR) reactions, but found that long oligobarcodes resulted in high levels of background following qPCR amplification in our control samples, suggesting primer dimerization or nonspecific binding of the primer probes. Based on these results, we tested a shorter 22-nucleotide barcode based on the sequence of *C. elegans* microRNA cel-miR-39, of which commercial reagents using a stem-loop primer and PCR primer-probe sets are available. Our short cel-miR-39 mimic barcode was further modified with phosphorthioate bonds to increase resistance to exonucleases (Figure 3.9 A). For detection of the microRNA, a stem-loop conversion reaction is required using a stem-loop primer, which is analogous to reverse-transcription.[107, 108] This stem-loop extended our short oligobarcodes with extra nucleotides to allow for the docking of primers to the target sequence for qPCR detection (Figure 3.9B). Finally for qPCR, we used commercial cel-miR-39 primer-probe sets (Taqman miRNA assay) which consist of two primers and a fluorescent fluorescein-based (FAM) probe to detect the target oligobarcode. We performed serial dilution experiments comparing expression level of oligobarcode detected with different amounts of stem-loop primer used in the reaction compared to a condition wherein no stem-loop primer is used at two different annealing temperatures. As expected, we found that using the stem-loop primer enabled oligobarcode detection by up to 10^4-fold greater than PBS controls and was robust across both dilutions of input stem-loop primer (Appendix B.1).

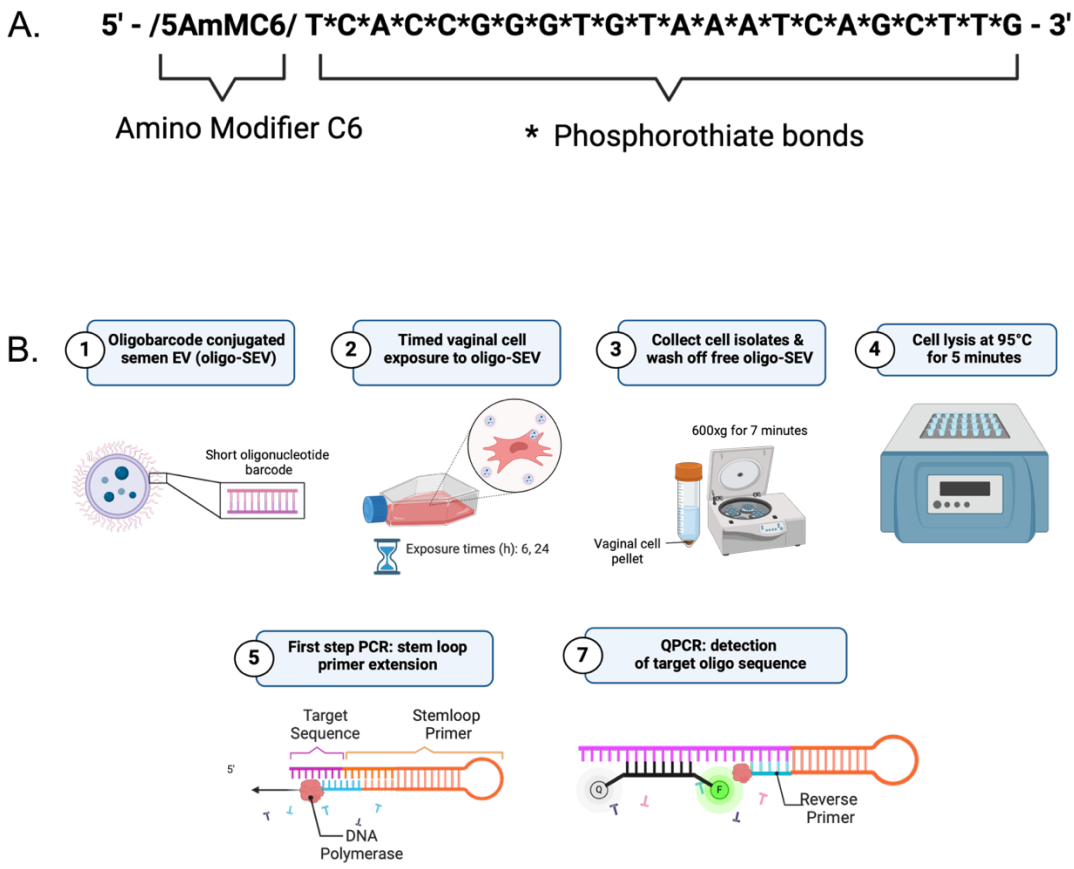

Figure 3.9. Oligobarcode design and application.
A) Oligobarcode design with amino and phosphorothiate bond modifications to improve the stability against exonucleases in physiological conditions. (B) Schema of experimental design for oligobarcode exposure studies and PCR strategy, created in BioRender.

We prepared oligo-EV conjugations using SEV and BEV, characterized oligo-EV conjugates using nanoparticle tracking analysis, then did stem-loop conversion and qPCR to detect the oligobarcode sequence on a dilution series of oligo-EV inputs. As little as 10 and as high as 10^7 molecules of oligo-SEVs and oligo-BEVs were detected, demonstrating that this method can quantify the amount of barcode on a wide range of oligo-EV inputs (Figure 3.10 A). We also ran digital PCR for absolute oligobarcode detection in oligo-SEV dilutions (Figure 3.10 B), which allowed us to estimate the ratio

of oligobarcode to EV and a detection limit for input number of oligo-EVs. We detected around 2 copies of oligobarcode per EV as quantified by digital PCR.

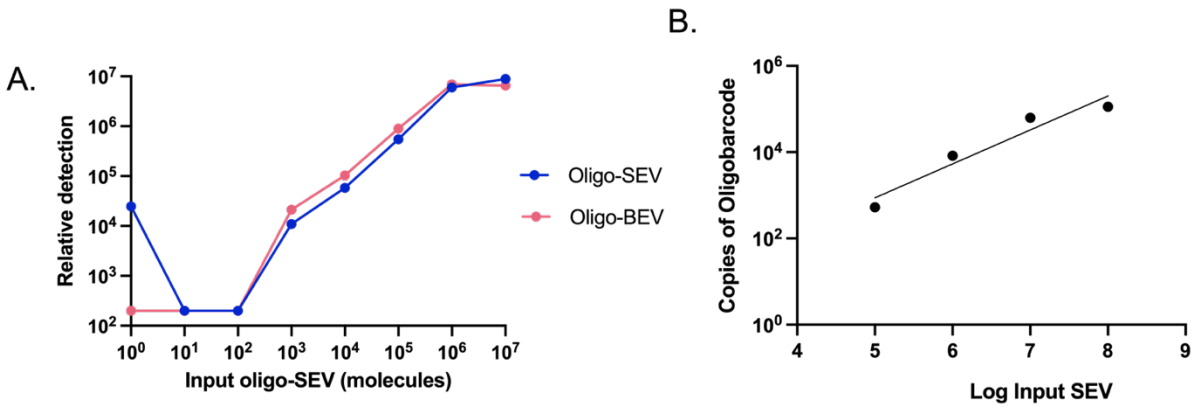

Figure 3.10. Oligobarcoded EV limit of detection evaluations. Comparison of dilution series of oligobarcoded SEVs (oligo-SEVs) and BEVs (oligo-BEVs) to determine the limit of detection for qPCR. B) Direct digital PCR results quantifying copies of oligobarcode detected per input number of SEV. Oligo-SEVs tested were from the same batch and any value below log3 of input SEV was undetected by digital PCR. Results are averaged from two technical replicates.

3.4.2. Application of oligobarcode-SEV in in vivo cell culture and ex vivo vaginal tissue culture

A serial dilution series was tested for oligo-SEV and oligo-BEV samples without cells to determine the proof-of-concept limit of detection using qPCR. Though commercial DNA columns are typically used to isolate DNA from samples, there may be significant DNA oligobarcode loss that can occur due to the short length of our oligobarcodes (22 base pairs) combined with several column extraction steps required for the assay. To address this challenge, a Direct PCR approach was implemented to detect oligobarcodes in a one-step process, bypassing DNA columns. We first tested this approach without the use of cells (Figure 3.11 A).[109] Rather than relying on DNA columns, Direct PCR used heat lysis to release the oligobarcodes into solution, which

was then directly inputted into PCR for stem-loop extension. In this way, lengthy DNA extraction using separate columns was not required, but instead DNA can be directly extruded from EVs and cells in one heat lysis step. The signal of oligo-SEV detected in our samples had up to a 10,000-fold increase when we used Direct PCR compared to DNA extraction columns to detect oligobarcode (Figure 3.11 A).Oligo-SEV and oligo-BEV trends were similar, suggesting uniform oligobarcode conjugation between both EV types and translatability of this technique.

Oligo-SEV conjugates were then applied to THP cells *in vitro* to test the detection limit and feasibility of oligobarcode detection in physiological environments. When applied to THP cell culture, we found that oligobarcodes were detected in treated cells in a dose-dependent manner, notably for dosages greater than 100 molecules of oligo-SEV (Figure 3.11 B). Additionally, to investigate the relationship between cell number and detection of oligobarcode, seral dilutions of THP cells were exposed to a spike-in of 10^7 molecules of oligo-SEVs for 24h (Figure 3.11 C).

From this experiment, oligobarcodes were detected in samples with as little as 1000 THP cells and in samples with up to 50,000 cells. There is a consistent inverse trend of decreased oligobarcode detection with increasing initial cell seeding density for the study. We detected no oligobarcode signal in samples containing 100,000 and 250,000 cells.

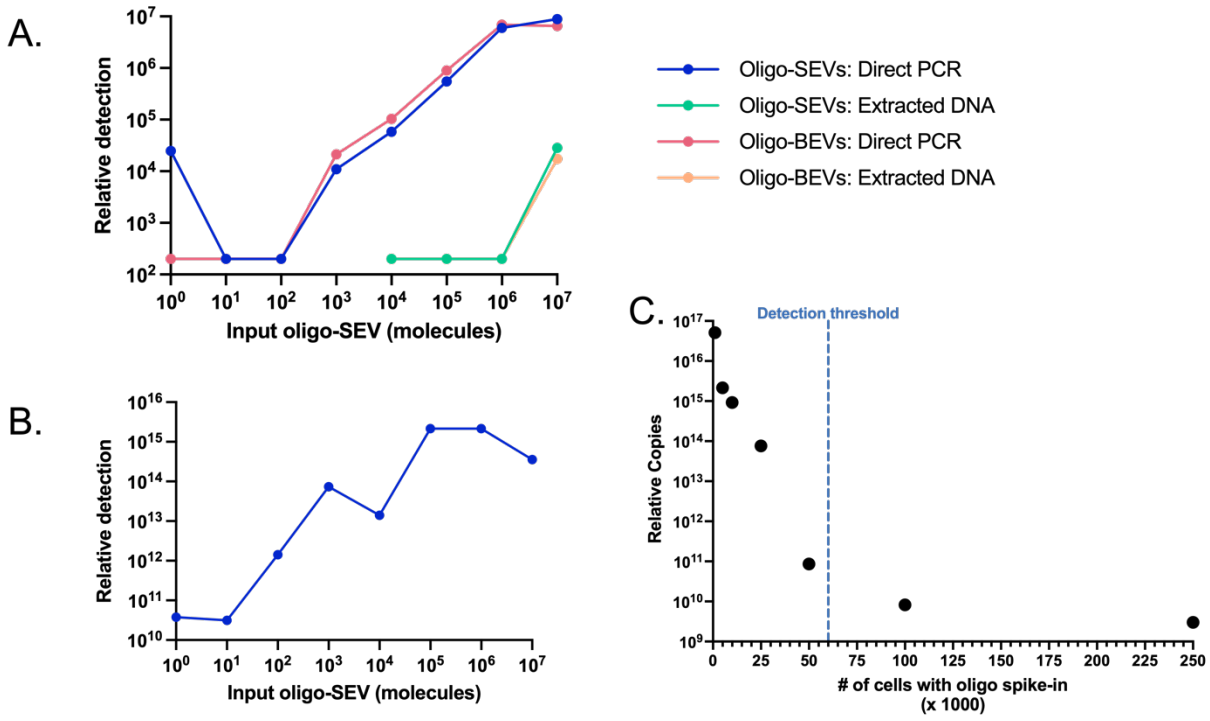

Figure 3.11. Determining the detection limit of oligo-EVs.
A) Comparison of the detection levels of oligobarcode using different DNA extraction techniques. Dilutions of oligo-SEV and oligo-BEVs were exposed to either commercial Qiagen DNA extraction columns ('Extracted DNA') or Direct PCR using heat lysis without extraction columns. To apply this technique in vitro, the qPCR detection limits of oligobarcode were compared when B) different dilutions of oligo-SEV spike-in were exposed to 25,000 human THP cells and when C) different dilutions of THP cells were exposed to 10^7 molecules of oligo-SEVs. Cells were incubated with oligo-SEVs for 24h before processing.

Following successful oligo-SEV detection in *in vitro* THP cells, oligo-SEVs were then administered to digested *ex vivo* human vaginal tissue. Oligo-SEVs and unconjugated oligobarcodes (blank oligo) were applied to digested vaginal tissue cultures at 10^6 molecules of oligo-SEV per cell for 6 and 24 hours. At each timepoint, cells were collected and washed to remove free oligo-SEVs. We then used magnetic cell separation based on positive selection of CD11c+ expressing cells to isolate the APCs from the remaining cells in the bulk sample (flow through). Oligobarcode uptake was measured and compared between the APCs and flow through cell populations using Direct and pre-amplified qPCR. Oligobarcode was detected in all samples

exposed to oligo-SEVs for both 6 and 24h timepoints. At these timepoints, oligo-SEV signal was detected in vaginal tissue up to 30,000-fold greater than unconjugated oligobarcodes, suggesting that SEVs enhance the oligobarcode uptake within cells (Figure 3.12 A). We also found that at both 6 and 24h timepoints oligo-SEVs were significantly localized with APCs compared to other cell types (flow through) by up to 100-fold, supporting their role as a first-responder to foreign entities within the body (Figure 3.12 A).[110-112] This result is similar to previous data which used fluorescence-based tracking of SEV uptake to demonstrate that antigen-presenting cells (APCs) preferentially uptake SEV.[113] This result served as a proof of concept that our oligobarcodes can be detected when exposed to physiological conditions for up to 24h post-EV exposure.

One limitation of using a stem-loop primer-based assay in more complex systems with cells is that the stem-loop can cause background amplification in samples when the initial stem-loop primer is not diluted enough in the subsequent PCR. However, dilution of the initial stem-loop product also reduced detection of oligobarcode in samples with low oligobarcode inputs and cellular DNA background. To reduce the background and improve the sensitivity for signal detection of oligobarcodes *in vitro*, a Taqman preamplification assay (Thermofisher) was used prior to qPCR. Taqmman preamplification (preamp) is 13-cycle PCR step that increased the amount of amplified target oligobarcode in the sample sufficiently above background noise. E*x vivo* digested vaginal cells were treated with oligo-SEV for 6h, then processed with Direct PCR followed by the preamp step and qPCR. Results indicated that priming samples with

preamp increased oligo-SEV detection by 10^3-10^4-fold compared to control samples without preamp (Figure 3.12 B).

To address potential concerns that the addition of engineered oligobarcodes with increased phosphorothioate bonds may cause toxicity to cells when exposed over long periods of time, we performed cell viability assays with *ex vivo* vaginal cells exposed to oligo-SEV. Our cell viability assays showed no cytotoxicity following 6h and 24h of exposure to oligo-SEV, and cells remained viable and proliferative for up to 24h of exposure to oligo-SEVs (Figure 3.12 C). Interestingly, cells demonstrated increased metabolic activity after 24h compared to 6h, suggesting proliferation even after oligo-SEV application.

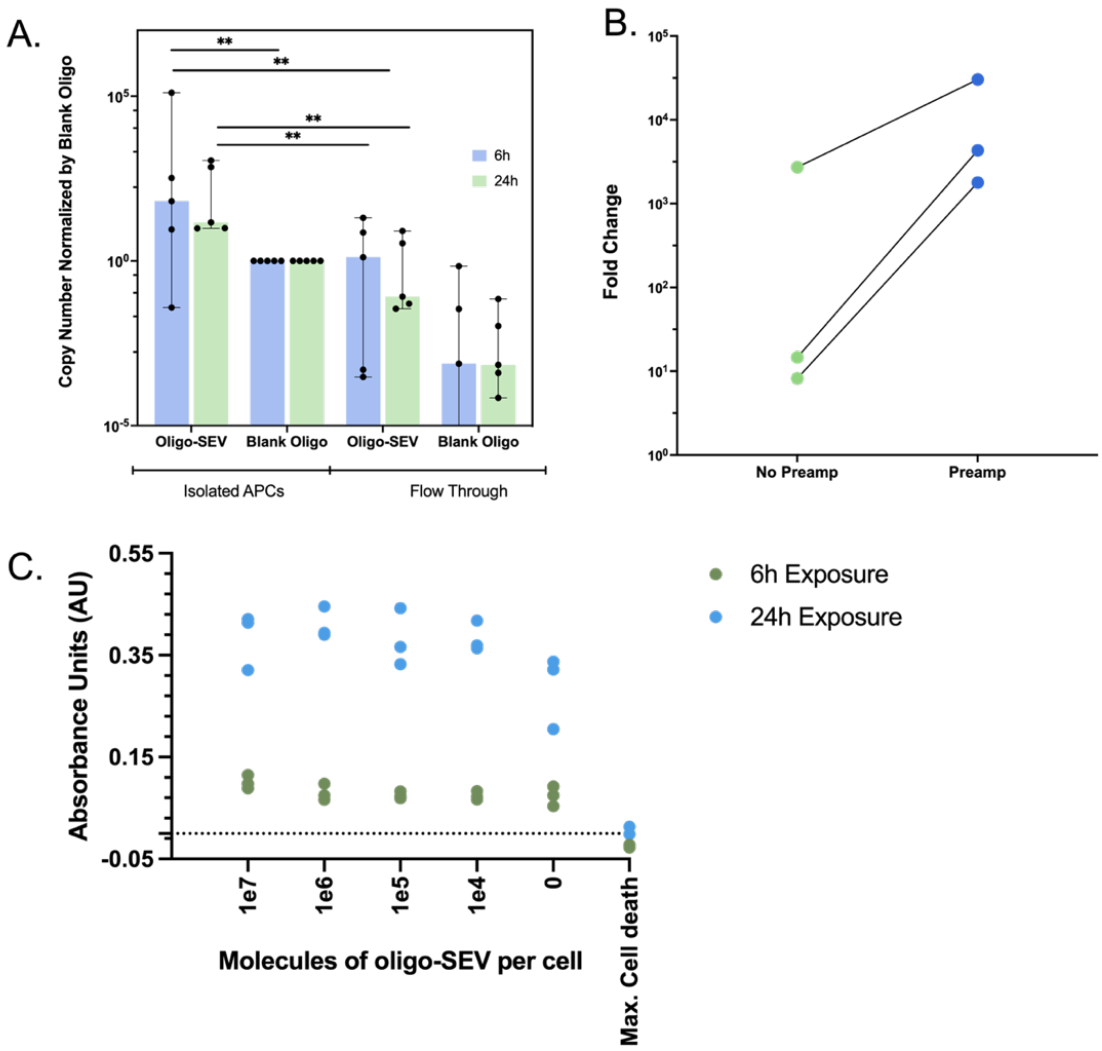

Figure 3.12. Oligo-SEV exposure to ex vivo vaginal tissue.
A) Ex vivo human vaginal cells from digested tissue were exposed to oligo-SEVs and unconjugated oligo for 6 & 24h. At the completion of the exposure period, antigen presenting cells (APCs) were isolated from non-APCs (flow through) using magnetic beads. Oligo expression (FAM) was measured with qPCR and normalized against a housekeeper gene (Late RPP30--HEX). All conditions were normalized against the level of blank oligo expression detected in APCs (negative control). N=5, bars plot median with standard deviation. B) Comparing efficacy of using preamp solution vs. without using preamp solution following 6h of oligo-SEV exposure to ex vivo vaginal tissue. Fold changes in oligo-SEV amplification compared to non-treated (cell only) control. N=3 biological replicates. C) Evaluating cell viability of vaginal cells exposed to oligo-SEVs over 6 and 24h using AlamarBlue metabolic assay.

3.4.3. Application of oligobarcode-BEVs in ex vivo organotypic whole hemisphere brain slices

One key aspect of this innovative oligobarcoding technique using fast and efficient click chemistry conjugation is that it can be applied using EVs derived from any source. In addition to SEVs, oligobarcodes were conjugated to brain-tissue derived EVs (BEVs) and topically applied onto organotypic whole hemisphere brain slices. Leveraging a previously established isolation technique,[104] BEVs were derived from male whole neonatal rat brain tissue for this study. Different dilutions of oligobarcoded BEVs (oligo-BEVs) and blank oligo were topically applied to brain slices to demonstrate detection of oligobarcode in *ex vivo* brain tissue culture. Following 24h exposure of brain slices to oligo-BEVs, the brain tissue was collected, digested, and oligobarcode signals were detected using Direct and qPCR analyses. Oligobarcode signal was detected in brain slices exposed to oligo-BEVs in a dose-dependent manner, with noticeably more amplification detected after 10^8 molecules of EV administered to the sample (Figure 3.13 A). Oligobarcode signal was successfully detected in tissue slices at 2^{15}-2^{17} fold greater than blank oligobarcodes when normalized by the housekeeper gene GAPDH (Glyceraldehyde 3-phosphate dehydrogenase) (Figure 3.13 B).[114 115] This suggested that oligo-BEVs are being actively taken up by brain cells and are detectable following 24h in tissue culture at physiological conditions. Furthermore, blank oligos were not detected in any sample regardless of the dilution factor used. These results demonstrate that oligobarcodes can be successfully conjugated to EVs from different sources and can be detected in cells both *in vitro* and *ex vivo*.

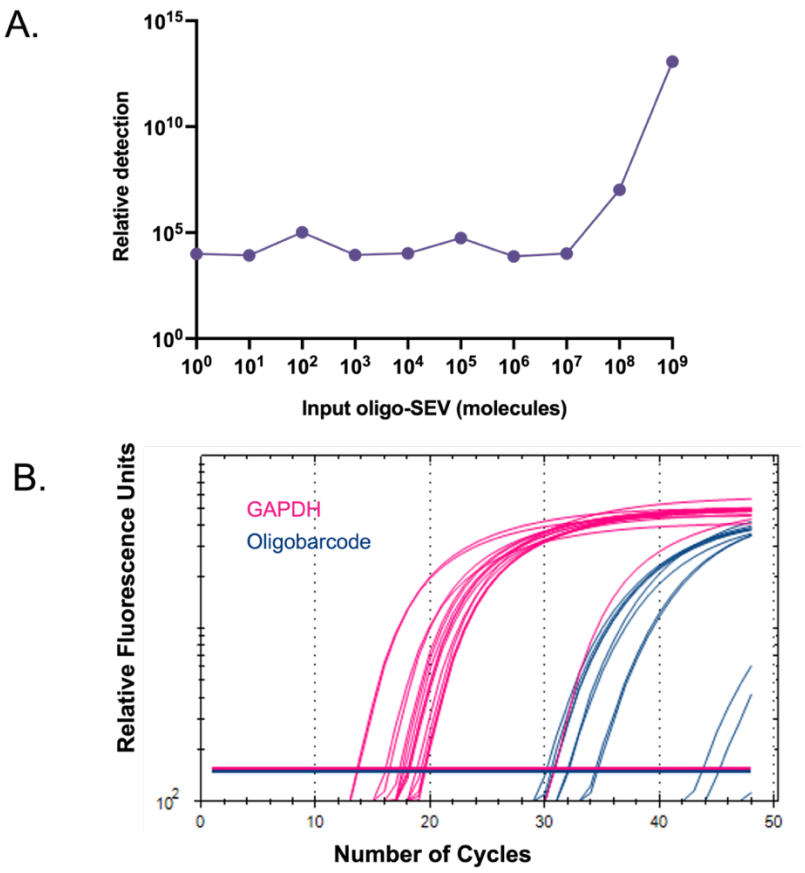

Figure 3.13. Oligo-BEV exposure to ex vivo brain tissue.
A) Dilution series of oligobarcode-BEV exposure to ex vivo organotypic whole hemisphere brain slices for 24h. Oligobarcode signal was measured with fluorescent probe-based qPCR and normalized against a housekeeper gene (GAPDH). B) Representative probe-based qPCR amplification results comparing oligobarcode-BEV signal (blue) to blank unconjugated oligobarcode signal (pink) in one sample. Samples with oligobarcoded BEVs demonstrated about $2^{15} - 2^{17}$ fold more signal (threshold cycle ~30-35) compared to blank oligobarcodes (threshold cycle ~47) when administered to brain slices. N=9 biological replicates, with each data point representing an average of 3 technical replicates.

3.4.5. In vivo administration and qPCR detection of oligobarcode-SEVs in murine models

Following the successful detection of oligobarcodes within both *in vitro* and *ex vivo* cultures, oligo-SEVs were applied to *in vivo* murine models. To test for the translatability of the oligobarcode technique for *in vivo* studies, one dose of oligo-SEVs were administered to female C57BL/6J mice. Genital tract and lymph node tissues were

harvested 24h after administration and immediately processed for analysis of oligobarcode signal in tissues with administered oligo-SEVs, blank unconjugated oligobarcodes, and saline controls (Figure 3.14). The tissues were digested, sorted, and Direct PCR and a probe-based qPCR were run on APCs and flow through cells as described for the *in vitro* studies. Overall, oligo-SEV detection levels were higher among APCs (Figure 3.14 A,C) compared to non-APC flow through cells (Figure 3.14 B,D) across all samples tested, indicating that oligo-SEVs may preferentially localize to APC cells. In the lower genital tract APCs expressed 133% greater oligo-SEV signal compared to flow through cells, and in the upper genital tract no oligo-SEVs were detected in the flow through at all. Blank oligobarcode was undetectable in almost every collected sample besides one APC sample from the lower genital tract, demonstrating that the SEVs are responsible for oligo-SEV uptake in cells compared to unconjugated oligobarcode (Figure 3.14 C-D).

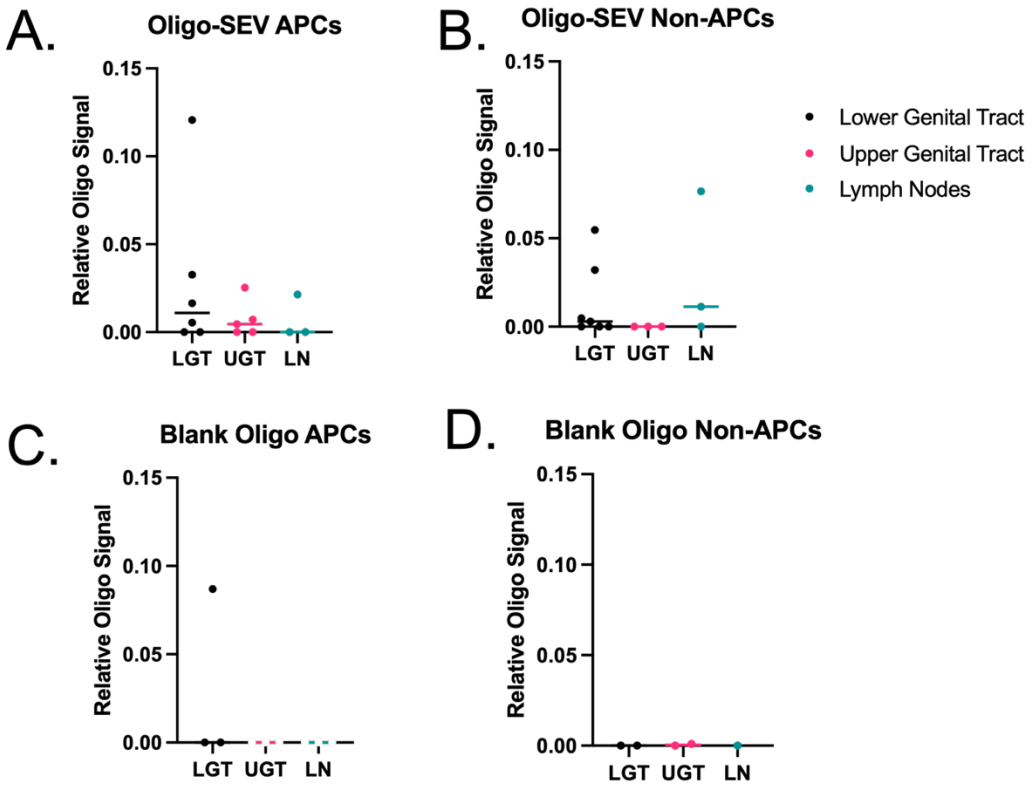

Figure 3.14. In vivo murine administration of oligo-SEVs and blank oligo for 24h. Oligo-SEVs and blank oligo were vaginally administered. Oligo-BEV and blank oligobarcode expression were quantified in A,C) APCs and B,D) non-APC cells. Oligobarcode signal was normalized against the housekeeping gene RPP30 expression, and then compared against a blank PBS control. N=4-6 biological replicates for oligo-SEV and 2 biological replicates for blank oligo. Oligobarcode detection levels were compared to a blank saline control.

Of all APC fractions, those derived from the lower genital tract demonstrated the greatest oligobarcode expression change compared to a saline control followed by the upper genital tract and lymph nodes. In contrast, in the non-APC flow through cell fractions cells derived from the lymph nodes demonstrated greatest oligobarcode expression levels, though there is high variability in the samples analyzed for the lymph nodes.

3.5. Discussion

Existing labeling methods for EVs are non-specific, semi-quantitative, and often require expensive equipment and training which reduces our ability to quantify EV localization within the body. Our novel oligobarcoding technique addresses challenges posed by current labeling methods by providing a highly translatable, accessible, and quantitative method that can be used to label EVs from any source and can be used *in vitro, ex vivo, and in vivo.* Detection of oligobarcodes require accessible PCR instrumentation, which provides quantitative information about the degree of oligobarcode uptake within cells. We have shown that this oligobarcoding method is detectable across multiple biological models (*in vitro, ex vivo, in* vivo) using our developed a multi-step PCR protocol, with a lower detection limit of 10 molecules of oligo-SEVs and a higher limit of 10^7 molecules of oligo-SEVs. In addition to testing oligo-SEVs, oligo-BEVs were also successfully detected using this proposed methodology. The oligo-EVs were detected in both vaginal and brain tissues using standard PCR techniques, which allow for greater translatability of this technology across different research spaces. Though the studies presented in this dissertation pertain to only one oligobarcode design, we are currently working with a different biobarcode design to demonstrate the flexibility of our oligobarcoding technology to be compatible with various barcode designs. Ideally, unique oligobarcode designs can be conjugated to EVs and detected in a single sample to uniquely identify different EVs.

The oligobarcoding method we developed is stable in physiological conditions up to 24h in different tissues. Oligobarcoding also did not induce cell cytotoxicity over this period of time, but rather, cells experienced increased metabolic activity likely due to

proliferation between 6-24h of oligo-SEV exposure. When applied *in vitro*, the upper limit of cells collected wherein oligo-SEVs signal remained detectable was 50,000. There was a noticeable decrease in oligo-SEV expression and number of cells seeded with the oligo-SEVs. Beyond the upper limit of 50,000 cells, Direct PCR may not work as well due to PCR inhibitors present in heat lysed cell samples. These PCR inhibitors increased as the number of initial cells seeded increased, resulting in decreased oligo-SEV signal expression. Oligo-SEVs were detected *in vitro* following 24h of exposure to THP cells at various dilutions ranging from 1-10^7 molecules of oligo-SEV in a generally dose-dependent manner. However, a slight decrease in oligo-SEV expression was observed after a dose of 10^7 oligo-SEV molecules. This suggests that 10^7 molecules of oligo-SEVs may be the upper limit of detection when applied to 10,000 THP cells. This dose of oligo-SEVs may be too high, given the recommended low cell count used for these *in vitro* studies. At this low cell seeding density, the cells may experience an upper limit of oligo-SEV uptake, resulting in a reduction of oligobarcode signal amplification between 10^6 and 10^7 oligo-SEVs.

Successful oligobarcode detection *in vitro* prompted further studies in more complex *ex vivo* physiological environments. To demonstrate the translatability of this technology, oligo-SEVs were applied to *ex vivo* human vaginal culture and oligo-BEVs were applied to *ex vivo* rat brain slices. When exposed to *ex vivo* vaginal tissues, oligo-SEV signals had significantly greater detection levels compared to blank unconjugated oligobarcodes, suggesting that SEVs are involved in driving specific cellular uptake and without the SEVs blank oligobarcodes are not effectively trafficked by vaginal cells.

Similarly, oligo-BEVs were also successfully detected following 24h of exposure to *ex vivo* brain slices, whereas there was no signal from blank oligo.

To evaluate oligo-SEV uptake within specific cell populations, oligo-SEVs were applied to *ex vivo* vaginal cells for 24h and APCS were immunoseparated from other cell populations (flow through). Oligo-SEVs are preferentially taken up by APCs in *ex vivo* vaginal cell culture compared to blank oligo, especially after 6h. Furthermore, APCs demonstrated greater uptake of oligo-SEVs compared to flow through cells at both 6 and 24h timepoints. This suggests that not only are oligo-SEVs detectable after 24h but they are also preferentially taken up by APCs compared to the flow through cells in vaginal tissue. As APCs are responsible for initiating immune response mechanisms against foreign microbes and pathogens, our results confirm that APCs uptake oligo-SEVs, which may be one proposed route of the conferral of tolerogenic factors from the SEV to APCs.[110, 112]

Following the successful detection of oligobarcodes in two different *ex vivo* tissue models, oligo-SEVs were applied to *in vivo* murine models and cells were analyzed for the presence of oligobarcode signal. Oligo-SEV levels were detected in both APC and flow through cell populations, while blank unconjugated oligobarcodes were only detectable in one APC sample in the lower genital tract. These results suggest that APCs preferentially uptake oligo-SEVs compared to blank oligo across all organs analyzed. Furthermore, oligo-SEV signal was detected in APCs across all regions (lower genital tract, upper genital tract, lymph nodes) while the signal was unreliable in other flow through cell types. Specifically, the lower genital tract revealed the highest levels of oligo-SEV signal, followed by the lymph nodes and upper genital tract. This

trend is not observed when evaluating oligo-SEV expression in non-APC flow through cells. As oligo-SEV intravaginal application occurred in the vagina, it is likely that oligo-SEVs that were not completely trafficked to other organs after 24h remained in the lower vaginal tract and interacted non-specifically to the cells in that region. From these results it is hypothesized that following 24h of exposure to the vaginal canal, oligo-SEVs are trafficked upwards from the lower genital tract towards the lymph nodes and upper genital tract by APCs. In comparison, flow through cells exhibited the greatest level of oligo-SEV expression in the lower genital tract, but inconsistent levels of oligo-SEV expression in the lymph nodes and upper genital tract. This suggests that the population of oligo-SEVs that remained in the lower genital tract did not get trafficked to other organs by non-APC flow through cells. Together, these results demonstrate that APCs may favor SEVs to uptake compared to other non-APC cells. It is important to note that unusually high levels of background signal were detected across all organs collected in saline controls. This level of background in qPCR was not observed in the *in* vitro or *ex vivo* human samples, nor the *ex vivo* rat samples. We hypothesize that the PCR background is a result of non-specific binding of the oligobarcode probe to a mouse-specific molecular target. Future studies using either optimized oligobarcode primer-probe sequences that are species-specific will reduce non-specific oligobarcode signals in the model organism. Alternatively, another form of EV detection and quantification such as using a molecular beacon rather than PCR can also improve sensitivity and reduce background noise.[116] We are currently working on a complementary detection methodology utilizing molecular beacons that fluoresce upon hybridization to the biobarcode targets. Molecular beacons are specific to the target sequence can be easily

detected using with a UV plate reader. Our preliminary results indicated that molecular beacons were detected within *in vitro* THP cell somas and were able to specifically bind to our target biobarcodes.

3.6. Conclusion

The ability to track EV uptake within cells is crucial to advancing the EV research and therapeutics spaces. We developed and deployed a novel oligonucleotide barcode tagging methodology for EVs using click chemistry. To demonstrate the translatability of this technology across fields, oligobarcodes were conjugated to EVs from brain tissue and semen and has been tested *in vitro*, *ex vivo*, and *in vivo*. Our results collectively show the translatability of our oligobarcoding technique to be detected from EVs across species and quantified with PCR to determine EV uptake within different cellular populations. Oligobarcodes address several concerns from existing EV labeling techniques by providing an accessible, low cost, sensitive, and quantitative detection methodology that can be readily applied to EVs from any source.

CHAPTER 4. DUAL QUANTUM DOT AND OLIGOBARCODE LABELING TO TRACK EV BEHAVIOR AND CELLULAR FATE

Nam Phuong Nguyen, Nels Schimek, Eleanor Wu, Olivia Colwell, Lucia Vojtech, Elizabeth Nance

This chapter is in preparation for submission under the title “Dual Quantum Dot and Oligobarcode Labeling to Probe Tissue Uptake and Transport of Brain Tissue-Derived Extracellular Vesicles."

4.1. Abstract

Extracellular vesicles (EVs) have emerged as promising therapeutic agents in various neurological conditions due to their ability to modulate injury response, tissue repair, and inflammation. However, there is a lack of detailed knowledge of EV movement within tissue, EV localization, and fate, which can limit the translation of EV-based therapeutics or diagnostics. To qualitatively and quantitatively assess EV behavior, we employed a novel click chemistry approach to label and track brain tissue-derived EVs (BEVs) with quantum dots (QDs) and oligobarcodes in brain tissue. Studies performed using EVs isolated from tissue rather than cell culture are more representative of the physiological behavior of endogenous EVs, especially within complex tissue environments. We used a combination of confocal microscopy, multiple particle tracking, and quantitative PCR to track BEVs on short- and long- timescales. Our findings confirmed that BEVs associate with microglia in an *ex vivo* brain tissue model, with increased cellular association observed following oxygen-glucose deprivation (OGD) injury, particularly in the striatum. Trends in BEV effective diffusion coefficients suggested regional changes in extracellular matrix integrity and cellular

viability post-injury. Additionally, novel oligobarcode tagging allowed us to quantify the uptake of BEVs in brain tissue up to 48h post-application and identify significant BEV uptake by microglia. Our results demonstrate the importance of considering the regional and pathological states of tissue in evaluating BEV localization and transport. Further mechanistic studies on pathways governing BEV cellular uptake in the brain is necessary for advancing EV-based therapeutics for neurological disorders.

4.2. Introduction

Extracellular vesicles (EVs) are biological nanoparticles that have garnered much interest in the therapeutic space due to their emergence as important players in injury response, tissue repair and regeneration, and mitigating inflammation in the body.[85, 117, 118] There are currently multiple registered clinical trials involving the use of EVs to address a variety of neurological conditions including ischemic stroke, Huntington's Disease, Parkinson's Disease, and dementia.[64] In particular, research focused on traumatic brain injury and brain disease has increasingly supported the critical role that EVs play in in the regulation of glial and neuronal communication, neuronal development, inflammatory cascades, tissue repair, and cellular proliferation within the adult brain.[25, 105, 119, 120] In a healthy brain model, EVs support critical crosstalk between neurons and glial cells. However, in injury or disease conditions, EVs can contribute to the spreading of inflammatory, antigenic, and cell death signals throughout the body.

Tissue repair in the brain following trauma relies on effective and robust exchanges of information between complex and diverse networks of brain cells via brain tissue-derived EVs (BEVs).[25, 31-33] Both *in vitro* and *in vivo* studies confirmed that treatment with cell culture-derived EVs led to increased neuronal recovery in adult

stroke and traumatic brain injury models.[52-54] Xin et. al. demonstrated that intravenous application of mesenchymal stem cell (MSC)-derived EVs in a perinatal rat model improved neurological outcomes, angiogenesis, and neurogenesis following hypoxia-ischemia injury (HI) in adult murine models.[55] We have also investigated the dose- and time-dependency of brain tissue-derived EV (BEV) treatment on an *ex vivo* brain slice model of neonatal HI.[104] BEV treatment decreased cellular cytotoxicity following ischemic injury, increased anti-inflammatory interleukin (IL)-10 cytokine levels, and a corresponding shift was detected in microglial morphology from pro-inflammatory amoebic to anti-inflammatory and restorative shape modes. Collectively, these results reflect the promising therapeutic role that BEVs play in attenuating inflammation and cell death following HI brain injury, which is the leading cause of morbidity and mortality in neonates.[4]

Though BEVs demonstrate promising results for improving the outcomes of neurological conditions, there exists a lack in understanding BEV behavior that remains a challenge for translational BEV research. The rate and specificity of BEV uptake has been hypothesized to depend on both the EV characteristics and the targeting moieties on the recipient cell, though all known studies on EV-cell interactions have been performed *in vitro*.[40, 47, 121, 122] The EVs derived from *in vitro* cell culture and applied to 2D platforms do not recapitulate the characteristics of native EVs found in a 3D tissue environment.[59, 60, 65, 66] It is unknown what cells EVs localize to in native brain tissue or how different brain pathologies affect EV movement within the tissue. For advancements in EV research to have the greatest potential for therapeutic use, understanding the regional distribution of BEVs, cellular localization, and their transport

properties through tissue is necessary to characterize their role in the brain and can inform the design of future BEV therapeutics.

Changes in brain microstructure, transport properties, and cellular viability during injury may affect BEV behaviors and cellular associations in tissue that aren't observed in an *in vitro* 2D environment.[69] Current EV tracking methods have important limitations when applied in 3D, ex vivo, or in vivo environments, including high costs of operation, limited tissue penetration depths, and semi-qualitative data outputs that make them less applicable and accessible.[92, 123, 124] For example, direct labeling of the lipid membrane using lipophilic dyes is considered the gold standard EV-labeling technique due to its wide accessibility.[123] However, these dyes can leak from the EV membrane leading to non-specific labeling of other lipid contaminants, are prone to photobleaching, have low tissue penetration, and provide only semi-qualitative output in the form of fluorescence intensity across images.[92, 95] To overcome these limitations, we utilize a click chemistry approach to both label and track BEVs with either quantum dots (QDs) or oligonucleotide biobarcodes (oligobarcodes).[106, 125] This approach uses a fast and efficient coupling reaction to allow for both qualitative and quantitative data output, is translatable across all EV platforms, and is also accessible as it only requires universally standard PCR techniques.

Qualitatively, QD conjugation to BEVs allows us to track BEV behavior within brain tissue models using multiple particle tracking (MPT) and confocal imaging. MPT is a technique that can be used in biological environments, including brain slices, under different conditions to evaluate particle deviation from random Brownian motion where individual particle displacement is microscopically tracked and subject to changes in the

local extracellular microenvironments of the tissues.[67, 69, 126] To our knowledge, there are no published studies that track multiple BEVs real-time in tissue, and BEV transport behavior in tissue microenvironments is still unknown. In addition, since MPT only captures short-time scale (millisecond) EV behavior, confocal microscopy of QD-BEVs can provide information on the cellular association of BEVs over longer periods of exposure time. While QDs tagged to BEVs provide the opportunity to semi-qualitatively assess BEV uptake in cells, oligobarcodes allow direct quantification of BEV uptake in cells. Oligobarcoded EVs (oligo-EVs) are detectable *in vitro, ex vivo,* and *in vivo* and their expression quantified using accessible PCR techniques to provide insight into the localization of semen-derived and brain-derived EVs within the genital tract and brain, respectively. Through this dual approach for labeling BEVs, we can observe BEV regional distribution and cellular associations in the brain, as well as real-time transport behavior in living tissue in both healthy and injury models.

4.3. Methods

4.3.1. Animal Care and Ethics

This study was performed in accordance with the guide for the care and use of laboratory animals of the National Institutes of Health (NIH). All animals were handled according to an approved Institutional Animal Care and Use Committee (IACUC) protocol (#4383-02) of the University of Washington (UW), Seattle, WA. The UW has an approved Animal Welfare Assurance (#A3464-01) on file with the NIH Office of Laboratory Animal Welfare, is registered with the United States Department of Agriculture (certificate #91-R-0001) and is accredited by AAALAC International. Time-mated pregnant female Sprague–Dawley rats (virus antibody-free CD® (SD) IGS,

Charles River Laboratories, Raleigh, NC, USA) were purchased and arrived on postnatal day 5 with a litter of 10, sex-balanced pups. Dams were housed individually with their litter and allowed to acclimate to their environment. Before and after the experiment, each dam and her pups were housed under standard conditions with an automatic 12 h light/dark cycle, a temperature range of 20–26 °C, and access to standard chow and autoclaved tap water.

4.3.2. Organotypic Whole Hemisphere (OWH) Brain Slicing

Following euthanasia with intraperitoneal pentobarbitol overdose, fresh brain tissue was rapidly extracted from P10 male rats, placed in ice cold dissection media, and sectioned into 300 µm organotypic whole hemisphere (OWH) slices using a McIlwain tissue chopper (Ted Pella, Redding, CA).[69] OWH slices were plated onto 6-well plates with permeable cell culture inserts (CellTreat, Pepperell, MA; cat #230601). One OWH slice per insert was plated for QD-BEV studies, while oligo-BEV exposure studies required three OWH slices per insert for improved oligobarcode detection. OWH slices were incubated at 37 °C in 1 mL of 25% slice culture medium (SCM) and 5% CO2 to recover from acute slicing. After 24h, the media was exchanged with fresh 25% SCM.

4.3.3. Oxygen Glucose Deprivation (OGD) exposure of slices

At 4 days in vitro (DIV4), OWH slices were incubated in oxygen-glucose deprived (OGD) media within a hypoxic chamber that was purged with nitrogen gas for 0.5h.[69] Previous work determined that 30 min incubation time under these conditions was sufficient to induce significantly higher cell death compared to healthy slices.[67] Following OGD exposure, slices were removed from the hypoxic chamber and fresh pre-warmed 25% slice culture media replaced the OGD media. QD-BEVs (1.3×10^{10} particles/mL

dosage of QD-BEVs) and oligo-BEVs (1.0 x 10^9 molecules of oligo-BEVs) were topically added onto the slice immediately following oxygen glucose deprivation conditioning (OGD). For oligo-BEV studies, 5-7 biological replicates were performed, with each biological replicate consisting of 3 slices. For QD-BEV localization studies, 5 biological replicates per condition per region were analyzed, with 3-4 images taken per region.

4.3.4. Isolation of Brain-Derived Extracellular vesicles (BEVs)

BEVs were isolated from whole, perfused neonatal male rat brains extracted from P10 rats.[104, 106] Brain tissue was prepared using a combination of ultracentrifugation, ultrafiltration, and size exclusion chromatography (SEC),[104] and BEV fractions were collected and stored at -80°C until studies were performed.

4.3.5. Conjugation of quantum dots (QD) to brain-derived extracellular vesicles (QD-BEV)

A modified method from Zhang et.al. was used to conjugate quantum dots (QD) to BEVs for confocal imaging and multiple particle tracking studies.[106] QDs functionalized with PEG-NH_2 (Invitrogen, Waltham, WA; cat #Q21511MP) were added to a PBS solution containing Sulfo-S-4FB (4FB) (VectorLabs, Newark, CA; cat #S-1008-010). This mixture of QD-PEG-NH_2 and 4FB was vortexed vigorously and left on ice to create a QD functionalized conjugate (QD-4FB). BEVs were added to Sulfo-S-HyNic (HyNic) (VectorLabs, Newark, CA; cat #S-1011-010) and vortexed to conjugate BEVs to HyNic molecules (BEV-HyNic). Both QD-4FB and BEV-HyNic solutions were incubated in the dark at room temperature for 2 hours on a rotating stand to ensure linker binding onto the QD and BEV. After incubation, QD-4FB was purified by a NAP-5 column (GE Healthcare, Chicago, IL; cat #GE17-0853-01), and BEV-HyNic was purified using an

ultrafiltration unit with a 100kDa molecular weight cut-off (Milipore Sigma, Burlington, MA; cat #UFC910024). The sample was ultracentrifuged at 3214 x g for 30 minutes to remove unbound, excess Sulfo-S-HyNic.

Purified QD-4FB and BEV-HyNic were combined and left in the dark on a rotating stand for 2 hours to ensure successful click chemistry reaction between QD-4FB and BEV-HyNic. A SEC column was used to separate fully conjugated QD-BEVs from unconjugated QD-4FB and fractions 7-9 (2.5mL total) were collected. A control sample containing unconjugated QD-4FB (fQD) was also purified to ensure that no artifacts were introduced during the BEV conjugation procedure. A final QD-BEV concentration was performed using an Amicon 50kDa molecular weight cut-off ultrafiltration unit ultracentrifuged at 3214x g. QD-BEV conjugates are stored at 4°C for a maximum of 3 days. QD-BEVs at a concentration of $1.3x10^{10}$ P/mL were applied topically to brain slices immediately after OGD.

4.3.6. QD-BEV regional localization studies on ex vivo brain slices

QD-BEVs were immediately applied to OWH slices on DIV4 (1.3×10^{10} P/mL dose) following OGD conditioning and incubated at 37°C for 24h. At the 24h timepoint, slices were formalin fixed and stained with Iba-1 (1:250 dilution) (VWR, Radnor, PA: cat #100369-764) and TOPRO (1:1000 dilution) (Thermofisher, Waltham, MA; cat #T3605) to label microglia and cellular nuclei, respectively. A Nikon A1R confocal microscope was used to image OWH brain slices. Three to five images were captured of the cortex and striatum at 40X, 60X, and 100X magnification. Confocal images were processed with ImageJ and the QD channel (555nm) was thresholded to reduce background autofluorescence (**Error! Reference source not found.**). ImageJ was used to quantify

the overall QD fluorescence signal intensity across the entire image. For microglial density and QD-BEV association counts, confocal images taken at a Z-stack of 25um thickness. The Z-stack tool in ImageJ was used to compress each channel into one image with maximum intensity that was used to manually count microglial density.

4.3.7. Multiple Particle Tracking (MPT) of QD-BEVs in ex vivo brain slices

On DIV5, slice culture media was exchanged for 1 mL of pre-warmed 25% slice culture media containing Hoechst (8 drops/mL, Thermo Fisher Scientific, Waltham, MA, cat #R37605). Slices were incubated for 1 h at standard culture conditions, then washed twice with 1 mL warm (37 °C) slice culture media for 3 min each. Following the second wash, a dose of $1.3x10^{10}$ P/mL of QD-BEVs or fQDs were topically added to each brain slice for 5, 30, or 60 minutes prior to imaging, though all reported videos were from 30-minute incubation times as longer timepoints showed severely decreased particle mobility (Supplemental Fig. 2). Slices were transferred to a glass imaging dish (VWR, Radnor, PA; cat #75856-742) and kept in a temperature-controlled incubation chamber maintained at 37 °C, 5% CO_2, and 80% humidity during the imaging session. Videos were collected at 67 frames-per-second and 100x magnification (oil immersion, 1.45 numerical aperture, Nikon Corporation) for 651 frames via fluorescent microscopy using a cMOS camera (Hamamatsu Photonics, Hamamatsu City, Japan) mounted on a confocal microscope. QD-BEV trajectories are computationally detected and tracked using the ImageJ plugin TrackMate. For MPT studies, 5-7 biological replicates were tracked per condition with 3 videos taken per sample.

4.3.8. Multiple Particle Tracking (MPT) analysis

Nanoparticle trajectories, trajectory mean square displacements (MSDs), and effective diffusive coefficients (D_{eff}) were extracted from confocal microscopy videos via a lab-developed Python package diff_classifier for parallelized and reproducible MPT workflows.[127, 128] The TrackMate plugin generates segmented trajectories for each video that provide particle positions in the x- and y-dimension at each frame of the video (Supplemental Fig. 3). From this, geometric ensemble averaged precision-weighted trajectory MSDs (<MSD>) were calculated for each trajectory and timestep. Each captured video was inspected and QD-BEV trajectories that were deemed not appropriate for analysis due to blinking or light diffraction rings were manually removed from the data files. In addition to D_{eff} distributions, the anomalous diffusion exponent for each trajectory, α , was calculated using diff_classifier.[127] Trajectories were categorized as either subdiffusive (α <0.9), normally diffusive (0.9≤ α ≤1.1), or superdiffusive (1.1< α) based on values reported in literature.[129, 130]

4.3.9. Conjugation of oligobarcodes to brain-derived extracellular vesicles (Oligo-BEV)

Oligobarcode click chemistry conjugation with BEVs has been described in Nguyen et.al. to conjugate short oligonucleotide barcodes (oligos) (Thermofisher, Waltham, MA; cat #4427975) to BEVs. Briefly, BEVs were added to a HyNic working solution (VectorLabs, Newark, CA; cat #S-1011-010) to create BEV-HyNic conjugates, while oligobarcodes were added to a 4FB working solution (VectorLabs, Newark, CA; cat #S-1008-010 to be used as a blank control without BEV conjugation (oligo-4FB). BEV-HyNic and oligo-4FB solutions were incubated in the dark at room temperature on

a rotating stand for 2 hours. After incubation, oligo-4FB was purified by a NAP-5 column (GE Healthcare, Chicago, IL; cat #GE17-0853-01) and BEV-HyNic was purified using an ultrafiltration unit with a 100kDa molecular weight cut-off (Milipore Sigma, Burlington, MA; cat #UFC910024). The unit was ultracentrifuged at 3214 x g to remove excess, unconjugated Sulfo-S-HyNic for 30 minutes.

Purified oligo-4FB and BEV-HyNic were combined and left in the dark on a rotating stand for 2 hours to ensure successful click chemistry reaction between oligo-4FB and BEV-HyNic. A SEC column was used to separate fully conjugated oligo-BEVs from unconjugated oligo-4FB and fractions 7-9 (2.5mL total) were collected. A control sample containing unconjugated oligo-4FB (blank oligobarcode) was also purified to ensure that no artifacts were introduced during the BEV conjugation procedure. A final oligo-BEV concentration was performed using an Amicon 50kDa molecular weight cut-off ultrafiltration unit ultracentrifuged at 3214 x g. Oligo-BEV conjugates are stored at 4°C, and the hydrodynamic diameter ranged from 140-250nm and concentration was measured to be between 1-4x10^{10} P/mL by nanoparticle tracking analysis.

4.3.10. Oligo-BEV exposure in ex vivo brain slices

Oligo-BEVs (10^9 oligo-BEV molecules) were topically administered to *ex vivo* brain slices following OGD on DIV4. After 24 and 48h brain slices were collected and chemically and manually digested in a Hibernate-E buffer containing collagenase and protease and phosphotase inhibitors. Following digestion, samples are spun down at 450g for 10 minutes to pellet cells and resuspended in 25μL of DNAse free H_2O. Samples were immediately heated at 95°C for 8 minutes to release oligobarcodes and gDNA into solution. Oligobarcodes are amplified using stemloop conversion followed by

a preamplification PCR reaction prior to oligobarcode detection via qPCR. Pre-amplification products were diluted 1:4 in TE buffer to be run with quantitative PCR (qPCR). For a 20μL total reaction volume per well, 10μL of Taqman Proamp Master Mix is combined with 1μL of each 20X primer-probe mix, 7μL DNAse free H_2O and 1μL of diluted pre-amplification sample. Thermocycler conditions used were: 1) denaturing at 95°C for 20 seconds, followed by 2) annealing/extension for 45 cycles of 95°C for 1 second and 65°C for 25 seconds. Samples were run with a multi-channel setting to collect fluorescent signals concurrently from the oligobarcode (FAM) and genomic GAPDH DNA (HEX) probes. Captured oligobarcode fluorescence signals were normalized by genomic DNA signals prior to calculating fold changes between conditions.

4.3.11. Fluorescence Activated Cell Sorting (FACS) of microglia from brain slices

OWH slices (6 slices per condition) were collected and digested on ice with accutase (Millipore Sigma, Newark, CA; cat #SCR005) solution. Following accutase digestion, the cell suspension was manually titrated using a pipette, filtered through 70μm cell strainers, and washed with dissociation buffer consisting of 1X HBSS (Thermofisher, Waltham, MA; cat #14025076) and 1M HEPES (Thermofisher, Waltham, MA; cat #15630080) to collect a single cell suspension. Collected cells were pelleted and resuspended with Percoll density gradient media (Cytiva #17089101) to a total of 33% Percoll solution. FACS media consisting of 1X HBSS, FBS (Milipore Sigma, Newark, CA; cat #12306C), and 1M HEPES was slowly overlaid with the Percoll solution, and the cell suspension was ultracentrifuged at 800xg for 15 minutes using the lowest brake setting. There were 3 resulting layers: a thin layer of myelin film at the

interface, the supernatant, and the pellet. Everything but the pellet was discarded, and the pellet was resuspended in FACS media. Anti-rat Fc block (BD Pharmingen, Franklin Lakes, NJ; cat # 550270) was added to the cell suspension at a 1:100 dilution for 5 minutes on ice. Cell suspensions were stained with the following antibody panel for 45 minutes: DAPI nuclear stain (1:10000 dilution, Thermofisher, Waltham, MA; cat # D1306), FITC anti-rat CD11b (1:50 dilution, BioLegend, San Diego, CA; cat # 201805), and PE-Cy7 anti-rat CD45 (1:50 dilution, BioLegend, San Diego, CA; cat # 202213). Isotype control antibodies were used (FITC Mouse IgG2a k Isotype Ctrl Antibody (Biolegend, San Diego, CA; cat # 400207), PE/Cy7 Mouse IgG2a k Isotype Ctrl Antibody, Biolegend, San Diego, CA; cat #400126). Following incubation, stained cells were pelleted and washed 3 times with FACS media to reduce background signal. Cells were sorted using a BD FACS Aria III and both $CD11b^{+}/CD45^{+}$ (microglia) and $CD11b^{-}/CD45^{-}$ fractions were collected for analysis (Appendix C. 4).

4.3.12. Statistical analysis

Statistical analyses were performed in GraphPad Prism version 10.1.1 (GraphPad Software, San Diego, CA, USA). All statistical significance determinations between groups were performed using nonparametric unpaired Mann-Whitney testing. All p-values < 0.05 were considered statistically significant, with p*<0.05, p**<0.005, p***<0.0005, p****<0.00005.

4.4. Results

4.4.1. QD-BEVs exhibited microglial association in both healthy and OGD *ex vivo* slices

QD-BEVs were applied to *ex vivo* slices to determine regional localization. The hydrodynamic diameter of the QD-BEV complexes was measured by nanoparticle tracking analysis (NTA) to range from 170-300 nm, and the average zeta potential was measured to be -11.4 mV. Though BEV treatment on HI brain slices have been shown to actively decrease cell death and alter microglial morphology, it is unclear whether BEV localization patterns are altered by brain injury compared to healthy conditions and if administered BEVs directly localize to microglia.[104] In addition, QD-BEVs associate to *in vitro* glial BV2 cell cultures, but whether they associate with microglia in brain tissue remains unknown.[106] Since BEV regional and cellular fate within *ex vivo* brain slices have not yet been confirmed, we tracked QD-BEVs in real-time to characterize short-term BEV localization patterns in OWH brain slices. In addition, we evaluated the long-term QD-BEV localization in tissues following 24h of QD-BEV exposure. When applied to healthy OWH brain slices, we showed that QD-BEVs associated with microglial soma within 24 hours of application in both the cortex and striatum (Figure 4.15 A-B). In contrast, fQDs that have not been conjugated to BEVs demonstrated high amounts of aggregation in healthy OWH brain slices at the same concentration as QD-BEVs (Figure 4.15 C). Aggregates were not seen in samples exposed to QD-BEVs.

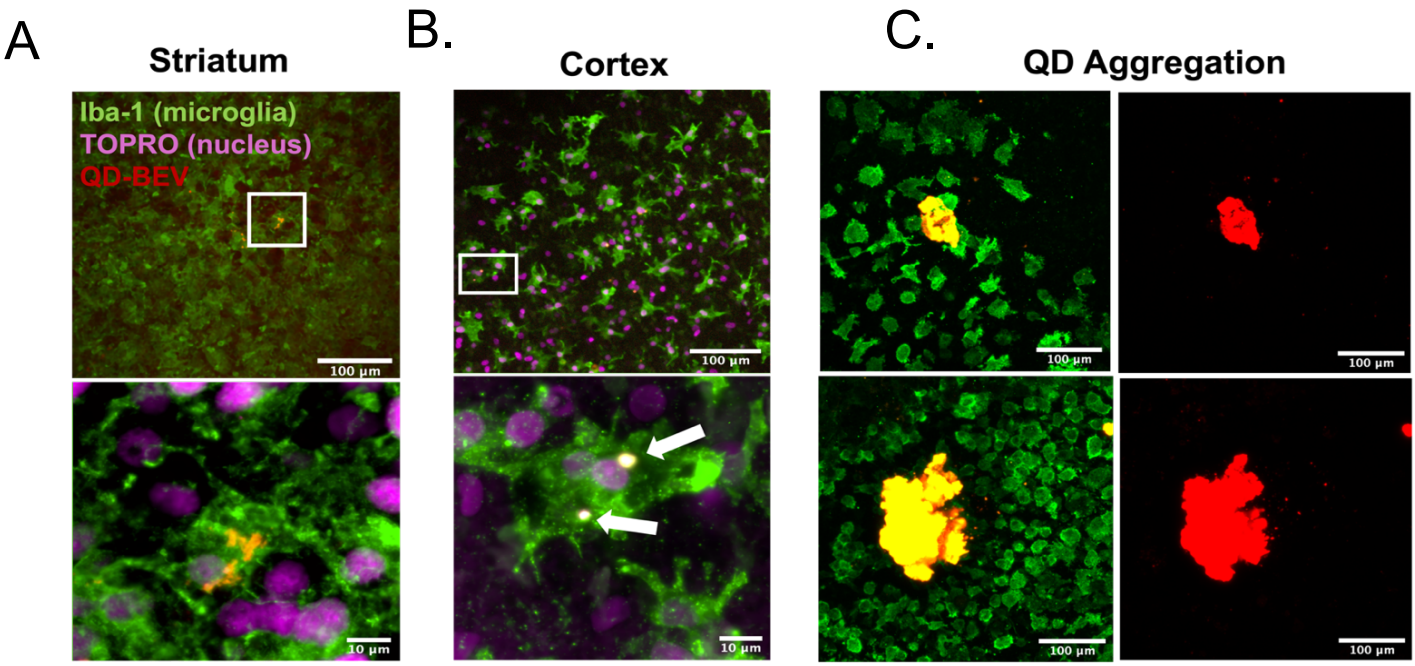

Figure 4.15. QD-BEV association with ex vivo microglia.
Representative confocal images of QD-BEV (red) association with microglia (green) and nuclei (magenta) in A) the striatum and B) the cortex of healthy ex vivo brain slices at 40X and 240X magnification. Colocalization of quantum dots and microglia is represented in yellow. C) Functionalized QDS that have not been conjugated with BEVs form large aggregates when applied to ex vivo healthy brain slices (images taken at 40X). Scale bars: A) top=100 µm, bottom=10 µm, B) top=100 µm, bottom=10 µm, C) 100 µm.

Following the confirmation of QD-BEV microglial association in brain slices, we sought to evaluate macroscale changes in regional distribution of QD-BEVs between the cortex, striatum, and corpus callosum and whether changes in BEV regional distribution is observed following injury. From prior work in this *ex vivo* model, these three regions were used to represent different physiological compositions—the cortex for grey matter, corpus callosum for white matter, and striatum for deep brain regions.[69, 99] We exposed OWH brain slices to OGD to model hypoxia ischemia in a neonatal brain.[69] Of particular interest after 24h of direct QD-BEV treatment is the association of

QD-BEVs to microglia distributed between the three regions, since association was confirmed in single cells *in vitro* and *ex vivo.* Representative confocal images of QD-BEVs (red) and labeled microglia (green) showed the presence of QD-BEVs in the cortex, striatum, and corpus callosum (Figure 4.16 A). To quantify the concentration of QD-BEV, signal intensity is calculated in ImageJ from representative confocal images of each region of interest (Figure 4.16 B). Following OGD exposure, the striatum showed a significant ten-fold increase ($p<0.05$) in QD-BEV signal compared to the cortex for both healthy and OGD conditions.

Trends indicated that OGD conditioning in the brain increased QD-BEV signal intensity across almost all regions investigated, except for the cortex, where the signal intensity is slightly decreased following injury. In contrast, QD-BEV signal intensity is similar between the cortex and striatum in healthy conditions with median values between $3.1\text{-}3.8\text{x}10^4$ fluorescence units, with slightly higher values in the corpus callosum ($6.4\text{x}10^4$ fluorescence units). Taking into consideration differences in cell density across different images that may affect overall signal intensity results, all microglia in each image were manually counted. Microglia were classified into two groups based on whether QD-BEVs were associated with the microglia. An evaluation of the percentage of microglia that are visually associated with QD-BEVs showed that about 40% of microglia in the OGD exposed striatum associated with QD-BEVs, a significant increase ($p<0.005$) to the 20% of BEV-associated microglia in the healthy control (Figure 4.16 C). OGD exposure increased microglial association with QD-BEVs by 6% in the cortex, 20% in the striatum, and 15% in the corpus callosum.

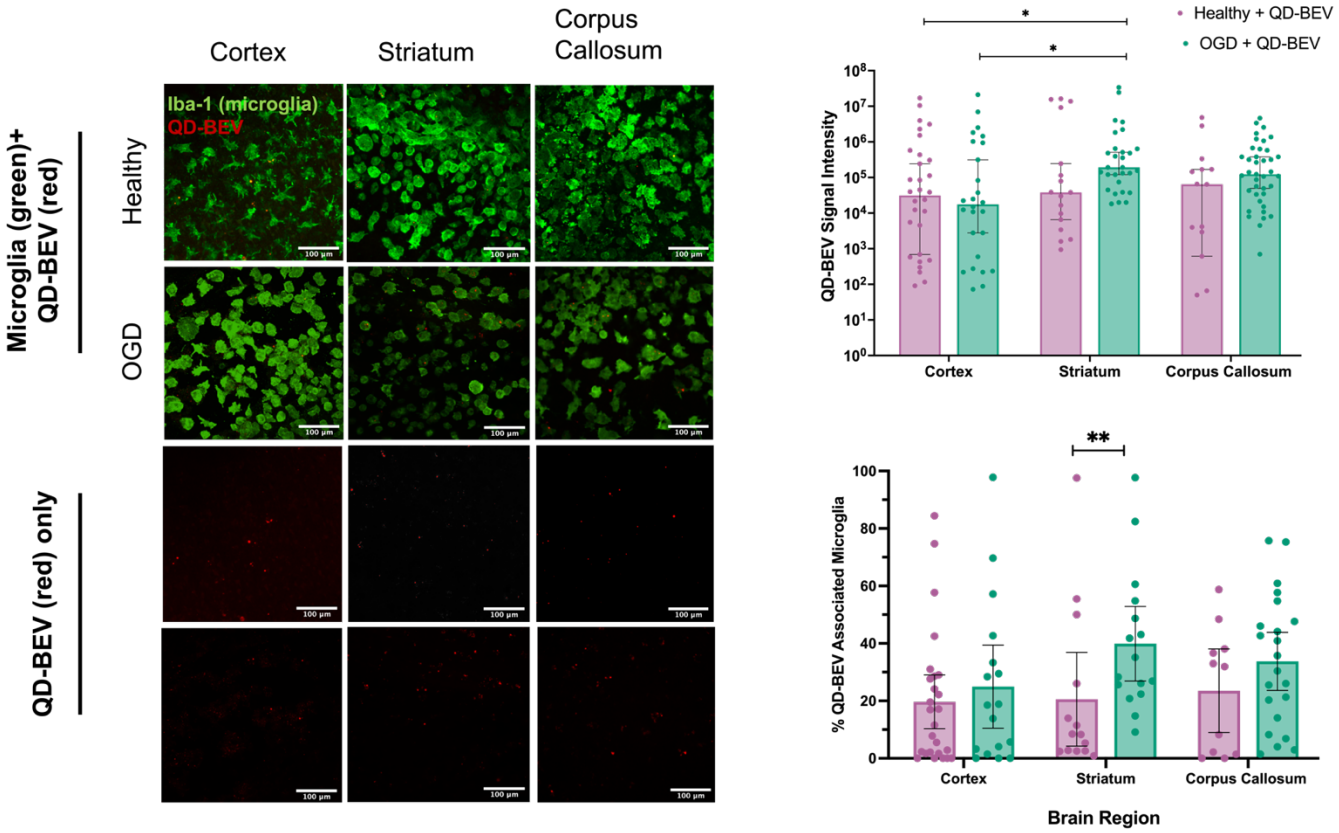

*Figure 4.16. QD-BEV association with microglial cells in ex vivo brain tissue. A) Representative confocal images of QD-BEV (red) association with microglia (green) between healthy and OGD conditioned ex vivo brain slices across the cortex, striatum, and corpus callosum. The first two rows exhibit the overlay of the microglial and QD-BEV channels, while the bottom two rows display only signal from the QD-BEV channel of the same images. B) QD-BEV localization in the cortex, striatum, and corpus callosum in ex vivo brain slices categorized by signal intensity and C) percentage of microglia associated with QD signal. All signal intensities of QD-BEVs are thresholded against the same negative control slice containing no QD-BEVs prior to analysis to reduce background autofluorescence. N=6 biological replicates per condition. Error bars represent B) median with 95% confidence interval and C) mean with 95% confidence interval. A nonparametric Kruskal-Wallis test with multiple comparisons was run for statistical significance testing *p<0.05*

4.4.2. MPT revealed that overall QD-BEV diffusivity is regionally dependent, with shifts in the anomalous diffusion exponent.

In addition to quantifying BEV association with microglia following 24h exposure, QDs were also used to quantify the diffusion patterns of BEVs in brain tissue on shorter timescales and compare them to random, Brownian movement. We analyzed QD-BEV

trajectories acquired from the cortex and striatum of healthy and OGD-exposed brain slices. The cortex is comprised largely of grey matter while the striatum is comprised of both grey and white matter, so comparing QD-BEV diffusivity between both types of matter provides insights to endogenous BEV movement in physiologically different microenvironments.[131, 132]

Our MPT analysis of D_{eff} revealed that the median QD-BEV diffusivity is significantly hindered ($p<0.05$) in the cortex (0.863$\mu m^2/s$) compared to the striatum (1.085$\mu m^2/s$) in healthy brain slices, but this observed statistical significance does not propagate following OGD exposure (OGD cortex: 0.787$\mu m^2/s$, OGD striatum: 1.037$\mu m^2/s$) (Figure 4.17 A, Table 4.3. Median diffusion coefficients from multiple particle tracking of QD-BEVs in brain tissue.). Interestingly, the D_{eff} of QD-BEVs was not injury dependent as there were no statistically significant differences between healthy and OGD conditions between regions. QD-BEVs from all regions and conditions had significantly greater diffusivity compared to control 4FB-functionalized QDs ($p<0.00005$) that were not conjugated to BEVs. fQDs had a median D_{eff} of 0.155 in the OGD exposed tissues and 0.164 in healthy tissues (Figure 4.17. Multiple particle tracking of QD-BEVs in ex vivo brain tissue. A , Table 4.3. Median diffusion coefficients from multiple particle tracking of QD-BEVs in brain tissue.). This was likely due to exposed functional hydrazine groups on the surface of QDs reacting nonspecifically with the tissue environment, leading to increased incidents of nanoparticle aggregation supported in confocal images (Figure 4.15 C). The theoretical D_{eff} of QD-BEVs of the same hydrodynamic size (154.9nm diameter) is 4.25$\mu m^2/s$ in artificial cerebral spinal fluid (viscosity of 6.913 x 10^{-4} Pa/s) at 37°C. QD-BEVs experienced more hindrance when

applied to brain tissues compared to movement in a free media. In comparison to 40nm have polystyrene (PS-PEG) nanoparticles, which are well-characterized particles that has been applied to this same *ex vivo* brain slice platform,[69] QD-BEVs experienced less hindrance in healthy brain tissue. The median D_{eff} of QD-BEVs in the cortex of healthy brain slices was calculated to be 0.864 $\mu m^2/s$. In contrast, the median D_{eff} of PS-PEG nanoparticles in the cortex of age-matched healthy brain slices was plotted as 0.630 $\mu m^2/s$.[69]

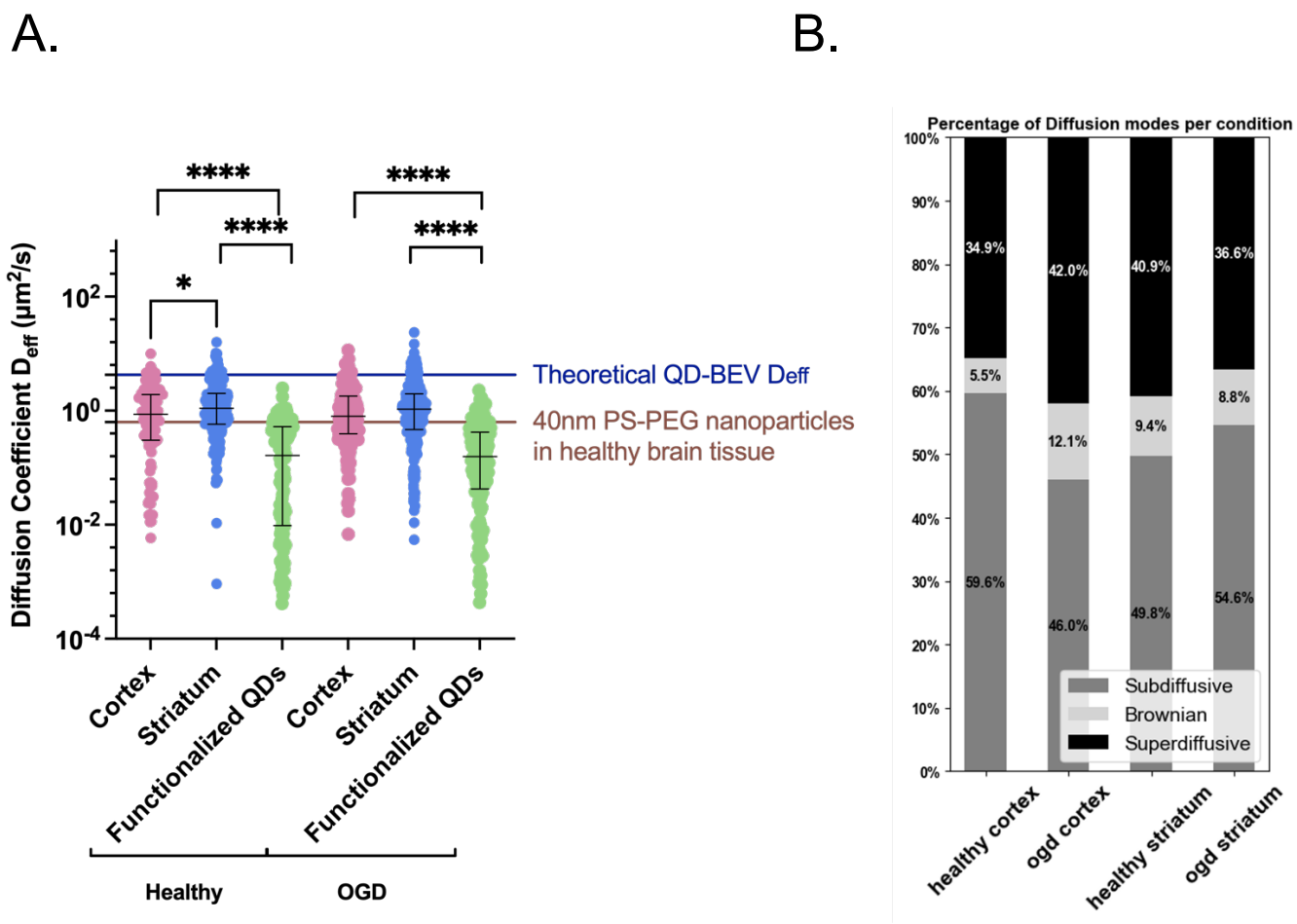

Figure 4.17. Multiple particle tracking of QD-BEVs in ex vivo brain tissue.
A) Diffusion coefficients (D_{eff}) of QD-BEVs and functionalized QDs topically applied to ex vivo brain slices, calculated at 1 second. Diffusion coefficients were measured in the cortex and

*striatum, and compared between healthy and oxygen glucose derived (OGD) tissue conditions. Functionalized QDs were tracked in the striatum. The theoretical $D_{eff.}$ of QD-BEVs in water at 37°C as calculated by Stokes Einstein is indicated by y=2.28 $\mu m^2/s$ and the median $D_{eff.}$ of 40nm PS-PEG nanoparticles in female age-matched brain slices is indicated by y=0.630 $\mu m^2/s$ [McKenna et.al., DOI: 10.1186/s13036-022-00293-w]. Error bars represent the median with interquartile range. Mann-Whitney non-parametric t-tests were performed for statistical significance: *p<0.05, ****p<0.00005. B) Anomalous diffusion exponent (α value) of the diffusive trajectories of the QD-BEVs between the cortex and striatum in healthy and OGD exposed brain slices.*

	Condition	
	Healthy	**OGD**
Cortex	0.864	0.787
Striatum	1.085	1.037
Functionalized QDs	0.164	0.156

Table 4.3. Median diffusion coefficients from multiple particle tracking of QD-BEVs in brain tissue.
Median diffusion coefficient (Deff (μm2/s)) values for the cortex and striatum in the healthy and OGD controls. Median Deff values for functionalized QDs were also measured.

Though bulk QD-BEV measurements of the D_{eff} suggested that there were no significant differences to BEV diffusivity between healthy and OGD tissues, evaluating individual D_{eff} values revealed more detail about the types of diffusion that QD-BEVs individually experience. The anomalous diffusion exponent (α value) of the trajectories were computationally calculated to classify nanoparticle diffusion into sub-diffusive, Brownian, or super-diffusive transport modes.[129, 130] Plots of the α value of QD-BEVs between different brain regions showed that each condition and region had diffusion profiles that changed following OGD (Figure 4.17 B). QD-BEVs in the cortex in healthy conditions had the greatest percentage of subdiffusive particles (60%) compared to all other conditions, with 5% of particles following Brownian diffusion, and 35%

experiencing superdiffusive diffusion. Following OGD exposure, the subdiffusive fraction of particles in the cortex decreased to 46%, while particles that were undergoing Brownian diffusion increased to 12% and superdiffusive particles increased to 42%.

The reverse trends were observed in the striatum between the healthy and OGD controls. In the striatum of healthy brain tissues, only 50% of QD-BEVs experienced subdiffusive diffusion compared to the healthy cortex where 60% of particles were subdiffusive. In the OGD cortex where there was a significant decrease in subdiffusive QD-BEVs following injury from 60% to 46% ($p=0.025$), in the striatum there was a slight increase in the percentage of subdiffusive QD-BEVs from 50% to 54% ($p=0.27$). With this increase in subdiffusive particles in the OGD striatum there was a corresponding decrease in superdiffusive particles from 41% to 37%. In the striatum the fraction of Brownian particles remained similar between healthy and OGD controls at 9%. This hindrance of BEVs in the striatum following injury may be caused by increased cellular debris or extracellular matrix breakdown.

An evaluation of overall cell density between regions showed that the striatum had significantly increased both cell density ($p<0.0001$) and cell death ($p<0.0001$)) compared to the cortex following OGD (Figure 4.18). The average DAPI cell count for the OGD cortex was 133 nuclei, whereas in the striatum the average was 255 nuclei. OGD injury led to increased cell density in the striatum, as well as an increase in cell cytotoxicity of 57% compared to just 3% in healthy slices. These significant differences only occurred following OGD injury, as the cortex and striatum cell count and cytotoxicity levels were statistically insignificant in healthy slices. These results suggest that though our MPT data only revealed significant changes in QD-BEV transport

behavior between brain regions, the tissue microenvironment experienced both regional and injury-dependent changes following injury. These regional and injury dependent changes in the tissue microenvironment in the brain were not captured through bulk D_{eff} analysis alone, emphasizing the need to supplement MPT data with other forms of analysis.

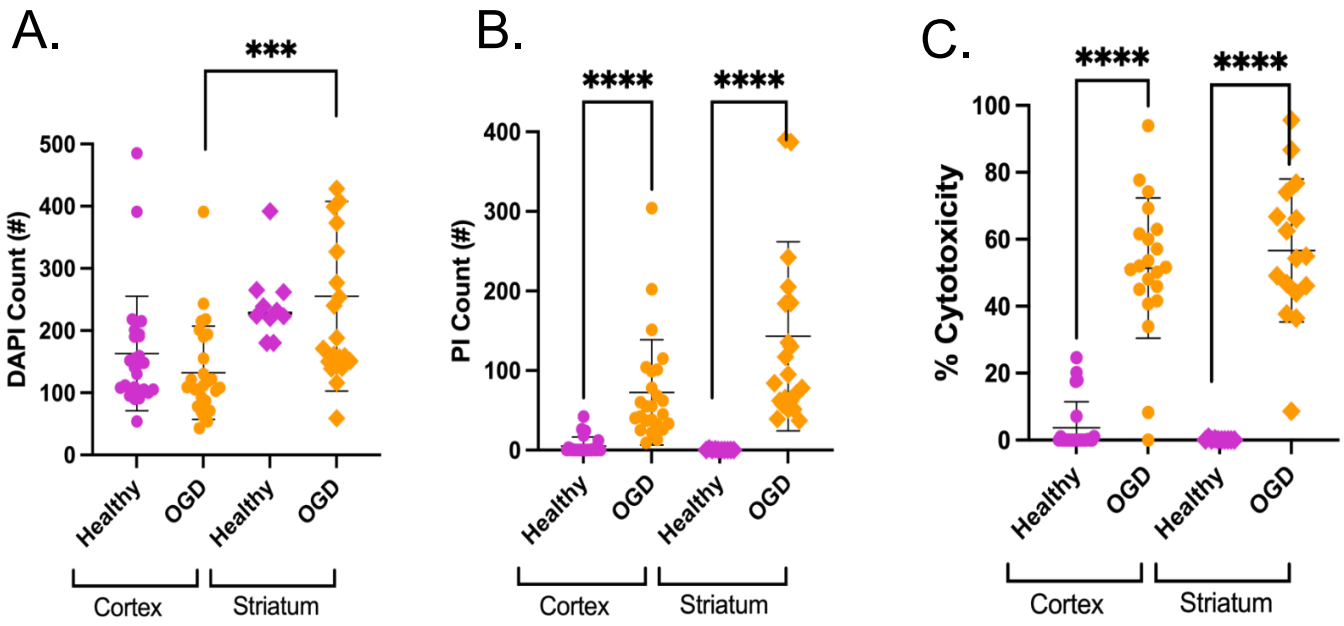

*Figure 4.18. Total cell density and cytotoxicity counts in ex vivo brain slices. Plots comparing the A) number of DAPI-stained nuclei, B) number of propidium iodide-stained nuclei, and C) percent cytotoxicity (PI count/DAPI count) in the cortex and striatum between healthy and OGD ex vivo brain slices. Error bars represent mean with standard deviation. Significance determined with nonparametric Mann-Whitney test. N=6-10 slices, ****=p<0.00005*

4.4.3. Oligobarcoded-BEVs were detected in OWH brain slices up to 48h.

Though the results from QD-BEV studies demonstrated that BEVs associate with cells *in vitro* and *ex vivo*, it is unclear from confocal imaging alone whether they are surface associated or internalized. We hypothesized that there was uptake of BEVs by cells following injury, as BEVs have been shown to improve the cytotoxic outcomes of

OGD-exposed brain slices in a dose- and time-dependent manner.[104] To determine whether tissue slices uptake BEVs, oligo-BEVs and unconjugated oligobarcodes (blank oligobarcode) were topically applied onto healthy and OGD-exposed OWH brain slices. Oligobarcode signals were successfully detected with qPCR in brain slices in both healthy and OGD conditions (Figure 4.19 A). Interestingly, there were no significant changes to oligo-BEV uptake between 24 and 48h. There was a significant 10^4-fold increase ($p=0.0442$) in oligo-BEV signal compared to blank unconjugated oligobarcode signal at both 24 and 48h, which demonstrates that brain slices are preferentially taking up the oligobarcode-BEVs over the blank oligobarcodes (Figure 4.19 A). Oligobarcode signals were consistently detected to be between 10^3 – 10^4-fold-greater than blank oligobarcodes. Specifically, oligo-BEVs had significantly greater uptake than blank oligobarcodes in almost all conditions excluding when applied for 24h on OGD slices, indicating that there may be a time-dependent component to oligo-BEV uptake in tissue following injury. Though these experiments evaluated tissue-scale uptake of oligo-BEVs, we sought to further investigate the cellular level uptake of BEVs.

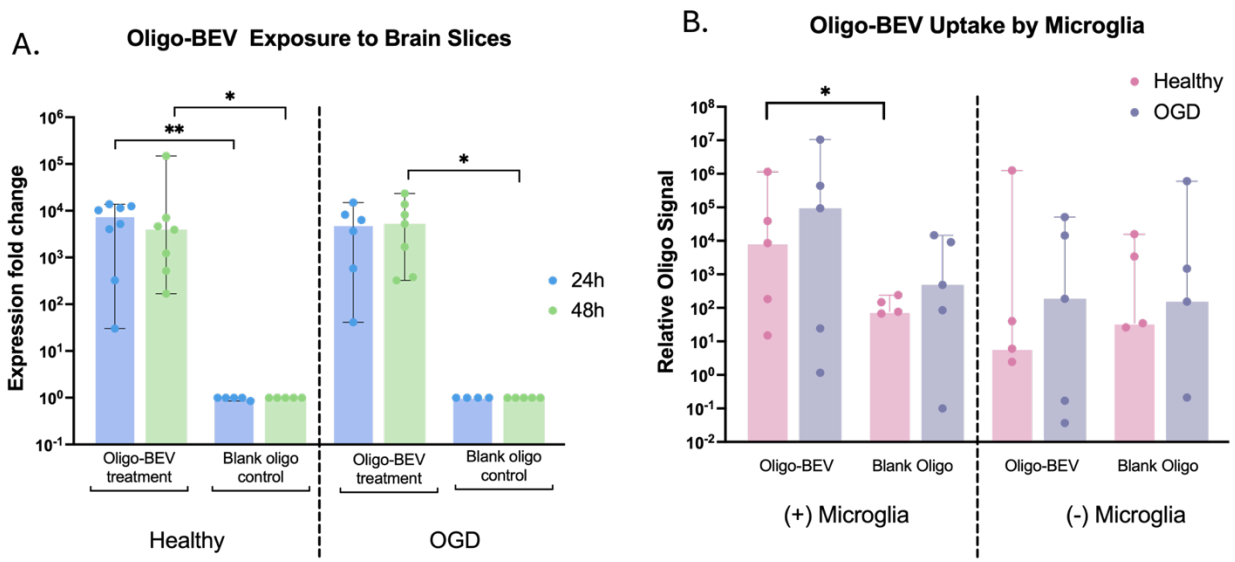

Figure 4.19. Oligobarcoded BEV (oligo-BEV) exposure on ex vivo brain tissue for 24 and 48h. A) Healthy and OGD-conditioned brain slices were compared for oligobarcode detection. Oligobarcode signal was measured with fluorescent probe-based qPCR and normalized against a housekeeper gene (GAPDH). were normalized against the level of blank oligo expression detected (negative control). There is a $10^4 - 10^5$ *fold increase in oligobarcode-BEV signal compared to blank oligobarcode signal in both timepoints and tissue conditions. N=3-4, bars plot mean with standard deviation. B) Fluorescence-Activated Cell Sorting of microglia from ex vivo brain slices treated with oligo-BEVs for 24h.* $CD11b^+/CD45^+$ *microglia are isolated. Oligo-BEV and blank oligobarcode signal is compared to a non-treated control between healthy and OGD conditions. Oligo-BEV and blank oligobarcode uptake is quantified within FACS separated microglial and non-microglial cell populations. Fold changes in oligobarcode detection are normalized against non-treated control slices. Statistics on data were performed using a non-parametric Kruskal-Wallace multiple comparisons test *p<0.05, **p<0.005*

4.4.4 BEVs interact with both microglia and non-microglial cell populations following FACS analysis.

Oligo-BEV uptake results in *ex vivo* tissues demonstrated that there was significant BEV uptake by brain tissue compared to blank oligobarcode following administration. However, as brain slices are comprised of a heterogenous population of cells, it is unknown which cell types oligo-BEVs localize to, and whether cell-specific uptake of oligo-BEVs is injury dependent. BEV treatment on OGD exposed slices have been shown to encourage microglia to shift from an inflammatory phenotype to a restorative phenotype, indicating therapeutic potential.[104] Microglia are highly dynamic

cells that are considered to be the resident immune cells of the brain responsible for initiating immune response to injury, including in response to hypoxia ischemia.[15, 133] Therefore, we sought to investigate microglia-specific uptake of oligo-BEVs within our *ex vivo* slice models.

After oligo-BEV exposure, FACS was performed on washed and digested brain slice tissues to sort CD11b+/CD45+ expressing microglia followed by qPCR on microglial (+microglia) and non-microglial (-microglia) fractions to detect oligo-BEV signal in both populations. As the OWH slices are removed from the blood supply and are cultured for several days on semi-permeable membranes, there were no infiltrating macrophages from the circulatory system to separate from the microglia. When evaluating cell-specific uptake of oligo-BEVs, there was a significant increase in oligo-BEV uptake compared to blank oligo in microglia from healthy tissues ($p=0.0317$) (Figure 4.19 B). There is a noticeable trend that oligo-BEV uptake in +microglia fractions is greater compared to -microglia fractions. Microglia in healthy controls exhibited about a 40-fold increase (8007.8 units of relative oligo signal in +microglia vs. 496.46 relative oligo signal in -microglia) in oligo-BEV uptake over -microglia. This trend is heightened following OGD injury, where there is about a 6000-fold increase in oligobarcode signal in microglia compared to -microglia.

Overall, there were also no overall significant changes in uptake of blank oligo between +microglia and -microglia between healthy and OGD conditions. However, the non-microglial population maintained consistent oligobarcode signal for both oligo-BEV and blank oligobarcode controls. The -microglia fraction exhibited between 23-52 units of relative signal across all groups besides in the healthy condition, where oligo-BEV

detection was 496 units of signal. In addition, -microglia fractions consistently exhibited lower oligobarcode signal compared to +microglia and had similar relative signals of oligobarcode across all samples. Promising trends in this FACS data indicated that +microglial fractions in healthy and OGD tissues uptake more oligo-BEVs.

4.5. Discussion

We utilized a fast and efficient click chemistry conjugation to tag BEVs with either QDs or oligobarcodes to allow for both qualitative and quantitative probing of BEVs in brain tissue. We demonstrated that QD-BEV complexes associated with microglia in *ex vivo* brain tissues in a region-dependent manner. There was a significant ten-fold increase in QD-BEV signal in the striatum compared to the cortex following OGD exposure that was supported by microglial association analyses when normalizing the signal intensity of QDs by microglia count. This result highlights the importance of considering the regional dependence of EV localization in the brain when designing future therapeutics. It is important to note that we did not perform a control using a blank nanoparticle with a similar geometry to an EV, such as a liposome, to test whether the regional dependence of EVs might be a result of the EV size or geometry, rather than targeting moieties on the EV surface. Though it is known that proteins on the surface of EVs are crucial to cell uptake, and even cell-*specific* uptake, further studies comparing the localization of blank liposomes to EVs will inform scientists of the impact that nanoparticle geometry and size play in determining localization.

In combination with QD conjugations that aided in probing regional BEV localization and confirmed microglial BEV association, novel oligobarcode conjugations were used to evaluate BEV cellular uptake. Oligo-BEVs exhibited significantly greater

uptake in bulk *ex vivo* brain tissues compared to unconjugated blank oligobarcodes. This result was supported with FACS separation of microglia, where the results also indicated a significant increase of oligo-BEV uptake in microglia compared to blank oligobarcodes. Even among non-microglial populations (-microglia) the levels of oligo-BEV uptake were generally increased compared to blank oligobarcode following OGD. Together these results indicate that BEVs are not only experiencing region-dependent association with microglia, but microglial populations also preferentially uptake BEVs over blank oligobarcodes. These findings are consistent with the responsive role microglia play in the brain, especially following OGD. Tissue damage invokes the acute release of damage associated molecular patterns (DAMPs) such as reactive oxygen species, necrotic cells, and damaged mitochondria.[134, 135] Microglia, as the primary immune cell responders to injury, respond to DAMPS by increasing their phagocytotic activity and producing an influx of inflammatory and anti-inflammatory cytokines and chemokines within 24h.[14] Microglia are well documented to become increasingly phagocytotic, proliferative, and active in response to ischemic brain injury, which may explain the trends of increased QD-BEV association with cells observed in our confocal and FACS data.[135-137] It has also been shown that microglia produce a strong response to EVs during injury repair mechanisms.[138, 139] It is important to note that even among the microglial population there are high levels of heterogeneity in autofluorescence and surface markers as microglia are biologically dynamic, with subsets that are differentially impacted by genetic variations and pathologies.[140, 141] Due to this heterogeneity, it is possible that $CD11b^{+}/CD45^{+}$ FACS gating only captured a subset of activated microglia and the oligo-BEV uptake is underestimated in our results.

Our MPT analysis of QD-BEV behavior provided new insights that QD-BEV diffusion was regionally dependent. BEVs experienced more hindrance in brain tissue compared to a hypothetical situation where BEVs are freely diffusing in artificial cerebral spinal fluid. This hindrance is attributed to interactions of the BEVs with the tortuous extracellular environment and cells.[69, 142] When compared to 40nm PS-PEG nanoparticles in the same *ex vivo* rat slice models, QD-BEVs experienced greater overall diffusivity. PS-PEG nanoparticles are inert with a near-neutral surface charge and are thus unlikely to interact electrostatically or chemically to the surrounding tissue environment. [69] In contrast, as BEVs present various surface moieties involved in cellular signaling, QD-BEVs are expected to experience facilitated interactions with cells in the environment.[143, 144] It has been previously reported that EVs exhibit greater intracellular diffusivity compared to synthetic nanoparticles due to increased interactions with motor proteins in the cytoskeleton.[145, 146] BEV membranes also contain a high concentration of phospholipids, cholesterol, and aquaporins that decrease hydrocarbon chain packing, allowing EVs to be more deformable and have greater membrane fluidity and water permeability.[147, 148,47, 148] Due to the flexible and permeable membrane of EVs, there are reports of rapid *in vivo* internalization and degradation of injected and endogenous EVs by macrophages and monocytes.[124]

In light of the regionally dependent behavior of BEV localization and transport in brain tissue, we determined that that there were notable regional changes in the brain following injury that is supported by previous research.[67, 69] There is a significant increase in the overall cell density, number of dead cells, and cytotoxicity in the striatum compared to the cortex. This rise in striatal cell density and debris in addition to the

breakdown of extracellular matrix can hinder BEV diffusion as seen in our results. Alternatively, the hindered diffusion of QD-BEVs following OGD may also be attributed to overall EV destabilization. The OGD model restricts available oxygen supply in the tissue, leading to acidosis of the extracellular milieu.[12, 149, 150] This acidification can destabilize EV associated proteins and result in decreased diffusivity of EVs in tissue.[151, 152]

Though QD-BEV conjugations pose several advantages over other forms of EV labels, there may be concerns that QD conjugation affects BEV localization. [99, 153] Notably, Zhang et.al. found QDs with different surface functionalities can associate with microglia *ex vivo* and *in vivo* in rats, with strong dependence on the brain region and some dependence on the QD surface functionalization.[99] Our findings align with this regionally dependent microglial interaction. However, QD-BEVs demonstrated different localization patterns, as the striatum had significantly high accumulation of QD-BEVs compared to other regions. Microglia in the striatum were observed to experience significant QD-BEV uptake after 24h of exposure, the extent of which was increased following OGD. In contrast, fQDs formed aggregates that were not observed in any QD-BEV samples that may be due to altering EV endocytosis and exocytosis pathways.[153] This lack of aggregative behavior following BEV conjugation to QDs suggests that BEVs that are inherently functionalized with molecular moieties that interact with cells and are likely responsible for driving regional distribution. Though EVs strongly associate with microglia, the distribution of EVs to other cell types would be of interest to study. In future studies, different cell types such as neurons and oligodendrocytes can be co-

stained with microglia to reveal the distribution of QD-BEVs in specific cellular populations of the brain.

4.6. Conclusion

Though BEVs demonstrated promising therapeutic effects in mitigating HI brain injury and are critically involved in regulating tissue repair, a lack of clarity on the localization and transport of BEVs in brain tissue restricts translational research in this area. We utilized a quick and efficient click chemistry to tag BEVs with QDs and oligobarcodes to probe BEV behavior qualitatively and quantitatively in endogenous brain tissue. We demonstrated that BEVs associated with microglia on *ex vivo* brain tissues and that cellular association with BEVs increased following OGD injury, particularly in the striatum. Regional differences were also seen in our MPT analyses of regional diffusion coefficients between healthy and injured conditions, which may be due to extracellular matrix breakdown and increased cell death. Novel oligobarcoding was also deployed to track BEV cellular uptake in *ex vivo* brain slices. Our results demonstrated that oligo-BEVs were preferentially taken up by microglia compared to blank oligobarcodes. Through the use of both qualitative image analyses using QD probes and quantitative analysis using oligobarcodes, we successfully evaluated the region-dependent and cell uptake behaviors of BEVs in endogenous brain tissue. Future evaluations of EV localization and transport must consider the importance that regional variances and pathological states play in EV behavior.

4.7. Data Availability Statement

The data can be provided upon request to the corresponding author. Python software is accessible via Nance-Lab/diff_classifier.[127]

4.8. Conflicts of Interest

The authors report no conflicts of interest.

4.9. Acknowledgements

This work was supported by the National Institute of General Medical Sciences (Grant #R35GM124677) and the Data Sciences Initiative in the Department of Chemical Engineering at the University of Washington. Research reported in this publication was also supported by the National Center for Advancing Translational Sciences of the National Institutes of Health under award number TL1TR002318 (Nguyen). The content is solely the responsibility of the authors and does not necessarily represent the official views of the National Institutes of Health. Part of this work was conducted at the Department of Laboratory Medicine and Pathology Flow Cytometry Core Facility at the University of Washington. We thank Brendan Butler and Emily Du on providing cell counting data for our MPT analysis that contributed to Figure 4.18.

Chapter 5. Research Summaries of Published and Ongoing Work

5.1. Brain tissue-derived extracellular vesicle mediated therapy in the neonatal ischemic brain

Nguyen, N. P., Helmbrecht, H., Ye, Z., Adebayo, T., Hashi, N., Doan, M. A., & Nance, E.* (2022). Brain tissue-derived extracellular vesicle mediated therapy in the neonatal ischemic brain. *International journal of molecular sciences*, *23*(2), 620.

*Corresponding author

Hypoxic-Ischemic Encephalopathy (HIE) in the brain is the leading cause of morbidity and mortality in neonates and can lead to irreparable tissue damage and cognition. In developed countries up to 4 out of every 500 live births suffer HIE, and this number is tripled to 13/500 in underdeveloped countries.[1, 3-5] In addition to high incidence rates, about to 1/3 of neonates who survive the initial onset of HIE are at risk of developing long-term cognitive disabilities or neurological disorders such as epilepsy or cerebral palsy.[3, 154] Due to the severity of this condition and the lack of an existing cure for HIE, it is important to investigate key mediators of HIE injury response to develop future therapeutics. Tissue repair requires highly coordinated cellular responses mediated by cell-derived extracellular vesicles (EVs). In contrast to the majority of EV studies that utilize EVs derived from *in vitro* cell culture, we successfully isolated and characterized EVs from whole brain rat tissue (BEV) to maintain physiological relevance. We showed that BEVs decreased cytotoxicity in an *ex vivo* brain slice model of HI in a dose- and time-dependent manner. The minimum therapeutic dosage was determined to be 25 μg BEVs, which corresponded to increased anti-inflammatory IL-10 cytokine expression. We also evaluated changes in microglia morphology to supplement our therapeutic efficacy studies. Microglia are the

resident immune cells of the brain and experience diverse injury-driven phenotypic changes.[15, 135, 155, 156] We used computational methods to detect microglia in our imaging samples and compute their various shape parameters to quantify changes in morphology.[157] In injured tissues, the morphology of microglia was also observed to shift from an amoeboid, inflammatory phenotype to a restorative, anti-inflammatory phenotype following BEV exposure. These results demonstrated that BEV administration on an *ex vivo* model of HI can decrease cellular cytotoxicity, increase anti-inflammatory signaling, and shift microglial morphology away from an inflammatory to an anti-inflammatory phenotype. These studies outlined the therapeutic potential of tissue derived BEVs for treating HI at small doses and a wide application time window. These promising results encourage future studies on tissue EVs and their role in alleviating inflammation in the brain.

5.2. Novel Oligonucleotide Biobarcodes for Labeling Extracellular Vesicles

Nguyen, N. P., Asencio, M., Paktinat, S., Nance, E., Vojtech, L.* *In preparation,* 2024.
*Corresponding author

There has been heightened interest in studying extracellular vesicles (EVs) due to their therapeutic potential across many models and diseases. To support the workflow of detecting and tracking EVs, accessible and sensitive methods for EV labeling are needed. Current methods for visualizing the trafficking of extracellular vesicles (EVs) rely on fluorescent labeling and microscopy to reveal their location. However, these methods are not fully quantitative and suffer from false-positive signals and unfavorable signal-to-noise background when analyzing tissue samples.[92, 94, 96, 123] Furthermore, they require specialized microscopes and instrumentation which are

expensive, not accessible in many locations, and necessitate extensive user training. Here, we sought to develop a method to label EVs with short oligonucleotide "biobarcodes", enabling detection in tissues by standard quantitative PCR techniques. We engineered a short (22 base) DNA oligonucleotide based on the *C. elegans* microRNA cel-miR-39 modified with a 5-prime amine group for click chemistry compatibility. Additional phosphorothioate bonds increase stability against exonucleases when applied *in vitro, ex vivo,* and *in vivo*.

We conjugated the oligonucleotide barcodes (oligobarcodes) to EVs isolated from human semen (SEVs) and from whole neonatal rat brains (BEVs) and administered to *in vitro* cell or *ex vivo* tissue cultures to examine the fate of SEVs and BEVs with different cell populations. To detect the oligobarcoded SEVs (oligo-SEVs) we utilized a three-step PCR protocol using stem-loop primer and pre-amplification, followed by quantitative PCR with an assay utilizing a locked-nucleic acid fluorescent probe. Compared to unconjugated oligo, we detected significantly more signal in cells treated with oligo-SEV, suggesting that cells actively interact with and uptake oligo-SEVs. Similar to results from qualitative imaging studies using fluorescently labeled SEV, oligo-SEVs were preferentially located with antigen-presenting cells in digested vaginal tissue samples. Oligonucleotide-based barcoding of EVs offers a novel method for quantitative, translatable, and microscope-free analysis of cellular EV uptake regardless of EV source and can be used in *in vitro*, *ex vivo*, and *in vivo* models.

5.3. Dual Quantum Dot and Oligobarcode Labeling to Probe Tissue Uptake and Transport of Brain Tissue-Derived Extracellular Vesicles

Nguyen, N. P., Schimek, N., Wu, E., Colwell, O., Vojtech, L., Nance, E.* *In preparation,* 2024.

*Corresponding author

Extracellular vesicles (EVs) have emerged as promising therapeutic agents in various neurological conditions due to their ability to modulate injury response, tissue repair, and inflammation. However, lack of detailed knowledge of EV tissue movement, localization, and fate limits the translation of EV-based therapeutics into the clinic. We employed a novel click chemistry approach to label and track brain tissue-derived EVs (BEVs) with quantum dots (QDs) and oligobarcodes, enabling qualitative and quantitative assessment of BEV behavior in brain tissue. Studies performed using EVs derived from tissue rather than cell culture are more representative of the physiological behavior of endogenous EVs, especially within complex tissue environments. We used a combination of confocal microscopy, multiple particle tracking (MPT), and quantitative PCR to track BEVs on short- and long- timescales. Our findings confirmed that BEVs associate with microglia in an *ex vivo* brain tissue model, with increased cellular association observed following oxygen-glucose deprivation (OGD) injury, particularly in the striatum. Trends in tracking BEV diffusion coefficients suggested regional changes in extracellular matrix integrity and cellular viability post-injury. Additionally, novel oligobarcode tagging allowed us to quantify the uptake of BEVs in brain tissue up to 48h post-application. Our results demonstrate the importance of considering the regional and pathological states of tissue in evaluating BEV localization and transport. Further

mechanistic studies on pathways governing BEV cellular uptake in the brain is necessary for advancing EV-based therapeutics for neurological disorders.

5.4. A Cross-Species Analysis of Microglial Morphology

Helmbrecht H., Lin T.J., **Nguyen, N.P.,** Schimek N. Onodera M., Correy K., Wood T., Svedin P., Mallard C., Chand K., Wixey J., Sah N., Kannan S., Nance E. "A Cross-Species Analysis of Microglial Morphology during Neurodevelopment." *In preparation.*

Neurodevelopmental diseases and injury have lasting impacts on neonates and their families, as even survivors experience heightened susceptibility for long-term cognitive and neurological disabilities.[5, 158] Due to the severity of the health outcomes, there is high clinical relevance to study the mechanisms of neurodevelopment and pathological disease states of the neonatal brain. In particular, microglia are the resident immune cells of the brain, and play a critical role in acute injury response, amelioration of inflammation, and sustained tissue repair following injury.[15, 18] In a healthy brain model, microglia regulate neuronal development, prune synapses, and clear debris and cell death from accumulating in the extracellular matrix.[159] As first-in-line responders to brain injury, microglia exhibit highly dynamic morphological shifts in response to changes to the environment, proteomics, and metabolomics.[81] Though microglia exhibit a spectrum of different phenotypes, they are classically categorized into two broad groups as "activated" vs. "resting" phenotypes. It is thought that "activated" microglia are characterized by an amoeboid and circular shape that is indicative of an inflammatory condition, whereas "resting" microglia display increased branching and reduced circularity that is indicative of anti-inflammatory processes.

Though it is known that microglia demonstrate heterogeneity in their shape in response to injury, the mechanism of this is still being investigated. It is also unknown

whether microglial phenotype changes across species. There are many different animal models that have been used to study neurological disease such as mice, rats, ferrets, and non-human primates. Due to the broad diversity of samples represented in literature it is important to capture the wide variety of microglial morphologies from multiple animal models. We are working on building a database of microglial images from tissues derived from different animal species (rat, mouse, ferret, pig, rabbit, and human) across both sexes. This database will be the largest neurodevelopmental microglial morphology database, to our knowledge and will help provide insights into biological factors that influence microglia morphology.

5.5. EXperimentalisT Interactive LEarning (TEXTILE)

Helmbrecht H., Schimek **N., Nguyen N.P.,** Nance E.* "Tutorials in EXperimentalisT Interactive LEarning (TEXTILE): Laboratory Educational Training as an Outreach Program for Research Careers." *In preparation.*

Chemical engineering core curricula involves introducing students to fundamental concepts such as thermodynamics and transport phenomena. Though chemical engineering courses introduce students to a variety of important concepts, student experiences in STEM education are greatly affected by their participation in undergraduate research.[160, 161] To encourage research accessibility to students and promote diversity in STEM, we developed a learning platform called Tutorials in EXperimentalisT Interactive LEarning (TEXTILE). TEXTILE consists of both a wetlab and drylab component, exposing students not only to data science methods, but also the wetlab experiments that were used to obtain the data used for data science analysis. TEXTILE is developed with laboratory-based learning and carries students through the pipeline of pairing wetlab techniques with data science analysis tools. It is

also developed as a module-based learning platform where students can skip modules or reorganize modules based on their learning level. When developing the TEXTILE modules, we focused on centering the course learning around specific topics explored in the Nance lab, such as microglia phenotype characterization and image analysis. In this way students can apply materials learned through the modules to real data collected from the lab. There were eleven developed modules for TEXTILE, and we launched our first TEXTILE learning cohort in summer 2022, and due to popular demand, offered the course again in summer 2023. We have also participated in the UW CoMotion Innovation workshop in an effort to expand TEXTILE's reach and accessibility.

Chapter 6. CURRICULUM VITAE

NAM PHUONG NGUYEN
Mobile: (503)-804-8142 | Email: npnguyen8@gmail.com

PROFESSIONAL SUMMARY

- Ph.D. graduate in Molecular Engineering and NIH translational science fellow with 7 years experience in leading, and executing research projects and protocols specializing on therapeutic platforms
- 10 years of experience in pre-clinical wetlab research, mentored 8 junior members, and worked on multidisciplinary and cross-functional teams across 6 departments
- Track record of active learning with resource management and scientific communication across broad audiences

SKILLS & COMPETANCIES

10 years of wetlab experience, aseptic technique, primary cell/tissue culturing, tissue handling, tissue processing and sectioning, rodent handling, polymerase chain reaction (PCR), digital PCR, immunohistochemistry, nanoparticle characterization, confocal microscopy, two-photon microscopy, live cell imaging, transmission electron microscopy (TEM), flow cytometry, fluorescence activated cell sorting (FACS), nanoparticle tracking analysis (NTA), RNA/DNA extraction, therapeutic dose-evaluations, exosome/protein extraction and purification, therapeutic controlled release studies, cell-based assays, size exclusion chromatography, primer design, quality control, scientific communication, good manufacturing practices, GraphPad Prism, data analysis, basic knowledge of Python for image analysis, statistical analysis for biomedical research

I. EDUCATION & TRAINING

Ph.D. Molecular Engineering and Sciences **September 2019-August 2024**
University of Washington, Seattle, WA
Research Advisor: Prof. Elizabeth Nance (Chemical Engineering)
Thesis: Brain-Derived Extracellular Vesicles as Therapeutic Vehicles and Molecular Probes in the Neonatal Brain

M.S. Materials Science & Engineering
University of Washington, Seattle, WA **September 2017-June 2019**
Research Advisors: Prof. Ying Zheng (Bioengineering) & Prof. Miqin Zhang (Materials Science)
Thesis: Designing a platform for control of collagen matrix anisotropy under a magnetic field with applications to vascular engineering and regenerative medicine

B.S. Materials Science & Engineering **September 2012-June 2017**

Stanford University, Stanford, CA
Research Advisors: Prof. Thomas Sudhof (Molecular/Cellular Physiology) & Prof. Sarah Heilshorn (Materials Science)

II. RESEARCH EXPERIENCE

Ph.D. Research Assistant, Advisor: Elizabeth Nance April 2020-August 2024
University of Washington, Dept. of Chemical Engineering
Thesis: Brain-derived extracellular vesicles (BEVs) as molecular probes and therapeutic vehicles in the neonatal brain

- Established EV isolation, purification, and characterization standard operating procedures in the Nance lab
- Determined significant BEV therapeutic effects on *ex vivo* neonatal models of hypoxia ischemia and impact on shifting microglia morphology from inflammatory to anti-inflammatory phenotypes
- Designed & deployed a novel quantum dot and oligonucleotide biobarcoding technology to track EV localization and cellular association

M.S. Research Assistant, Advisor: Ying Zheng November 2017-March 2019
University of Washington, Dept. of Bioengineering
Thesis: Designing a platform for control of collagen matrix anisotropy under a magnetic field with applications to vascular engineering and regenerative medicine

- Designed microfluidic platform to analyze cellular organization under a magnetic field
- Constructed collagen matrix molds to characterize and establish collagen fiber alignment

M.S. Research Assistant, Advisor: Fumio Ohuchi June 2018-June 2019
University of Washington, Dept. of Materials Science
Applied machine learning to create and publish data visualizations of material structural-property relationships

- Applied machine learning to hundreds of unique materials from the Granta materials database to determine trends in materials properties
- Established the use of self-organizing mapping as an effective educational tool for materials science students and trend recognition in material properties

Undergraduate Researcher, Advisor: Thomas Sudhof March 2014-October 2016
Stanford University, Dept. of Molecular and Cellular Physiology

- Independently performed behavioral and quantitative assays/techniques (immunohistochemistry, western blotting, confocal imaging, protein isolation) with murine models analyzing synaptic organization and regulation
- Performed neonatal murine brain dissections and animal husbandry

III. PUBLICATIONS

- **Nguyen, N.P.**; Helmbrecht, H.; Ye, Z.; Adebayo, T.; Hashi, N.; Doan, M.-A.; Nance, E. Brain Tissue-Derived Extracellular Vesicle Mediated Therapy in the Neonatal Ischemic Brain. *Int. J. Mol. Sci.,* (**2022**), DOI: 10.3390/ijms23020620
- **Nguyen, N**.**P**., Qian,J., Oya, Y., Kikugawa, G., Okabe, T.,Huang, Y., & Ohuchi, F. Introducing Self-Organized Maps (SOM) as a Tool for Materials Research and Education, *Results in Materials,* **(2019)**, DOI: 10.1016/j.rinma.2019.100020
- Ludwig, C., Shan, M., **Nguyen, N.P.,** and Lam, C., The Future of Automated Mobile Eye Diagnosis, *Journal of Mobile Technology in Medicine*, Vol.5, **(2016),** DOI: 10.7309/jmtm.5.2.7

IV. PROVISIONAL PATENTS

Nguyen, Nam Phuong, Paktinat, S., Vojtech, L., Nance, E. 2023. Oligomer Barcode for Labeling Extracellular Vesicles. U.S. Patent 63/594,885, filed October 31, 2023. Provisional patent.

V. INDUSTRY EXPERIENCE

Materials Engineering Internship, December 2014-June 2015
Koli Inc., Fremont, CA

- Developed material analyses on a novel device, implemented design iteration, and prepared testing protocols
- Established biocompatibility testing and manufacturing protocols for device currently in clinical trials

Design Engineering Internship, January 2013-June 2013
Stanford University, Stanford, CA

- Implemented design of novel baby carrier targeted to paraplegic parents
- Manufactured and tested multiple iterations of device
- Showcased product at Stanford Design School Symposium

VI. AWARDS, CONFERENCES, AND PROFESSIONAL SOCIETIES

AWARDS

2024: UW Women Engineers Rise Outstanding Scholar

2023: UW CoMotion Young Innovator Showcase Invitee

2023: NIH Institute of Translational Health Sciences TL1 Graduate Fellowship

2023: National Society of Women Engineers (SWE) Best Graduate Research Award

2022: UW Chemical Engineering Graduate Student Symposium Best Poster Award

2022: Controlled Release Society Nervous System Delivery Trainee Award

2022: Molecular Engineering & Sciences Outstanding Service Award

2022: UW Graduate & Professional Student Senate Travel Grant Award Winner

2019: Recipient of UW College of Engineering Dean's Fellowship in Materials Science

2015: Order of Omega Women in Leadership Award

2013: BioX Fellowship Recipient, Department of Biology, Judith Frydman Lab

CONFERENCES

Platform/Plenary Talks

1. "Novel oligonucleotide biobarcode tagging of extracellular vesicles (EVs)," *2024 Institute of Translational Health Sciences Expo,* Seattle, WA (May 2024)
2. "Brain-Derived Extracellular Vesicles: Molecular Probes and Therapeutic Vehicles in the Neonatal Ischemic Brain," *Biomedical Engineering Society Annual Conference,* Seattle, WA (Oct. 2023)
3. "Biological Nanoparticle Therapeutics in the Brain", *Society of Women Engineers Annual Conference,* Seattle, WA (March 2023)
4. "Brain-Derived Extracellular Vesicles: Molecular Probes and Therapeutic Vehicles in the Neonatal Ischemic Brain", *American Institute of Chemical Engineers Annual Conference,* Phoenix, AZ (November 2022)
5. **"**Brain-Derived Extracellular Vesicles: Molecular Probes and Therapeutic Vehicles in the Neonatal Ischemic Brain", *Controlled Release Society Annual Conference*, Montreal, Canada (July. 2022)

Poster Presentations

1. "Novel oligonucleotide (oligo) barcode tagging of semen-derived extracellular vesicles (SEV)," *International Society of Extracellular Vesicles Annual Conference,* Seattle, WA (May 2023)
2. "Brain-Derived Extracellular Vesicles: Molecular Probes and Therapeutic Vehicles in the Neonatal Ischemic Brain," *15th Annual Chemical Engineering Graduate Student Symposium*, University of Washington (Oct. 2022)
3. "Brain Tissue-Derived Extracellular Vesicle Mediated Therapy in the Neonatal Ischemic Brain", *13th Hershey Conference on Developmental Brain Injury*, Union, WA (May. 2022)
4. "The Role of TRiC in Molecular Biology", *Undergraduate BioX Research Symposium,* Stanford University, Stanford, CA (Aug. 2013)

INVITED SEMINARS

1. "Novel Oligonucleotide Biobarcoding of Extracellular Vesicles," *UW CoMotion Innovator Showcase* (Nov. 2023)
2. "Biological Nanoparticle Therapeutics in the Brain," *NW Science Writers Association* (Sep. 2022)
3. "Investigating the Therapeutic Potential of Brain-Derived Extracellular Vesicles in

Neonatal Ischemia Models," *Bioengineering Seminar Series,* University of Washington (Apr. 2022)
4. "Self-Organized Maps (SOM) as a Tool for Materials Education", *Data Science in Materials Science*, Inst. of Fluid Sciences, Tohoku University, Japan (Mar. 2019)

PROFESSIONAL SOCIETIES

- DEI (Diversity, Equity, Inclusivity) Committee Deputy Chair, Controlled Release Society (2021-2023)
- Director, Society of Women Engineers, UW Graduate Chapter (2020-2023)
- Graduate member, International Society of Extracellular Vesicles (2023-2024)
- Graduate member, American Institute of Chemical Engineers (2022-2023)

VII. SCIENCE OUTREACH AND LEADERSHIP

Science Communicator, A Tale of Two PhDs Blog March 2020-present
Website: ataleoftwophds.com/Instagram: @tale_of_2_phds

- Created a science blog to educate readers on my research, graduate school, and IDEA (inclusivity, diversity, equality, anti-racism) in STEM
- Currently developing a podcast featuring grad students and faculty members to showcase research across different fields

Director of GradSWE, Society of Women Engineers (SWE) at UW
June 2021-June 2023
University of Washington

- Acted as the representative and liaison between the graduate and undergraduate SWE chapters
- Led a team of 16 officers in organizing and providing resources to engineering graduate community
- Grew the GradSWE leadership team by 300% over the first year as being Director and successfully established formal committee branches

Outreach Subcommittee Chair, Graduate Student Association
September 2020-September 2023
University of Washington

- Spearheaded the organization of the first diversity committee in Molecular Engineering
- Established and moderated Molecular Engineering town halls, outreach events, and community development events
- Organized and moderated a new best practices research mentorship training workshop for graduate students

Instructor, UW Math Science Upward Bound Program July 2019-August 2022
University of Washington

- Two summers instructing low-income and underrepresented high school students in the greater Seattle area preparing for college
- Taught more than 80 students research skills and introductory engineering principles, culminating in a research project presented at a symposium every year

VIII. MENTEES & RESEARCH TRAINEES

- 2020-2022: Ziming (Jimmy)Ye, 2021 B.S. Chemical Engineering, University of Washington
- 2020- 2023: Tolu Adebayo, 2023 B.S. Biology, University of Washington, *ALVA Scholar*
- 2021-2023: Ana Sigler, 2023 B.S. Bioengineering, University of Washington
- 2021- 2023: Najma Hashi, 2023 B.S. Chemical Engineering, University of Washington
- 2021-2022: Daria Gileva, 2024 B.S. Bioengineering, University of Washington
- 2022-2023: Norah Alhindi, 2023 B.S. Biochemistry, University of Washington
- 2022- 2024: Eleanor Wu, 2025 B.S. Bioengineering, University of Washington, *Mary Gates Scholar*
- 2023-2024: Olivia Colwell, 2025 B.S. Bioengineering, University of Washington, *Mary Gates Scholar*

IX. SERVICE

2023: Graduate Society of Women Engineers: Boeing & Bristol Myers Squibb Sponsored Professional Networking Happy Hour, *Organizer*

2023: Molecular Engineering & Sciences Graduate Student Association: Research Mentorship Best Practices, *Panelist*

2022: Molecular Engineering & Sciences Graduate Student Association: Introduction to Undergraduate Research, *Moderator*

2022: Department of Chemical Engineering, Distinguished Young Scholars Seminar, *Graduate Reviewer*

2022: Molecular Engineering & Sciences 5-Year Review Committee, *Graduate Student Representative*

2022: UW Women's Center Making Connections High School Program, *Event Organizer & Invited Panelist*

2022: Controlled Release Society Young Scientist Committee Meeting, *Invited Speaker*

2022: Controlled Release Society Focus Group Chair Orientation, *Invited Speaker*

2022, 2021: Molecular Engineering & Sciences DEI Committee Undergraduate Research Panel, *Invited Panelist & Event Organizer*

2022, 2011: Society of Women Engineers Professional Careers Panel, *Event Organizer*

2022: Society of Women Engineers High School Leadership Summit, *Event Organizer*

2022, 2021: Reddit AMA for Molecular Engineering, *Event Organizer & Panelist*

2021: Molecular Engineering & Sciences DEI Committee "STEM Grad School 101", *Event Organizer & Panelist*

2021: Undergraduate Research Panel Workshop on Best Practices in Mentorship, *Event Organizer & Panelist*

2021: Molecular Engineering & Sciences DEI Committee Mentorship Program, *Graduate Mentor*

2021, 2020: Society of Women Engineers Resume and Career Building Workshop, *Event Organizer*

2020: Society of Women Engineers Negotiations Workshop, *Event Organizer*

Journals Reviewed
Nature Nanotechnology
Journal of Controlled Release

BIBLIOGRAPHY

1. Ferriero DM. Neonatal Brain Injury. New England Journal of Medicine. 2004;351(19):1985-95. doi: 10.1056/NEJMra041996.
2. Davidson J, Davies A, Wassink G, Bennet L, Gunn A. Can we further optimize therapeutic hypothermia for hypoxic-ischemic encephalopathy? Neural Regeneration Research. 2019;14(10):1678. doi: 10.4103/1673-5374.257512.
3. Kurinczuk JJ, White-Koning M, Badawi N. Epidemiology of neonatal encephalopathy and hypoxic-ischaemic encephalopathy. Early Hum Dev. 2010;86(6):329-38. Epub 2010/06/18. doi: 10.1016/j.earlhumdev.2010.05.010. PubMed PMID: 20554402.
4. Douglas-Escobar M, Weiss MD. Hypoxic-Ischemic Encephalopathy. JAMA Pediatrics. 2015;169(4):397. doi: 10.1001/jamapediatrics.2014.3269.
5. Millar LJ, Shi L, Hoerder-Suabedissen A, Molnár Z. Neonatal Hypoxia Ischaemia: Mechanisms, Models, and Therapeutic Challenges. Frontiers in Cellular Neuroscience. 2017;11. doi: 10.3389/fncel.2017.00078.
6. Jacobs S, Hunt R, Tarnow-Mordi W, Inder T, Davis P. Cooling for newborns with hypoxic ischaemic encephalopathy. Cochrane Database Syst Rev. 2007(4):CD003311. Epub 2007/10/19. doi: 10.1002/14651858.CD003311.pub2. PubMed PMID: 17943788.
7. Shankaran S, Laptook AR, Pappas A, Mcdonald SA, Das A, Tyson JE, Poindexter BB, Schibler K, Bell EF, Heyne RJ, Pedroza C, Bara R, Van Meurs KP, Huitema CMP, Grisby C, Devaskar U, Ehrenkranz RA, Harmon HM, Chalak LF, Demauro SB, Garg M, Hartley-Mcandrew ME, Khan AM, Walsh MC, Ambalavanan N, Brumbaugh JE, Watterberg KL, Shepherd EG, Hamrick SEG, Barks J, Cotten CM, Kilbride HW, Higgins RD. Effect of Depth and Duration of Cooling on Death or Disability at Age 18 Months Among Neonates With Hypoxic-Ischemic Encephalopathy. JAMA. 2017;318(1):57. doi: 10.1001/jama.2017.7218.
8. Wood TR, Gundersen JK, Falck M, Maes E, Osredkar D, Løberg EM, Sabir H, Walløe L, Thoresen M. Variability and sex-dependence of hypothermic neuroprotection in a rat model of neonatal hypoxic–ischaemic brain injury: a single laboratory meta-analysis. Scientific Reports. 2020;10(1). doi: 10.1038/s41598-020-67532-2.
9. Wood T, Osredkar D, Puchades M, Maes E, Falck M, Flatebø T, Walløe L, Sabir H, Thoresen M. Treatment temperature and insult severity influence the neuroprotective effects of therapeutic hypothermia. Scientific Reports. 2016;6(1):23430. doi: 10.1038/srep23430.
10. Liao R, Wood TR, Nance E. Nanotherapeutic modulation of excitotoxicity and oxidative stress in acute brain injury. Nanobiomedicine. 2020;7:1849543520970819. doi: 10.1177/1849543520970819.
11. Liao R, Wood TR, Nance E. Superoxide dismutase reduces monosodium glutamate-induced injury in an organotypic whole hemisphere brain slice model of excitotoxicity. Journal of Biological Engineering. 2020;14(1). doi: 10.1186/s13036-020-0226-8.

12. Liao R, Wood TR, Nance E. Nanotherapeutic modulation of excitotoxicity and oxidative stress in acute brain injury. Nanobiomedicine. 2020;7:184954352097081. doi: 10.1177/1849543520970819.
13. Xia W, Han J, Huang G, Ying W. Inflammation in ischaemic brain injury: Current advances and future perspectives. Clinical and Experimental Pharmacology and Physiology. 2010;37(2):253-8. doi: 10.1111/j.1440-1681.2009.05279.x.
14. McKee CA, Lukens JR. Emerging Roles for the Immune System in Traumatic Brain Injury. Frontiers in Immunology. 2016;7. doi: 10.3389/fimmu.2016.00556.
15. Benakis C, Garcia-Bonilla L, Iadecola C, Anrather J. The role of microglia and myeloid immune cells in acute cerebral ischemia. Frontiers in Cellular Neuroscience. 2015;8. doi: 10.3389/fncel.2014.00461.
16. Li B, Dasgupta C, Huang L, Meng X, Zhang L. MiRNA-210 induces microglial activation and regulates microglia-mediated neuroinflammation in neonatal hypoxic-ischemic encephalopathy. Cellular & Molecular Immunology. 2020;17(9):976-91. doi: 10.1038/s41423-019-0257-6.
17. McRae A, Gilland E, Bona E, Hagberg H. Microglia activation after neonatal hypoxic-ischemia. Brain Res Dev Brain Res. 1995;84(2):245-52. doi: 10.1016/0165-3806(94)00177-2. PubMed PMID: 7743644.
18. Weinstein JR, Koerner IP, Möller T. Microglia in ischemic brain injury. Future Neurology. 2010;5(2):227-46. doi: 10.2217/fnl.10.1.
19. Tsuji S, Di Martino E, Mukai T, Tsuji S, Murakami T, Harris RA, Blomgren K, Åden U. Aggravated brain injury after neonatal hypoxic ischemia in microglia-depleted mice. Journal of Neuroinflammation. 2020;17(1). doi: 10.1186/s12974-020-01792-7.
20. Serdar M, Kempe K, Rizazad M, Herz J, Bendix I, Felderhoff-Muser U, Sabir H. Early Pro-inflammatory Microglia Activation After Inflammation-Sensitized Hypoxic-Ischemic Brain Injury in Neonatal Rats. Front Cell Neurosci. 2019;13:237. Epub 20190524. doi: 10.3389/fncel.2019.00237. PubMed PMID: 31178702; PMCID: PMC6543767.
21. Paolicelli RC, Sierra A, Stevens B, Tremblay ME, Aguzzi A, Ajami B, Amit I, Audinat E, Bechmann I, Bennett M, Bennett F, Bessis A, Biber K, Bilbo S, Blurton-Jones M, Boddeke E, Brites D, Brone B, Brown GC, Butovsky O, Carson MJ, Castellano B, Colonna M, Cowley SA, Cunningham C, Davalos D, De Jager PL, de Strooper B, Denes A, Eggen BJL, Eyo U, Galea E, Garel S, Ginhoux F, Glass CK, Gokce O, Gomez-Nicola D, Gonzalez B, Gordon S, Graeber MB, Greenhalgh AD, Gressens P, Greter M, Gutmann DH, Haass C, Heneka MT, Heppner FL, Hong S, Hume DA, Jung S, Kettenmann H, Kipnis J, Koyama R, Lemke G, Lynch M, Majewska A, Malcangio M, Malm T, Mancuso R, Masuda T, Matteoli M, McColl BW, Miron VE, Molofsky AV, Monje M, Mracsko E, Nadjar A, Neher JJ, Neniskyte U, Neumann H, Noda M, Peng B, Peri F, Perry VH, Popovich PG, Pridans C, Priller J, Prinz M, Ragozzino D, Ransohoff RM, Salter MW, Schaefer A, Schafer DP, Schwartz M, Simons M, Smith CJ, Streit WJ, Tay TL, Tsai LH, Verkhratsky A, von Bernhardi R, Wake H, Wittamer V, Wolf SA, Wu LJ, Wyss-Coray T. Microglia states and nomenclature: A field at its crossroads. Neuron. 2022;110(21):3458-83. doi: 10.1016/j.neuron.2022.10.020. PubMed PMID: 36327895; PMCID: PMC9999291.
22. Kim Y, Park J, Choi YK. The Role of Astrocytes in the Central Nervous System Focused on BK Channel and Heme Oxygenase Metabolites: A Review. Antioxidants. 2019;8(5):121. doi: 10.3390/antiox8050121.
23. Liddelow SA, Barres BA. Reactive Astrocytes: Production, Function, and Therapeutic Potential. Immunity. 2017;46(6):957-67. doi: 10.1016/j.immuni.2017.06.006.
24. El Andaloussi S, Mäger I, Breakefield XO, Wood MJA. Extracellular vesicles: biology and emerging therapeutic opportunities. Nature Reviews Drug Discovery. 2013;12(5):347-57. doi: 10.1038/nrd3978.

25. Holm MM, Kaiser J, Schwab ME. Extracellular Vesicles: Multimodal Envoys in Neural Maintenance and Repair. Trends in Neurosciences. 2018;41(6):360-72. doi: 10.1016/j.tins.2018.03.006.
26. Turturici G, Tinnirello R, Sconzo G, Geraci F. Extracellular membrane vesicles as a mechanism of cell-to-cell communication: advantages and disadvantages. American Journal of Physiology-Cell Physiology. 2014;306(7):C621-C33. doi: 10.1152/ajpcell.00228.2013.
27. Welsh JA, Goberdhan DCI, O'Driscoll L, Buzas EI, Blenkiron C, Bussolati B, Cai H, Di Vizio D, Driedonks TAP, Erdbrugger U, Falcon-Perez JM, Fu QL, Hill AF, Lenassi M, Lim SK, Mahoney MG, Mohanty S, Moller A, Nieuwland R, Ochiya T, Sahoo S, Torrecilhas AC, Zheng L, Zijlstra A, Abuelreich S, Bagabas R, Bergese P, Bridges EM, Brucale M, Burger D, Carney RP, Cocucci E, Crescitelli R, Hanser E, Harris AL, Haughey NJ, Hendrix A, Ivanov AR, Jovanovic-Talisman T, Kruh-Garcia NA, Ku'ulei-Lyn Faustino V, Kyburz D, Lasser C, Lennon KM, Lotvall J, Maddox AL, Martens-Uzunova ES, Mizenko RR, Newman LA, Ridolfi A, Rohde E, Rojalin T, Rowland A, Saftics A, Sandau US, Saugstad JA, Shekari F, Swift S, Ter-Ovanesyan D, Tosar JP, Useckaite Z, Valle F, Varga Z, van der Pol E, van Herwijnen MJC, Wauben MHM, Wehman AM, Williams S, Zendrini A, Zimmerman AJ, Consortium M, Thery C, Witwer KW. Minimal information for studies of extracellular vesicles (MISEV2023): From basic to advanced approaches. J Extracell Vesicles. 2024;13(2):e12404. doi: 10.1002/jev2.12404. PubMed PMID: 38326288; PMCID: PMC10850029.
28. Gandham S, Su X, Wood J, Nocera AL, Alli SC, Milane L, Zimmerman A, Amiji M, Ivanov AR. Technologies and Standardization in Research on Extracellular Vesicles. Trends in Biotechnology. 2020;38(10):1066-98. doi: 10.1016/j.tibtech.2020.05.012.
29. Théry C, Witwer KW, Aikawa E, Alcaraz MJ, Anderson JD, Andriantsitohaina R, Antoniou A, Arab T, Archer F, Atkin-Smith GK, Ayre DC, Bach J-M, Bachurski D, Baharvand H, Balaj L, Baldacchino S, Bauer NN, Baxter AA, Bebawy M, Beckham C, Bedina Zavec A, Benmoussa A, Berardi AC, Bergese P, Bielska E, Blenkiron C, Bobis-Wozowicz S, Boilard E, Boireau W, Bongiovanni A, Borràs FE, Bosch S, Boulanger CM, Breakefield X, Breglio AM, Brennan MÁ, Brigstock DR, Brisson A, Broekman ML, Bromberg JF, Bryl-Górecka P, Buch S, Buck AH, Burger D, Busatto S, Buschmann D, Bussolati B, Buzás EI, Byrd JB, Camussi G, Carter DR, Caruso S, Chamley LW, Chang Y-T, Chen C, Chen S, Cheng L, Chin AR, Clayton A, Clerici SP, Cocks A, Cocucci E, Coffey RJ, Cordeiro-Da-Silva A, Couch Y, Coumans FA, Coyle B, Crescitelli R, Criado MF, D'Souza-Schorey C, Das S, Datta Chaudhuri A, De Candia P, De Santana EF, De Wever O, Del Portillo HA, Demaret T, Deville S, Devitt A, Dhondt B, Di Vizio D, Dieterich LC, Dolo V, Dominguez Rubio AP, Dominici M, Dourado MR, Driedonks TA, Duarte FV, Duncan HM, Eichenberger RM, Ekström K, El Andaloussi S, Elie-Caille C, Erdbrügger U, Falcón-Pérez JM, Fatima F, Fish JE, Flores-Bellver M, Försönits A, Frelet-Barrand A, Fricke F, Fuhrmann G, Gabrielsson S, Gámez-Valero A, Gardiner C, Gärtner K, Gaudin R, Gho YS, Giebel B, Gilbert C, Gimona M, Giusti I, Goberdhan DC, Görgens A, Gorski SM, Greening DW, Gross JC, Gualerzi A, Gupta GN, Gustafson D, Handberg A, Haraszti RA, Harrison P, Hegyesi H, Hendrix A, Hill AF, Hochberg FH, Hoffmann KF, Holder B, Holthofer H, Hosseinkhani B, Hu G, Huang Y, Huber V, Hunt S, Ibrahim AG-E, Ikezu T, Inal JM, Isin M, Ivanova A, Jackson HK, Jacobsen S, Jay SM, Jayachandran M, Jenster G, Jiang L, Johnson SM, Jones JC, Jong A, Jovanovic-Talisman T, Jung S, Kalluri R, Kano S-I, Kaur S, Kawamura Y, Keller ET, Khamari D, Khomyakova E, Khvorova A, Kierulf P, Kim KP, Kislinger T, Klingeborn M, Klinke DJ, Kornek M, Kosanović MM, Kovács ÁF, Krämer-Albers E-M, Krasemann S, Krause M, Kurochkin IV, Kusuma GD, Kuypers S, Laitinen S, Langevin SM, Languino LR, Lannigan J, Lässer C, Laurent LC, Lavieu G, Lázaro-Ibáñez E, Le Lay S, Lee M-S, Lee YXF, Lemos DS, Lenassi M, Leszczynska A, Li IT, Liao K, Libregts SF, Ligeti E, Lim R, Lim SK, Linē A, Linnemannstöns K, Llorente A, Lombard CA, Lorenowicz MJ, Lörincz ÁM, Lötvall J, Lovett J, Lowry MC, Loyer X, Lu Q, Lukomska B, Lunavat TR, Maas SL, Malhi H, Marcilla A, Mariani J, Mariscal J, Martens-Uzunova ES, Martin-Jaular L, Martinez MC, Martins VR, Mathieu M, Mathivanan S, Maugeri M,

Mcginnis LK, Mcvey MJ, Meckes DG, Meehan KL, Mertens I, Minciacchi VR, Möller A, Møller Jørgensen M, Morales-Kastresana A, Morhayim J, Mullier F, Muraca M, Musante L, Mussack V, Muth DC, Myburgh KH, Najrana T, Nawaz M, Nazarenko I, Nejsum P, Neri C, Neri T, Nieuwland R, Nimrichter L, Nolan JP, Nolte-'T Hoen EN, Noren Hooten N, O'Driscoll L, O'Grady T, O'Loghlen A, Ochiya T, Olivier M, Ortiz A, Ortiz LA, Osteikoetxea X, Østergaard O, Ostrowski M, Park J, Pegtel DM, Peinado H, Perut F, Pfaffl MW, Phinney DG, Pieters BC, Pink RC, Pisetsky DS, Pogge Von Strandmann E, Polakovicova I, Poon IK, Powell BH, Prada I, Pulliam L, Quesenberry P, Radeghieri A, Raffai RL, Raimondo S, Rak J, Ramirez MI, Raposo G, Rayyan MS, Regev-Rudzki N, Ricklefs FL, Robbins PD, Roberts DD, Rodrigues SC, Rohde E, Rome S, Rouschop KM, Rughetti A, Russell AE, Saá P, Sahoo S, Salas-Huenuleo E, Sánchez C, Saugstad JA, Saul MJ, Schiffelers RM, Schneider R, Schøyen TH, Scott A, Shahaj E, Sharma S, Shatnyeva O, Shekari F, Shelke GV, Shetty AK, Shiba K, Siljander PR-M, Silva AM, Skowronek A, Snyder OL, Soares RP, Sódar BW, Soekmadji C, Sotillo J, Stahl PD, Stoorvogel W, Stott SL, Strasser EF, Swift S, Tahara H, Tewari M, Timms K, Tiwari S, Tixeira R, Tkach M, Toh WS, Tomasini R, Torrecilhas AC, Tosar JP, Toxavidis V, Urbanelli L, Vader P, Van Balkom BW, Van Der Grein SG, Van Deun J, Van Herwijnen MJ, Van Keuren-Jensen K, Van Niel G, Van Royen ME, Van Wijnen AJ, Vasconcelos MH, Vechetti IJ, Veit TD, Vella LJ, Velot É, Verweij FJ, Vestad B, Viñas JL, Visnovitz T, Vukman KV, Wahlgren J, Watson DC, Wauben MH, Weaver A, Webber JP, Weber V, Wehman AM, Weiss DJ, Welsh JA, Wendt S, Wheelock AM, Wiener Z, Witte L, Wolfram J, Xagorari A, Xander P, Xu J, Yan X, Yáñez-Mó M, Yin H, Yuana Y, Zappulli V, Zarubova J, Žėkas V, Zhang J-Y, Zhao Z, Zheng L, Zheutlin AR, Zickler AM, Zimmermann P, Zivkovic AM, Zocco D, Zuba-Surma EK. Minimal information for studies of extracellular vesicles 2018 (MISEV2018): a position statement of the International Society for Extracellular Vesicles and update of the MISEV2014 guidelines. Journal of Extracellular Vesicles. 2018;7(1):1535750. doi: 10.1080/20013078.2018.1535750.

30. Henne M, William, Buchkovich J, Nicholas, Emr D, Scott. The ESCRT Pathway. Developmental Cell. 2011;21(1):77-91. doi: 10.1016/j.devcel.2011.05.015.

31. Wood MJA, O'Loughlin AJ, Lakhal S. Exosomes and the blood–brain barrier: implications for neurological diseases. Therapeutic Delivery. 2011;2(9):1095-9. doi: 10.4155/tde.11.83.

32. Budnik V, Ruiz-Cañada C, Wendler F. Extracellular vesicles round off communication in the nervous system. Nature Reviews Neuroscience. 2016;17(3):160-72. doi: 10.1038/nrn.2015.29.

33. Brenna S, Krisp C, Altmeppen HC, Magnus T, Puig B. Brain-Derived Extracellular Vesicles in Health and Disease: A Methodological Perspective. International Journal of Molecular Sciences. 2021;22(3):1365. doi: 10.3390/ijms22031365.

34. Zheng M, Huang M, Ma X, Chen H, Gao X. Harnessing Exosomes for the Development of Brain Drug Delivery Systems. Bioconjugate Chemistry. 2019;30(4):994-1005. doi: 10.1021/acs.bioconjchem.9b00085.

35. Saint-Pol J, Gosselet F, Duban-Deweer S, Pottiez G, Karamanos Y. Targeting and Crossing the Blood-Brain Barrier with Extracellular Vesicles. Cells. 2020;9(4):851. doi: 10.3390/cells9040851.

36. Huang Y, Arab T, Russell AE, Mallick ER, Nagaraj R, Gizzie E, Redding-Ochoa J, Troncoso JC, Pletnikova O, Turchinovich A, Routenberg DA, Witwer KW. Towards a human brain EV atlas: Characteristics of EVs from different brain regions, including small RNA and protein profiles. 2023.

37. You Y, Muraoka S, Jedrychowski MP, Hu J, Mcquade AK, Young-Pearse T, Aslebagh R, Shaffer SA, Gygi SP, Blurton-Jones M, Poon WW, Ikezu T. Human neural cell type-specific extracellular vesicle proteome defines disease-related molecules associated with activated astrocytes in Alzheimer's disease brain. Journal of Extracellular Vesicles. 2022;11(1). doi: 10.1002/jev2.12183.

38. Brenna S, Altmeppen HC, Mohammadi B, Rissiek B, Schlink F, Ludewig P, Krisp C, Schluter H, Failla AV, Schneider C, Glatzel M, Puig B, Magnus T. Characterization of brain-derived extracellular vesicles reveals changes in cellular origin after stroke and enrichment of the prion protein with a potential role in cellular uptake. J Extracell Vesicles. 2020;9(1):1809065. Epub 20200827. doi: 10.1080/20013078.2020.1809065. PubMed PMID: 32944194; PMCID: PMC7480459.
39. Fan Y, Chen Z, Zhang M. Role of exosomes in the pathogenesis, diagnosis, and treatment of central nervous system diseases. J Transl Med. 2022;20(1):291. Epub 20220627. doi: 10.1186/s12967-022-03493-6. PubMed PMID: 35761337; PMCID: PMC9235237.
40. Fowler CD. NeuroEVs: Characterizing Extracellular Vesicles Generated in the Neural Domain. The Journal of Neuroscience. 2019;39(47):9262-8. doi: 10.1523/jneurosci.0146-18.2019.
41. You Y, Borgmann K, Edara VV, Stacy S, Ghorpade A, Ikezu T. Activated human astrocyte-derived extracellular vesicles modulate neuronal uptake, differentiation and firing. Journal of Extracellular Vesicles. 2020;9(1):1706801. doi: 10.1080/20013078.2019.1706801.
42. Guitart K, Loers G, Buck F, Bork U, Schachner M, Kleene R. Improvement of neuronal cell survival by astrocyte-derived exosomes under hypoxic and ischemic conditions depends on prion protein. Glia. 2016;64(6):896-910.
43. Vingtdeux V, Hamdane M, Loyens A, Gele P, Drobeck H, Begard S, Galas MC, Delacourte A, Beauvillain JC, Buee L, Sergeant N. Alkalizing drugs induce accumulation of amyloid precursor protein by-products in luminal vesicles of multivesicular bodies. J Biol Chem. 2007;282(25):18197-205. Epub 20070427. doi: 10.1074/jbc.M609475200. PubMed PMID: 17468104.
44. Saadatpour L, Fadaee E, Fadaei S, Nassiri Mansour R, Mohammadi M, Mousavi SM, Goodarzi M, Verdi J, Mirzaei H. Glioblastoma: exosome and microRNA as novel diagnosis biomarkers. Cancer Gene Ther. 2016;23(12):415-8. Epub 20161111. doi: 10.1038/cgt.2016.48. PubMed PMID: 27834360.
45. Kumar A, Stoica BA, Loane DJ, Yang M, Abulwerdi G, Khan N, Kumar A, Thom SR, Faden AI. Microglial-derived microparticles mediate neuroinflammation after traumatic brain injury. Journal of Neuroinflammation. 2017;14(1). doi: 10.1186/s12974-017-0819-4.
46. Dickens AM, Tovar-y-Romo LB, Yoo S-W, Trout AL, Bae M, Kanmogne M, Megra B, Williams DW, Witwer KW, Gacias M, Tabatadze N, Cole RN, Casaccia P, Berman JW, Anthony DC, Haughey NJ. Astrocyte-shed extracellular vesicles regulate the peripheral leukocyte response to inflammatory brain lesions. Science Signaling. 2017;10(473):eaai7696. doi: 10.1126/scisignal.aai7696.
47. Lenzini S, Bargi R, Chung G, Shin J-W. Matrix mechanics and water permeation regulate extracellular vesicle transport. Nature Nanotechnology. 2020;15(3):217-23. doi: 10.1038/s41565-020-0636-2.
48. Chivet M, Javalet C, Laulagnier K, Blot B, Hemming FJ, Sadoul R. Exosomes secreted by cortical neurons upon glutamatergic synapse activation specifically interact with neurons. J Extracell Vesicles. 2014;3:24722. Epub 20141113. doi: 10.3402/jev.v3.24722. PubMed PMID: 25398455; PMCID: PMC4232649.
49. Brenna S, Altmeppen HC, Mohammadi B, Rissiek B, Schlink F, Ludewig P, Krisp C, Schlüter H, Failla AV, Schneider C, Glatzel M, Puig B, Magnus T. Characterization of brain-derived extracellular vesicles reveals changes in cellular origin after stroke and enrichment of the prion protein with a potential role in cellular uptake. Journal of Extracellular Vesicles. 2020;9(1):1809065. doi: 10.1080/20013078.2020.1809065.
50. Bianco F, Perrotta C, Novellino L, Francolini M, Riganti L, Menna E, Saglietti L, Schuchman EH, Furlan R, Clementi E, Matteoli M, Verderio C. Acid sphingomyelinase activity triggers microparticle release from glial cells. EMBO J. 2009;28(8):1043-54. Epub 20090319. doi: 10.1038/emboj.2009.45. PubMed PMID: 19300439; PMCID: PMC2664656.

51. Xie R, Zeng X, Yan H, Huang X, Deng C. Effects and Mechanisms of Exosomes from Different Sources in Cerebral Ischemia. Cells. 2022;11(22). Epub 20221115. doi: 10.3390/cells11223623. PubMed PMID: 36429051; PMCID: PMC9688936.
52. Otero-Ortega L, Laso-García F, Frutos MCG-D, Diekhorst L, Martínez-Arroyo A, Alonso-López E, García-Bermejo ML, Rodríguez-Serrano M, Arrúe-Gonzalo M, Díez-Tejedor E, Fuentes B, Gutiérrez-Fernández M. Low dose of extracellular vesicles identified that promote recovery after ischemic stroke. Stem Cell Research & Therapy. 2020;11(1). doi: 10.1186/s13287-020-01601-1.
53. Zhang Y, Chopp M, Meng Y, Katakowski M, Xin H, Mahmood A, Xiong Y. Effect of exosomes derived from multipluripotent mesenchymal stromal cells on functional recovery and neurovascular plasticity in rats after traumatic brain injury. Journal of neurosurgery. 2015;122(4):856-67. doi: 10.3171/2014.11.JNS14770.
54. Deng M, Xiao H, Peng H, Yuan H, Xu Y, Zhang G, Tang J, Hu Z. Preservation of neuronal functions by exosomes derived from different human neural cell types under ischemic conditions. European Journal of Neuroscience. 2018;47(2):150-7. doi: 10.1111/ejn.13784.
55. Xin D, Li T, Chu X, Ke H, Liu D, Wang Z. MSCs-extracellular vesicles attenuated neuroinflammation, synapse damage and microglial phagocytosis after hypoxia-ischemia injury by preventing osteopontin expression. Pharmacological Research. 2021;164:105322. doi: 10.1016/j.phrs.2020.105322.
56. Du L, Jiang Y, Sun Y. Astrocyte-derived exosomes carry microRNA-17-5p to protect neonatal rats from hypoxic-ischemic brain damage via inhibiting BNIP-2 expression. NeuroToxicology. 2021;83:28-39. doi: 10.1016/j.neuro.2020.12.006.
57. Song Y, Li Z, He T, Qu M, Jiang L, Li W, Shi X, Pan J, Zhang L, Wang Y, Zhang Z, Tang Y, Yang GY. M2 microglia-derived exosomes protect the mouse brain from ischemia-reperfusion injury via exosomal miR-124. Theranostics. 2019;9(10):2910-23. Epub 20190504. doi: 10.7150/thno.30879. PubMed PMID: 31244932; PMCID: PMC6568171.
58. Ikeda T, Kawabori M, Zheng Y, Yamaguchi S, Gotoh S, Nakahara Y, Yoshie E, Fujimura M. Intranasal Administration of Mesenchymal Stem Cell-Derived Exosome Alleviates Hypoxic-Ischemic Brain Injury. Pharmaceutics. 2024;16(4):446. doi: 10.3390/pharmaceutics16040446.
59. Zhang Y, Chopp M, Zhang ZG, Katakowski M, Xin H, Qu C, Ali M, Mahmood A, Xiong Y. Systemic administration of cell-free exosomes generated by human bone marrow derived mesenchymal stem cells cultured under 2D and 3D conditions improves functional recovery in rats after traumatic brain injury. Neurochem Int. 2017;111:69-81. Epub 20160815. doi: 10.1016/j.neuint.2016.08.003. PubMed PMID: 27539657; PMCID: PMC5311054.
60. Klyachko NL, Arzt CJ, Li SM, Gololobova OA, Batrakova EV. Extracellular Vesicle-Based Therapeutics: Preclinical and Clinical Investigations. Pharmaceutics. 2020;12(12). Epub 20201201. doi: 10.3390/pharmaceutics12121171. PubMed PMID: 33271883; PMCID: PMC7760239.
61. Thippabhotla S, Zhong C, He M. 3D cell culture stimulates the secretion of in vivo like extracellular vesicles. Sci Rep. 2019;9(1):13012. Epub 20190910. doi: 10.1038/s41598-019-49671-3. PubMed PMID: 31506601; PMCID: PMC6736862.
62. Volpe JJ. Commentary - Exosomes: Realization of the great therapeutic potential of stem cells. J Neonatal Perinatal Med. 2020;13(3):287-91. Epub 2020/05/24. doi: 10.3233/NPM-200477. PubMed PMID: 32444568; PMCID: PMC7592649.
63. Witwer KW, Wolfram J. Extracellular vesicles versus synthetic nanoparticles for drug delivery. Nature Reviews Materials. 2021;6(2):103-6. doi: 10.1038/s41578-020-00277-6.
64. Sanz-Ros J, Mas-Bargues C, Romero-Garcia N, Huete-Acevedo J, Dromant M, Borras C. Extracellular Vesicles as Therapeutic Resources in the Clinical Environment. Int J Mol Sci. 2023;24(3). Epub 20230125. doi: 10.3390/ijms24032344. PubMed PMID: 36768664; PMCID: PMC9917082.

65. Thippabhotla S, Zhong C, He M. 3D cell culture stimulates the secretion of in vivo like extracellular vesicles. Scientific Reports. 2019;9(1). doi: 10.1038/s41598-019-49671-3.
66. Kusuma GD, Li A, Zhu D, McDonald H, Inocencio IM, Chambers DC, Sinclair K, Fang H, Greening DW, Frith JE, Lim R. Effect of 2D and 3D Culture Microenvironments on Mesenchymal Stem Cell-Derived Extracellular Vesicles Potencies. Front Cell Dev Biol. 2022;10:819726. Epub 20220214. doi: 10.3389/fcell.2022.819726. PubMed PMID: 35237601; PMCID: PMC8882622.
67. Joseph A, Liao R, Zhang M, Helmbrecht H, Mckenna M, Filteau JR, Nance E. Nanoparticle-microglial interaction in the ischemic brain is modulated by injury duration and treatment. Bioengineering & Translational Medicine. 2020;5(3). doi: 10.1002/btm2.10175.
68. Wood TR, Hildahl K, Helmbrecht H, Corry KA, Moralejo DH, Kolnik SE, Prater KE, Juul SE, Nance E. A ferret brain slice model of oxygen–glucose deprivation captures regional responses to perinatal injury and treatment associated with specific microglial phenotypes. Bioengineering & Translational Medicine. 2021. doi: 10.1002/btm2.10265.
69. Mckenna M, Filteau JR, Butler B, Sluis K, Chungyoun M, Schimek N, Nance E. Organotypic whole hemisphere brain slice models to study the effects of donor age and oxygen-glucose-deprivation on the extracellular properties of cortical and striatal tissue. Journal of Biological Engineering. 2022;16(1). doi: 10.1186/s13036-022-00293-w.
70. Humpel C. ORGANOTYPIC BRAIN SLICE CULTURES: A REVIEW. Neuroscience. 2015;305:86-98. doi: 10.1016/j.neuroscience.2015.07.086.
71. Hill CA, Fitch RH. Sex Differences in Mechanisms and Outcome of Neonatal Hypoxia-Ischemia in Rodent Models: Implications for Sex-Specific Neuroprotection in Clinical Neonatal Practice. Neurology Research International. 2012;2012:1-9. doi: 10.1155/2012/867531.
72. Vella LJ, Scicluna BJ, Cheng L, Bawden EG, Masters CL, Ang S, Willamson N, McLean C, Barnham KJ, Hill AF. A rigorous method to enrich for exosomes from brain tissue:14.
73. van der Walt S, Schonberger JL, Nunez-Iglesias J, Boulogne F, Warner JD, Yager N, Gouillart E, Yu T, scikit-image c. scikit-image: image processing in Python. PeerJ. 2014;2:e453. Epub 20140619. doi: 10.7717/peerj.453. PubMed PMID: 25024921; PMCID: PMC4081273.
74. Schindelin J, Arganda-Carreras I, Frise E, Kaynig V, Longair M, Pietzsch T, Preibisch S, Rueden C, Saalfeld S, Schmid B, Tinevez J-Y, White DJ, Hartenstein V, Eliceiri K, Tomancak P, Cardona A. Fiji: an open-source platform for biological-image analysis. Nature Methods. 2012;9(7):676-82. doi: 10.1038/nmeth.2019.
75. Kongsui R, Beynon SB, Johnson SJ, Walker FR. Quantitative assessment of microglial morphology and density reveals remarkable consistency in the distribution and morphology of cells within the healthy prefrontal cortex of the rat. Journal of Neuroinflammation. 2014;11(1). doi: 10.1186/s12974-014-0182-7.
76. Phillip JM, Han K-S, Chen W-C, Wirtz D, Wu P-H. A robust unsupervised machine-learning method to quantify the morphological heterogeneity of cells and nuclei. Nature Protocols. 2021;16(2):754-74. doi: 10.1038/s41596-020-00432-x.
77. Helmbrecht H. 2022.
78. Huang Y, Cheng L, Turchinovich A, Mahairaki V, Troncoso JC, Pletniková O, Haughey NJ, Vella LJ, Hill AF, Zheng L, Witwer KW. Influence of species and processing parameters on recovery and content of brain tissue-derived extracellular vesicles. Journal of Extracellular Vesicles. 2020;9(1):1785746. doi: 10.1080/20013078.2020.1785746.
79. Tzaridis T, Bachurski D, Liu S, Surmann K, Babatz F, Gesell Salazar M, Völker U, Hallek M, Herrlinger U, Vorberg I, Coch C, Reiners KS, Hartmann G. Extracellular Vesicle Separation Techniques Impact Results from Human Blood Samples: Considerations for Diagnostic Applications. International Journal of Molecular Sciences. 2021;22(17):9211. PubMed PMID: doi:10.3390/ijms22179211.
80. Jeppesen DK, Fenix AM, Franklin JL, Higginbotham JN, Zhang Q, Zimmerman LJ, Liebler DC, Ping J, Liu Q, Evans R, Fissell WH, Patton JG, Rome LH, Burnette DT, Coffey RJ.

Reassessment of Exosome Composition. Cell. 2019;177(2):428-45.e18. doi: 10.1016/j.cell.2019.02.029.
81. Dubbelaar ML, Kracht L, Eggen BJL, Boddeke E. The Kaleidoscope of Microglial Phenotypes. Front Immunol. 2018;9:1753. Epub 2018/08/16. doi: 10.3389/fimmu.2018.01753. PubMed PMID: 30108586; PMCID: PMC6079257.
82. Xu S, Lu J, Shao A, Zhang JH, Zhang J. Glial Cells: Role of the Immune Response in Ischemic Stroke. Frontiers in Immunology. 2020;11. doi: 10.3389/fimmu.2020.00294.
83. Chand S, Jo A, Vellichirammal NN, Gowen A, Guda C, Schaal V, Odegaard K, Lee H, Pendyala G, Yelamanchili SV. Comprehensive Characterization of Nanosized Extracellular Vesicles from Central and Peripheral Organs: Implications for Preclinical and Clinical Applications. ACS Applied Nano Materials. 2020;3(9):8906-19. doi: 10.1021/acsanm.0c01654.
84. Gudbergsson JM, Jønsson K, Simonsen JB, Johnsen KB. Systematic review of targeted extracellular vesicles for drug delivery – Considerations on methodological and biological heterogeneity. Journal of Controlled Release. 2019;306:108-20. doi: 10.1016/j.jconrel.2019.06.006.
85. Yáñez-Mó M, Siljander PR-M, Andreu Z, Bedina Zavec A, Borràs FE, Buzas EI, Buzas K, Casal E, Cappello F, Carvalho J, Colás E, Cordeiro-Da Silva A, Fais S, Falcon-Perez JM, Ghobrial IM, Giebel B, Gimona M, Graner M, Gursel I, Gursel M, Heegaard NHH, Hendrix A, Kierulf P, Kokubun K, Kosanovic M, Kralj-Iglic V, Krämer-Albers E-M, Laitinen S, Lässer C, Lener T, Ligeti E, Linē A, Lipps G, Llorente A, Lötvall J, Manček-Keber M, Marcilla A, Mittelbrunn M, Nazarenko I, Nolte-'T Hoen ENM, Nyman TA, O'Driscoll L, Olivan M, Oliveira C, Pállinger É, Del Portillo HA, Reventós J, Rigau M, Rohde E, Sammar M, Sánchez-Madrid F, Santarém N, Schallmoser K, Stampe Ostenfeld M, Stoorvogel W, Stukelj R, Van Der Grein SG, Helena Vasconcelos M, Wauben MHM, De Wever O. Biological properties of extracellular vesicles and their physiological functions. Journal of Extracellular Vesicles. 2015;4(1):27066. doi: 10.3402/jev.v4.27066.
86. Tkach M, Thery C. Communication by Extracellular Vesicles: Where We Are and Where We Need to Go. Cell. 2016;164(6):1226-32. doi: 10.1016/j.cell.2016.01.043. PubMed PMID: 26967288.
87. Klyachko NL, Arzt CJ, Li SM, Gololobova OA, Batrakova EV. Extracellular Vesicle-Based Therapeutics: Preclinical and Clinical Investigations. Pharmaceutics. 2020;12(12):1171. doi: 10.3390/pharmaceutics12121171.
88. Sun D, Zhuang X, Xiang X, Liu Y, Zhang S, Liu C, Barnes S, Grizzle W, Miller D, Zhang HG. A novel nanoparticle drug delivery system: the anti-inflammatory activity of curcumin is enhanced when encapsulated in exosomes. Mol Ther. 2010;18(9):1606-14. Epub 2010/06/24. doi: 10.1038/mt.2010.105. PubMed PMID: 20571541; PMCID: PMC2956928.
89. Cheng L, Hill AF. Therapeutically harnessing extracellular vesicles. Nat Rev Drug Discov. 2022;21(5):379-99. Epub 20220302. doi: 10.1038/s41573-022-00410-w. PubMed PMID: 35236964.
90. Yi YW, Lee JH, Kim SY, Pack CG, Ha DH, Park SR, Youn J, Cho BS. Advances in Analysis of Biodistribution of Exosomes by Molecular Imaging. Int J Mol Sci. 2020;21(2). Epub 20200119. doi: 10.3390/ijms21020665. PubMed PMID: 31963931; PMCID: PMC7014306.
91. Betzer O, Barnoy E, Sadan T, Elbaz I, Braverman C, Liu Z, Popovtzer R. Advances in imaging strategies for in vivo tracking of exosomes. Wiley Interdiscip Rev Nanomed Nanobiotechnol. 2020;12(2):e1594. Epub 20191215. doi: 10.1002/wnan.1594. PubMed PMID: 31840427.
92. Li YJ, Wu JY, Wang JM, Hu XB, Xiang DX. Emerging strategies for labeling and tracking of extracellular vesicles. J Control Release. 2020;328:141-59. Epub 20200831. doi: 10.1016/j.jconrel.2020.08.056. PubMed PMID: 32882270.
93. Almeida S, Santos L, Falcao A, Gomes C, Abrunhosa A. In Vivo Tracking of Extracellular Vesicles by Nuclear Imaging: Advances in Radiolabeling Strategies. Int J Mol Sci.

2020;21(24). Epub 20201211. doi: 10.3390/ijms21249443. PubMed PMID: 33322484; PMCID: PMC7764519.
94. Choi H, Lee DS. Illuminating the physiology of extracellular vesicles. Stem Cell Research & Therapy. 2016;7(1). doi: 10.1186/s13287-016-0316-1.
95. Shimomura T, Seino R, Umezaki K, Shimoda A, Ezoe T, Ishiyama M, Akiyoshi K. New Lipophilic Fluorescent Dyes for Labeling Extracellular Vesicles: Characterization and Monitoring of Cellular Uptake. Bioconjug Chem. 2021;32(4):680-4. Epub 20210313. doi: 10.1021/acs.bioconjchem.1c00068. PubMed PMID: 33719402.
96. Takov K, Yellon DM, Davidson SM. Confounding factors in vesicle uptake studies using fluorescent lipophilic membrane dyes. J Extracell Vesicles. 2017;6(1):1388731. Epub 20171012. doi: 10.1080/20013078.2017.1388731. PubMed PMID: 29184625; PMCID: PMC5699187.
97. Richter M, Vader P, Fuhrmann G. Approaches to surface engineering of extracellular vesicles. Advanced Drug Delivery Reviews. 2021;173:416-26. doi: 10.1016/j.addr.2021.03.020.
98. Salunkhe S, Dheeraj, Basak M, Chitkara D, Mittal A. Surface functionalization of exosomes for target-specific delivery and in vivo imaging & tracking: Strategies and significance. J Control Release. 2020;326:599-614. Epub 20200728. doi: 10.1016/j.jconrel.2020.07.042. PubMed PMID: 32730952.
99. Zhang M, Bishop BP, Thompson NL, Hildahl K, Dang B, Mironchuk O, Chen N, Aoki R, Holmberg VC, Nance E. Quantum dot cellular uptake and toxicity in the developing brain: implications for use as imaging probes. Nanoscale Advances. 2019;1(9):3424-42. doi: 10.1039/c9na00334g.
100. Kaminski VDL, Ellwanger JH, Chies JAB. Extracellular vesicles in host-pathogen interactions and immune regulation — exosomes as emerging actors in the immunological theater of pregnancy. Heliyon. 2019;5(8):e02355. doi: 10.1016/j.heliyon.2019.e02355.
101. Vojtech L, Woo S, Hughes S, Levy C, Ballweber L, Sauteraud RP, Strobl J, Westerberg K, Gottardo R, Tewari M, Hladik F. Exosomes in human semen carry a distinctive repertoire of small non-coding RNAs with potential regulatory functions. Nucleic Acids Research. 2014;42(11):7290-304. doi: 10.1093/nar/gku347.
102. Vojtech L, Woo S, Hughes S, Levy C, Ballweber L, Sauteraud RP, Strobl J, Westerberg K, Gottardo R, Tewari M, Hladik F. Exosomes in human semen carry a distinctive repertoire of small non-coding RNAs with potential regulatory functions. Nucleic Acids Res. 2014;42(11):7290-304. Epub 20140516. doi: 10.1093/nar/gku347. PubMed PMID: 24838567; PMCID: PMC4066774.
103. Vojtech L, Zhang M, Davé V, Levy C, Hughes SM, Wang R, Calienes F, Prlic M, Nance E, Hladik F. Extracellular vesicles in human semen modulate antigen-presenting cell function and decrease downstream antiviral T cell responses. PLOS ONE. 2019;14(10):e0223901. doi: 10.1371/journal.pone.0223901.
104. Nguyen NP, Helmbrecht H, Ye Z, Adebayo T, Hashi N, Doan M-A, Nance E. Brain Tissue-Derived Extracellular Vesicle Mediated Therapy in the Neonatal Ischemic Brain. International Journal of Molecular Sciences. 2022;23(2):620. doi: 10.3390/ijms23020620.
105. Heidarzadeh M, Sokullu E, Saghati S, Karimipour M, Rahbarghazi R. Insights into the Critical Role of Exosomes in the Brain; from Neuronal Activity to Therapeutic Effects. Molecular Neurobiology. 2022. doi: 10.1007/s12035-022-02853-z.
106. Zhang M, Vojtech L, Ye Z, Hladik F, Nance E. Quantum Dot Labeling and Visualization of Extracellular Vesicles. ACS Applied Nano Materials. 2020;3(7):7211-22. doi: 10.1021/acsanm.0c01553.
107. Schmittgen TD, Lee EJ, Jiang J, Sarkar A, Yang L, Elton TS, Chen C. Real-time PCR quantification of precursor and mature microRNA. Methods. 2008;44(1):31-8. doi: 10.1016/j.ymeth.2007.09.006. PubMed PMID: 18158130; PMCID: PMC2663046.
108. Kramer MF. Stem-Loop RT-qPCR for miRNAs. Current Protocols in Molecular Biology. 2011;95(1):15.0.1-.0.1. doi: 10.1002/0471142727.mb1510s95.

109. Ben-Amar A, Oueslati S, Mliki A. Universal direct PCR amplification system: a time- and cost-effective tool for high-throughput applications. 3 Biotech. 2017;7(4). doi: 10.1007/s13205-017-0890-7.
110. den Haan JM, Arens R, van Zelm MC. The activation of the adaptive immune system: cross-talk between antigen-presenting cells, T cells and B cells. Immunol Lett. 2014;162(2 Pt B):103-12. Epub 20141016. doi: 10.1016/j.imlet.2014.10.011. PubMed PMID: 25455596.
111. Rodriguez-Pinto D. B cells as antigen presenting cells. Cell Immunol. 2005;238(2):67-75. Epub 20060330. doi: 10.1016/j.cellimm.2006.02.005. PubMed PMID: 16574086.
112. Wira CR, Rossoll RM, Kaushic C. Antigen-presenting cells in the female reproductive tract: influence of estradiol on antigen presentation by vaginal cells. Endocrinology. 2000;141(8):2877-85. doi: 10.1210/endo.141.8.7594. PubMed PMID: 10919275.
113. Vojtech L, Zhang M, Davé V, Levy C, Hughes SM, Wang R, Calienes F, Prlic M, Nance E, Hladik F. Extracellular vesicles in human semen modulate antigen-presenting cell function and decrease downstream antiviral T cell responses. PLoS ONE. 2019;14(10). doi: 10.1371/journal.pone.0223901.
114. Derks NM, Muller M, Gaszner B, Tilburg-Ouwens DT, Roubos EW, Kozicz LT. Housekeeping genes revisited: different expressions depending on gender, brain area and stressor. Neuroscience. 2008;156(2):305-9. Epub 20080803. doi: 10.1016/j.neuroscience.2008.07.047. PubMed PMID: 18722514.
115. Al-Bader MD, Al-Sarraf HA. Housekeeping gene expression during fetal brain development in the rat-validation by semi-quantitative RT-PCR. Brain Res Dev Brain Res. 2005;156(1):38-45. doi: 10.1016/j.devbrainres.2005.01.010. PubMed PMID: 15862626.
116. Huang K, Marti AA. Recent trends in molecular beacon design and applications. Anal Bioanal Chem. 2012;402(10):3091-102. Epub 20111208. doi: 10.1007/s00216-011-5570-6. PubMed PMID: 22159461.
117. Lamichhane TN, Sokic S, Schardt JS, Raiker RS, Lin JW, Jay SM. Emerging Roles for Extracellular Vesicles in Tissue Engineering and Regenerative Medicine. Tissue Engineering Part B: Reviews. 2014;21(1):45-54. doi: 10.1089/ten.teb.2014.0300.
118. Wiklander OPB, Brennan MÁ, Lötvall J, Breakefield XO, El Andaloussi S. Advances in therapeutic applications of extracellular vesicles. Science Translational Medicine. 2019;11(492):eaav8521. doi: 10.1126/scitranslmed.aav8521.
119. Salikhova DI, Timofeeva AV, Golovicheva VV, Fatkhudinov TK, Shevtsova YA, Soboleva AG, Fedorov IS, Goryunov KV, Dyakonov AS, Mokrousova VO, Shedenkova MO, Elchaninov AV, Makhnach OV, Kutsev SI, Chekhonin VP, Silachev DN, Goldshtein DV. Extracellular vesicles of human glial cells exert neuroprotective effects via brain miRNA modulation in a rat model of traumatic brain injury. Scientific Reports. 2023;13(1). doi: 10.1038/s41598-023-47627-2.
120. Heidarzadeh M, Sokullu E, Saghati S, Karimipour M, Rahbarghazi R. Insights into the Critical Role of Exosomes in the Brain; from Neuronal Activity to Therapeutic Effects. Molecular Neurobiology. 2022;59(7):4453-65. doi: 10.1007/s12035-022-02853-z.
121. Noren Hooten N, Yáñez-Mó M, Derita R, Russell A, Quesenberry P, Ramratnam B, Robbins PD, Di Vizio D, Wen S, Witwer KW, Languino LR. Hitting the Bullseye: Are extracellular vesicles on target? Journal of Extracellular Vesicles. 2020;10(1). doi: 10.1002/jev2.12032.
122. Wu X, Tang T, Wei Y, Cummins KA, Wood DK, Pang HB. Extracellular Vesicles Mediate the Intercellular Exchange of Nanoparticles. Advanced Science. 2022;9(7):2102441. doi: 10.1002/advs.202102441.
123. Liu Q, Huang J, Xia J, Liang Y, Li G. Tracking tools of extracellular vesicles for biomedical research. Frontiers in Bioengineering and Biotechnology. 2022;10. doi: 10.3389/fbioe.2022.943712.
124. Verweij FJ, Balaj L, Boulanger CM, Carter DRF, Compeer EB, D'Angelo G, El Andaloussi S, Goetz JG, Gross JC, Hyenne V, Kramer-Albers EM, Lai CP, Loyer X, Marki A,

Momma S, Nolte-'t Hoen ENM, Pegtel DM, Peinado H, Raposo G, Rilla K, Tahara H, Thery C, van Royen ME, Vandenbroucke RE, Wehman AM, Witwer K, Wu Z, Wubbolts R, van Niel G. The power of imaging to understand extracellular vesicle biology in vivo. Nat Methods. 2021;18(9):1013-26. Epub 20210826. doi: 10.1038/s41592-021-01206-3. PubMed PMID: 34446922; PMCID: PMC8796660.
125. Smyth T, Petrova K, Payton NM, Persaud I, Redzic JS, Graner MW, Smith-Jones P, Anchordoquy TJ. Surface functionalization of exosomes using click chemistry. Bioconjug Chem. 2014;25(10):1777-84. Epub 20140930. doi: 10.1021/bc500291r. PubMed PMID: 25220352; PMCID: PMC4198107.
126. Nance EA, Woodworth GF, Sailor KA, Shih TY, Xu Q, Swaminathan G, Xiang D, Eberhart C, Hanes J. A dense poly(ethylene glycol) coating improves penetration of large polymeric nanoparticles within brain tissue. Sci Transl Med. 2012;4(149):149ra19. Epub 2012/08/31. doi: 10.1126/scitranslmed.3003594. PubMed PMID: 22932224; PMCID: PMC3718558.
127. Nance-Lab/diff_classifier. Available from: https://github.com/Nance-Lab/diff_classifier.
128. Curtis C, Rokem A, Nance E. diff_classifier: Parallelization of multi-particle tracking video analyses. Journal of Open Source Software. 2019;4(36):989. doi: 10.21105/joss.00989.
129. Sykova E, Nicholson C. Diffusion in brain extracellular space. Physiol Rev. 2008;88(4):1277-340. doi: 10.1152/physrev.00027.2007. PubMed PMID: 18923183; PMCID: PMC2785730.
130. Pinholt HD, Bohr SS, Iversen JF, Boomsma W, Hatzakis NS. Single-particle diffusional fingerprinting: A machine-learning framework for quantitative analysis of heterogeneous diffusion. Proc Natl Acad Sci U S A. 2021;118(31). doi: 10.1073/pnas.2104624118. PubMed PMID: 34321355; PMCID: PMC8346862.
131. Mercadante AA, Tadi P. Neuroanatomy, Gray Matter. StatPearls. Treasure Island (FL)2024.
132. Bamford IJ, Bamford NS. The Striatum's Role in Executing Rational and Irrational Economic Behaviors. Neuroscientist. 2019;25(5):475-90. Epub 20190124. doi: 10.1177/1073858418824256. PubMed PMID: 30678530; PMCID: PMC6656632.
133. Bachiller S, Jimenez-Ferrer I, Paulus A, Yang Y, Swanberg M, Deierborg T, Boza-Serrano A. Microglia in Neurological Diseases: A Road Map to Brain-Disease Dependent-Inflammatory Response. Front Cell Neurosci. 2018;12:488. Epub 20181218. doi: 10.3389/fncel.2018.00488. PubMed PMID: 30618635; PMCID: PMC6305407.
134. Ziemka-Nalecz M, Jaworska J, Zalewska T. Insights Into the Neuroinflammatory Responses After Neonatal Hypoxia-Ischemia. Journal of Neuropathology & Experimental Neurology. 2017;76(8):644-54. doi: 10.1093/jnen/nlx046.
135. Weinstein JR, Koerner IP, Moller T. Microglia in ischemic brain injury. Future Neurol. 2010;5(2):227-46. doi: 10.2217/fnl.10.1. PubMed PMID: 20401171; PMCID: PMC2853969.
136. Benjelloun N, Renolleau S, Represa A, Ben-Ari Y, Charriaut-Marlangue C. Inflammatory responses in the cerebral cortex after ischemia in the P7 neonatal Rat. Stroke. 1999;30(9):1916.
137. Ivacko JA, Sun R, Silverstein FS. Hypoxic-Ischemic Brain Injury Induces an Acute Microglial Reaction in Perinatal Rats1. Pediatric Research. 1996;39(1):39-47. doi: 10.1203/00006450-199601000-00006.
138. Paolicelli RC, Bergamini G, Rajendran L. Cell-to-cell Communication by Extracellular Vesicles: Focus on Microglia. Neuroscience. 2019;405:148-57. Epub 20180413. doi: 10.1016/j.neuroscience.2018.04.003. PubMed PMID: 29660443.
139. Yang Y, Boza-Serrano A, Dunning CJR, Clausen BH, Lambertsen KL, Deierborg T. Inflammation leads to distinct populations of extracellular vesicles from microglia. J Neuroinflammation. 2018;15(1):168. Epub 20180528. doi: 10.1186/s12974-018-1204-7. PubMed PMID: 29807527; PMCID: PMC5972400.

140. Burns J, Ransohoff R, Mingueneau M. Isolation of Microglia and Analysis of Protein Expression by Flow Cytometry: Avoiding the Pitfall of Microglia Background Autofluorescence. BIO-PROTOCOL. 2021;11(14). doi: 10.21769/bioprotoc.4091.
141. Nikodemova M, Watters JJ. Efficient isolation of live microglia with preserved phenotypes from adult mouse brain. Journal of Neuroinflammation. 2012;9(1):147. doi: 10.1186/1742-2094-9-147.
142. Nance EA, Woodworth GF, Sailor KA, Shih T-Y, Xu Q, Swaminathan G, Xiang D, Eberhart C, Hanes J. A Dense Poly(Ethylene Glycol) Coating Improves Penetration of Large Polymeric Nanoparticles Within Brain Tissue. Science Translational Medicine. 2012;4(149):149ra19-ra19. doi: 10.1126/scitranslmed.3003594.
143. Santucci L, Bruschi M, Del Zotto G, Antonini F, Ghiggeri GM, Panfoli I, Candiano G. Biological surface properties in extracellular vesicles and their effect on cargo proteins. Sci Rep. 2019;9(1):13048. Epub 20190910. doi: 10.1038/s41598-019-47598-3. PubMed PMID: 31506490; PMCID: PMC6736982.
144. Debnath K, Heras KL, Rivera A, Lenzini S, Shin JW. Extracellular vesicle-matrix interactions. Nat Rev Mater. 2023;8(6):390-402. Epub 20230317. doi: 10.1038/s41578-023-00551-3. PubMed PMID: 38463907; PMCID: PMC10919209.
145. Rautaniemi K, John T, Richter M, Huck BC, Zini J, Loretz B, Lehr CM, Vuorimaa-Laukkanen E, Lisitsyna E, Laaksonen T. Intracellular Dynamics of Extracellular Vesicles by Segmented Trajectory Analysis. Anal Chem. 2022;94(51):17770-8. Epub 20221213. doi: 10.1021/acs.analchem.2c02928. PubMed PMID: 36512439; PMCID: PMC9798377.
146. Rudsari HK, Zoofaghari M, Damrath M, Veletić M, Bergsland J, Balasingham I. Anomalous Diffusion of Extracellular Vesicles in an Extracellular Matrix for Molecular Communication. IEEE Transactions on Molecular, Biological and Multi-Scale Communications. 2023;9(1):8-12. doi: 10.1109/tmbmc.2023.3240928.
147. Olbrich K, Rawicz W, Needham D, Evans E. Water permeability and mechanical strength of polyunsaturated lipid bilayers. Biophys J. 2000;79(1):321-7. doi: 10.1016/S0006-3495(00)76294-1. PubMed PMID: 10866958; PMCID: PMC1300936.
148. Takechi-Haraya Y, Sakai-Kato K, Abe Y, Kawanishi T, Okuda H, Goda Y. Atomic Force Microscopic Analysis of the Effect of Lipid Composition on Liposome Membrane Rigidity. Langmuir. 2016;32(24):6074-82. Epub 20160609. doi: 10.1021/acs.langmuir.6b00741. PubMed PMID: 27232007.
149. Robbins NM, Swanson RA. Opposing Effects of Glucose on Stroke and Reperfusion Injury. Stroke. 2014;45(6):1881-6. doi: 10.1161/strokeaha.114.004889.
150. Khacho M, Tarabay M, Patten D, Khacho P, Maclaurin JG, Guadagno J, Bergeron R, Cregan SP, Harper M-E, Park DS, Slack RS. Acidosis overrides oxygen deprivation to maintain mitochondrial function and cell survival. Nature Communications. 2014;5(1). doi: 10.1038/ncomms4550.
151. Cheng Y, Zeng Q, Han Q, Xia W. Effect of pH, temperature and freezing-thawing on quantity changes and cellular uptake of exosomes. Protein & Cell. 2019;10(4):295-9. doi: 10.1007/s13238-018-0529-4.
152. Wang J, Chen D, Ho EA. Challenges in the development and establishment of exosome-based drug delivery systems. J Control Release. 2021;329:894-906. Epub 20201012. doi: 10.1016/j.jconrel.2020.10.020. PubMed PMID: 33058934.
153. Gao J, Song Q, Gu X, Jiang G, Huang J, Tang Y, Yu R, Wang A, Huang Y, Zheng G, Chen H, Gao X. Intracerebral fate of organic and inorganic nanoparticles is dependent on microglial extracellular vesicle function. Nat Nanotechnol. 2024;19(3):376-86. Epub 20231229. doi: 10.1038/s41565-023-01551-8. PubMed PMID: 38158436.
154. Adami RR, Grundy ME, Poretti A, Felling RJ, Lemmon M, Graham EM. Distinguishing Arterial Ischemic Stroke From Hypoxic–Ischemic Encephalopathy in the Neonate at Birth. Obstetrics and gynecology. 2016;128(4):704-12. doi: 10.1097/AOG.0000000000001631.

155. Gomez-Nicola D, Perry VH. Microglial Dynamics and Role in the Healthy and Diseased Brain. The Neuroscientist. 2015;21(2):169-84. doi: 10.1177/1073858414530512.
156. Savage JC, Carrier M, Tremblay M-È. Morphology of Microglia Across Contexts of Health and Disease. Microglia: Springer New York; 2019. p. 13-26.
157. Phillip JM, Han KS, Chen WC, Wirtz D, Wu PH. A robust unsupervised machine-learning method to quantify the morphological heterogeneity of cells and nuclei. Nat Protoc. 2021;16(2):754-74. Epub 20210111. doi: 10.1038/s41596-020-00432-x. PubMed PMID: 33424024; PMCID: PMC8167883.
158. Yellepeddi VK, Joseph A, Nance E. Pharmacokinetics of nanotechnology-based formulations in pediatric populations. Advanced Drug Delivery Reviews. 2019;151-152:44-55. doi: 10.1016/j.addr.2019.08.008.
159. Liu YJ, Green KN, Holmes TC, Xu X. Commentary: How Do Microglia Regulate Neural Circuit Connectivity and Activity in the Adult Brain? Neurosci Insights. 2022;17:26331055211071124. Epub 20220124. doi: 10.1177/26331055211071124. PubMed PMID: 35098130; PMCID: PMC8796061.
160. Madan CR, and Teitge, B.D. The benefits of undergraduate research: The student's perspective. The mentor: An academic advising journal 2013;15:1-3.
161. Reisel JR, Walker, C.M., Cancado, L., and Mitriyani, D. Successful Undergraduate Research Experiences in Engineering: Student, Faculty, and Industrial Perspectives.2016.

APPENDICES

Appendix A. Supplemental to Chapter 2

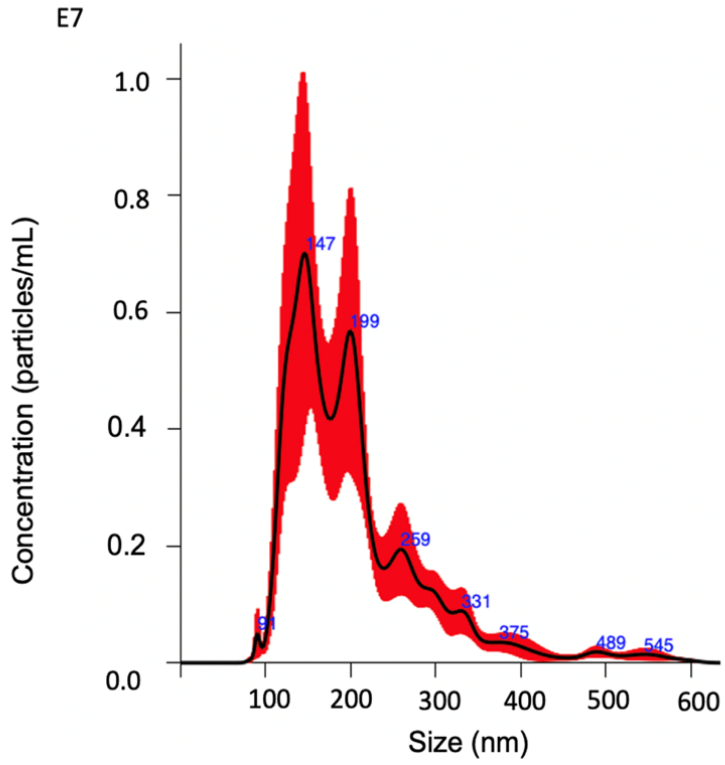

Appendix A. 1. Nanoparticle Tracking Analysis (NTA) quantification of BEVs.
Single representative NTA result of the size distribution of a BEV extract with error bars in red and peaks in blue (N=1 sample). Sample was diluted to 1:1000 in 1X PBS for NTA analysis on the NanoSight.

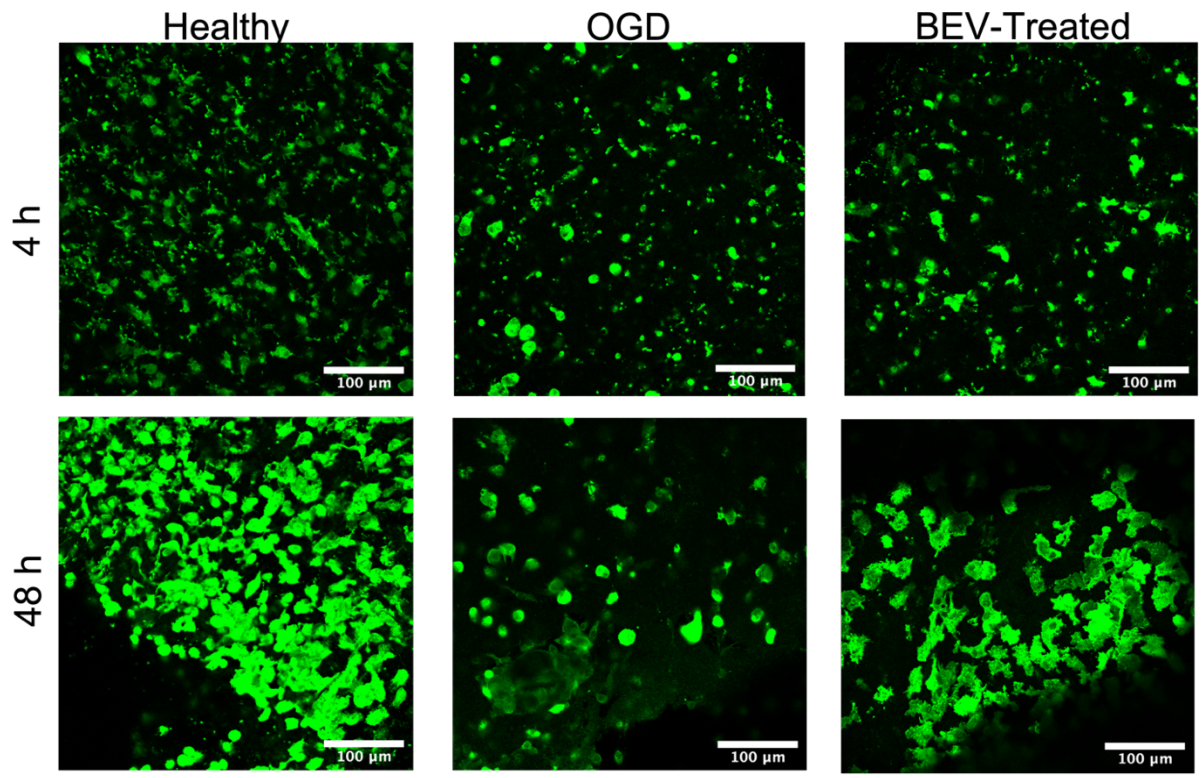

Appendix A. 2. Confocal imaging of microglia in ex vivo brain slices.
Representative confocal imaging examples of Iba-1-stained microglia in ex vivo brain slices at 40x magnification from the cortex of ex vivo brain slices for healthy, OGD control, and 25μg BEV-treated slices at an exposure time of 4 and 48h. Scale bar=100μm

Treatment	Exposure	Shape Mode 1	Shape Mode 2	Shape Mode 3	Shape Mode 4	Shape Mode 5
non-treated control	0 hr	16.3	15	21.5	29.6	17.6
	4 hr	18.5	23.3	15.1	25.3	17.8
	24 hr	14.9	24.3	26	22.1	12.7
	48 hr	15.6	15.6	37.4	19	12.3
ogd control	0 hr	17.7	23.8	20.4	21.4	16.7
	4 hr	17.9	13.5	20.8	31.4	16.4
	24 hr	17.6	19.9	34.1	15.3	13.1
	48 hr	15.2	23.2	28	17.6	16
bev treatment	4 hr	12.3	20.3	29.5	21.2	16.7
	24 hr	12.2	21.8	36.5	17.3	12.2
	48 hr	22.5	17	21.7	21.7	17

Key: Percent Shape Mode	12	17	21	27	38

Appendix A. 3. Global heatmaps of percent shape mode by treatment and then followed by exposure time.

Appendix B. Supplemental to Chapter 3.

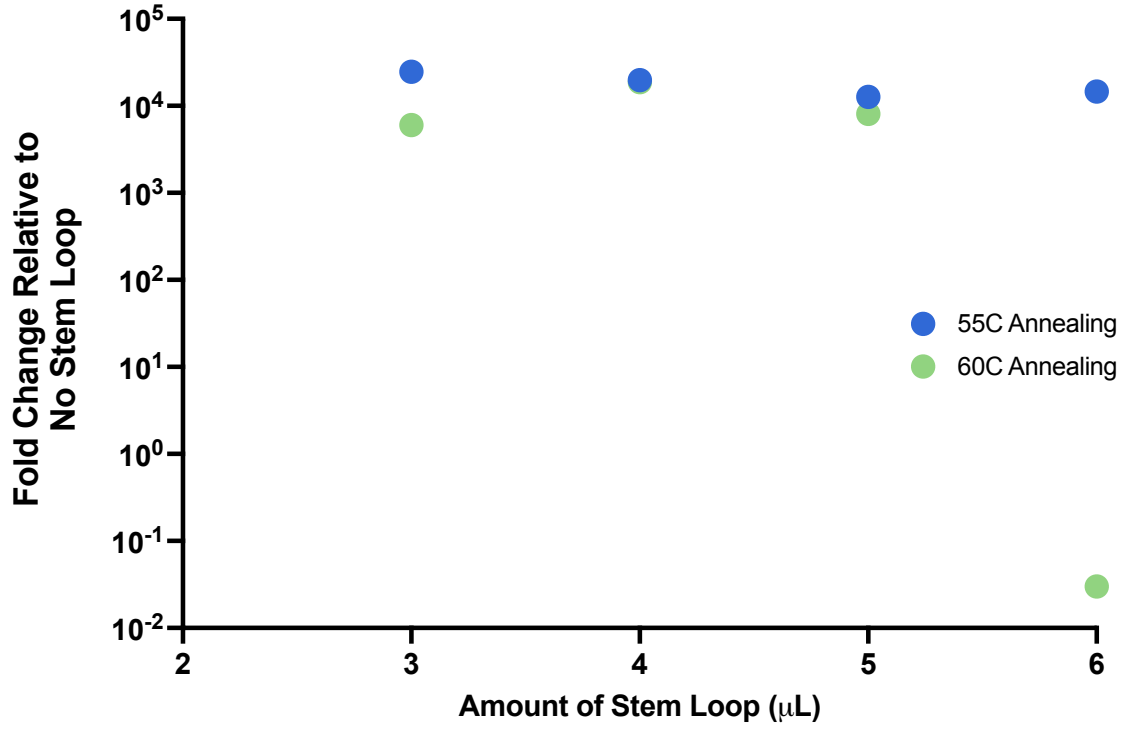

Appendix B. 1. Stemloop dilution quantification.
Expression levels of oligobarcode using various dilutions of stem-loop primer compared to a non stem-loop control. Annealing temperatures used are 55℃ and 60℃.

Appendix C. Supplemental to Chapter 4

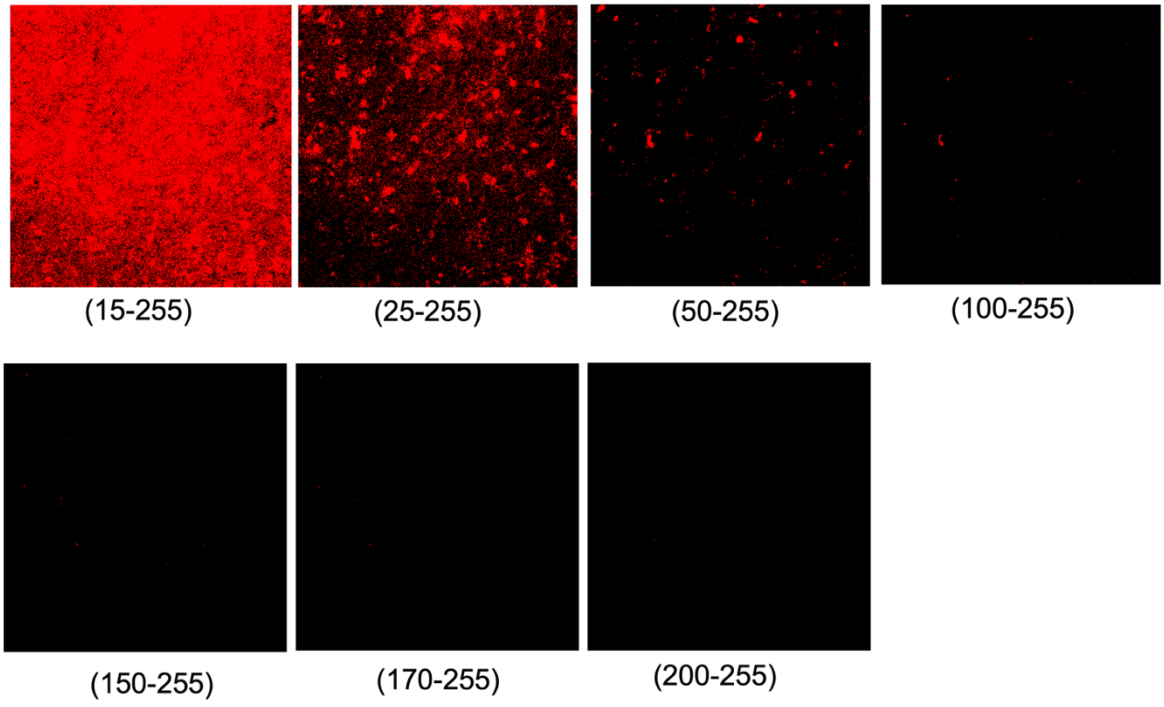

Appendix C. 1. Color intensity thresholding values to remove brain tissue autofluorescence. Thresholding parameters set on non-treated, healthy ex vivo brain slices to remove tissue autofluorescence (red). Images were taken on a confocal microscope at 40x in the cortical region and thresholded in ImageJ.

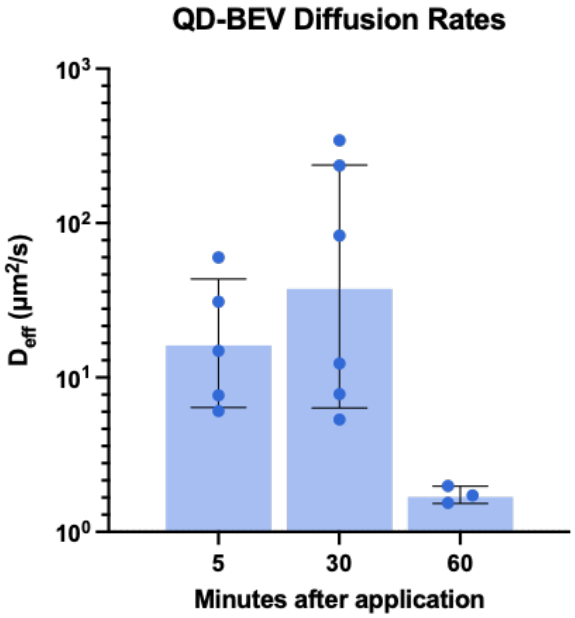

Appendix C. 2. Diffusion coefficients of QD-BEVs in brain tissue over time.
Diffusion coefficient ($\mu m^2/s$) of QD-BEVs topically applied to healthy ex vivo brain slices and exposed for various lengths of time prior to MPT (5, 30, 60 min). Error bars reported represent mean with standard deviation.

A.

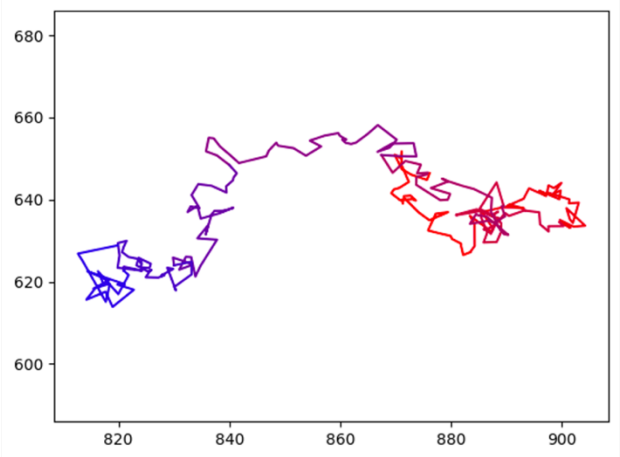

B.

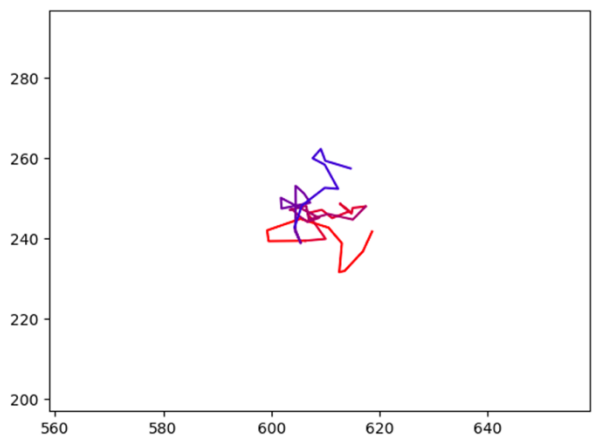

Appendix C. 3. Depiction of QD-BEV trajectories in ex vivo brain tissue.
Computationally generated X-Y plots of QD-BEV trajectories with a A) high mean squared displacement and B) low mean squared displacement derived from the Trackmate plug-in in ImageJ. The color gradient represents increasing time-steps, with blue the earliest time-step and red the latest time-step collected.

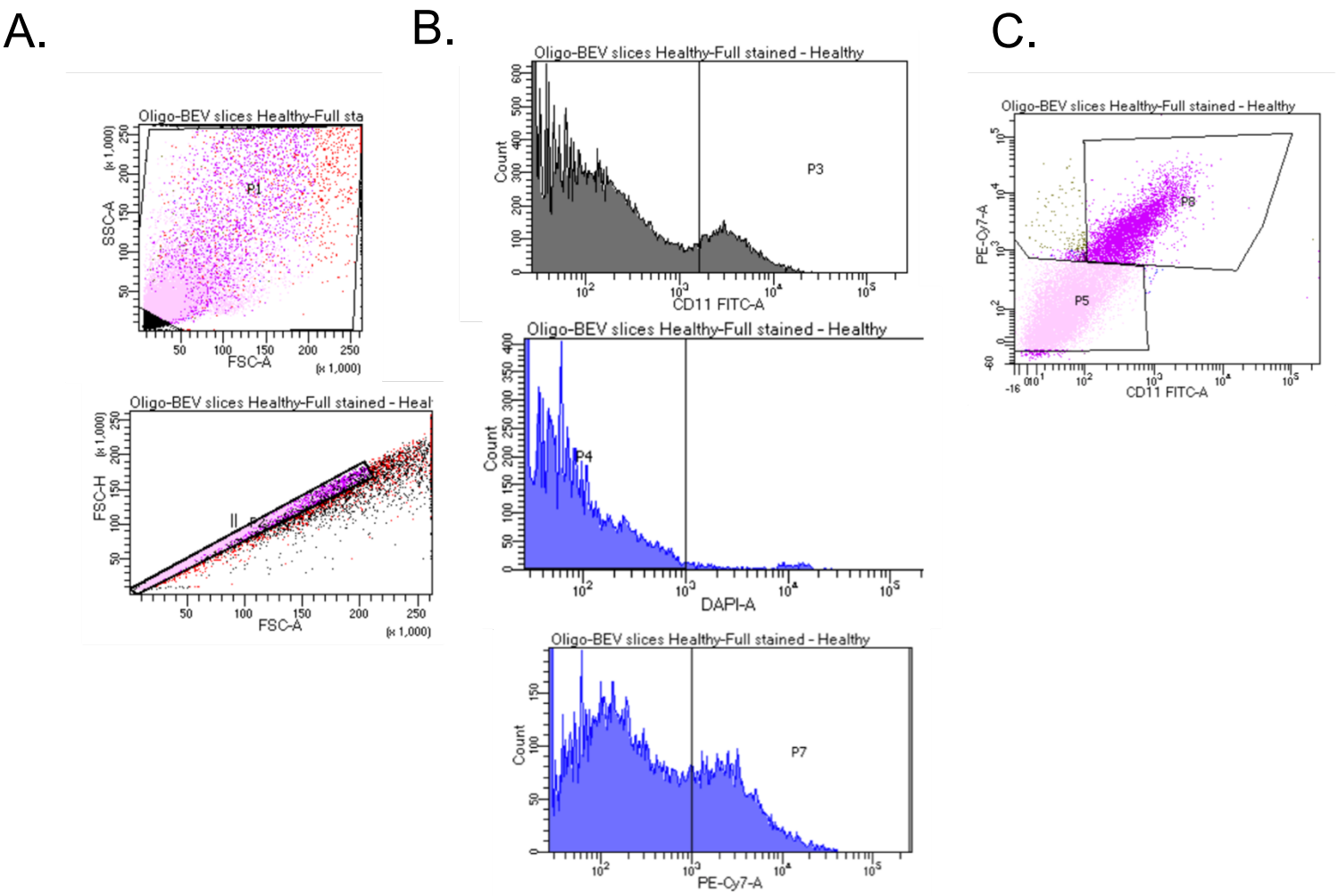

Appendix C. 4. FACS gating strategy for isolating microglia from ex vivo brain tissue. A) Cells are identified from cell debris (top) and singlet cells are identified and gated (bottom) prior to B) gating by markers of interest: CD11b (top), DAPI (center), and CD45 (bottom). C) CD11b+/CD45+ cells were identified as microglia, and were gated and collected (P9 gate), while the rest of the cells were identified as non-microglia and were also gated (P5 gate) and collected.